Frequency Estimation under Stationary and Non-stationary Conditions - A Case Study of Induction Motor Fault Diagnosis

Anik Kumar Samanta

Frequency Estimation under Stationary and Non-stationary Conditions - A Case Study of Induction Motor Fault Diagnosis

Thesis submitted to
Indian Institute of Technology, Kharagpur
for the award of the degree
of

Doctor of Philosophy

by

Anik Kumar Samanta

under the supervision of

Aurobinda Routray
Professor, Dept. of Electrical Engineering

and

Swanand R. Khare
Assistant Professor, Dept. of Mathematics

ADVANCED TECHNOLOGY DEVELOPMENT CENTRE
INDIAN INSTITUTE OF TECHNOLOGY, KHARAGPUR
October 2021

APPROVAL OF THE VIVA-VOCE BOARD

Date: October 11, 2021

Certified that the thesis entitled **Frequency Estimation under Stationary and Non-stationary Conditions - A Case Study of Induction Motor Fault Diagnosis** submitted by **Anik Kumar Samanta** to Indian Institute of Technology Kharagpur, for the award of the degree of Doctor of Philosophy has been accepted by the external examiners and that the student has successfully defended the thesis in the viva-voce examination held today.

Prof. Pabitra Mitra
(Member of the DSC)

Prof. V. N. A. Naikan
(Member of the DSC)

Prof. Nirmalya Ghosh
(Member of the DSC)

Prof. Aurobinda Routray
(Supervisor)

Prof. Swanand R. Khare
(Joint Supervisor)

(Prof. Anil Kulkarni)
(External Examiner)

(Prof. Pranab K. Dutta)
(Chairman of the DSC)

Advanced Technology Development Centre
Indian Institute of Technology, Kharagpur
Kharagpur, India 721302.

Certificate

This is to certify that this thesis entitled **Frequency Estimation under Stationary and Non-stationary Conditions - A Case Study of Induction Motor Fault Diagnosis** submitted by **Anik Kumar Samanta**, to the Indian Institute of Technology Kharagpur, is a record of bonafide research work carried out under our supervision and is worthy of consideration for award of the degree of Doctor of Philosophy of the Institute.

Aurobinda Routray
Department of Electrical Engineering
Indian Institute of Technology Kharagpur
India 721302.

Swanand R. Khare
Department of Mathematics
Indian Institute of Technology Kharagpur
India 721302.

Indian Institute of Technology Kharagpur, Kharagpur
Date:

Declaration

I certify that

a. the work contained in the thesis is original and has been done by me under the guidance of my supervisors;

b. the work has not been submitted to any other institute for any other degree or diploma;

c. I have followed the guidelines provided by the Institute in preparing the thesis;

d. I have conformed to ethical norms and guidelines while writing the thesis;

e. whenever I have used materials (data, models, figures and text) from other sources, I have given due credit to them by citing them in the text of the thesis, and giving their details in the references, and taken permission from the copyright owners of the sources, whenever necessary.

Anik Kumar Samanta

Dedicated to

Maa and Baba

Acknowledgment

This thesis marks the end of a long and eventful journey that wouldn't have been possible without the encouragement and support of several people. I am indebted to my supervisors, Prof. Aurobinda Routray and Prof. Swanand Khare for their guidance, teaching, and feedback throughout the research work. I am grateful to the Doctoral Scrutiny Committee, Prof. P.K. Dutta, Prof. Pabitra Mitra, Prof. V. N. A. Naikan, and Prof. Nirmalya Ghosh for their valuable suggestions during the tenure of the work. I am thankful to the Head, Advanced Technology Development Centre; Head, Centre for Railway Research; and Head, Dept. of Electrical Engineering, IIT Kharagpur, for facilitating the research work. My sincere gratitude towards the examiners Prof. Jose Antonino Daviu (Universitat Politècnica de Valencia) and Prof. Anil Kulkarni (IIT Bombay) for examining the thesis and providing their valuable and encouraging comments.

It was a great opportunity for me to work with my co-researchers, Dr. Arunava Naha, Dr. Ayan Mukherjee, Dr. Somnath Sengupta, and Dr. Chittaranjan Pradhan. I am grateful to them for their continuous inspiration and valuable suggestions. I would like to thank the interns Ayush Bansal, Amey Pawar, Poonam Priyadarshini Parida, Souradeep Ghosh, Varun Nagesh Jolly Behera, Subhayan de, and Praveen Chaubey who were instrumental in multiple exploratory works with me.

I am grateful to Prof. Vivek Goyal (Boston University) and Prof. Anna Scaglione (Arizona State) for their insightful interaction and discussions. I am thankful to the IEEE SPS student branch especially Prof. P.K. Dutta and Prof. Anirban Mukherjee for mentoring and the SPS members Lily, Akanksha, and

Suman for their dedication, hard work, and collaborations in the IEEE SPS student branch.

I would like to appreciate the help and support of all my colleagues in the Embedded Controls lab, CRR Lab, and RTES Lab. My special thanks to Soumi, Anushree, Aritra, Anwesha Di, Arvind, Himadri, Ramnarayan, Yasar, and Rahul who inspired me in research and made my stay on the campus enjoyable and memorable. I am indebted to my school friends Abhijeet, Abhinandan, Arindam, Ases, Anirban, Tamojit, and Preetam for their love, support, and appreciation.

My deepest gratitude goes to my parents, Sasa, Lisha, and other members of my family for their unflagging love and support throughout my life. This thesis would not have been possible without their sacrifices, love, and support.

Abstract

Signal parameters carry vital characteristic information about any physical process. Fourier bases have been of tremendous analytical potential that still spans the space of signature analysis. This thesis attempts to retrieve phase information of signals with time-varying and constant frequencies to gain insight into such processes.

We adopt a model-based approach to estimate the instantaneous frequency (IF) of multiple time-varying components using a linearized constrained Kalman-based method. The method is used for estimating the chirp-like characteristic features of gravitational waves emanated from the merging of binary black-holes. The phase abstraction property of the method is used for extracting the dominant modes of the signal. The removal of dominant modes reduces the spectral leakage for stationary frequency estimation. As a consequence, previously obscured low-magnitude frequency components are observable.

We propose two spectral estimators in the thesis for stationary conditions when the frequency is constant in the observation window. The Rayleigh-quotient-based method uses the well-known Fourier basis constructed Eigenvectors to estimate the unknown Eigenvalues of a symmetric autocorrelation matrix. The technique has high frequency and amplitude accuracy and requires low computational resources. The approach is data-driven and doesn't require any information about the underlying model. Alternatively, the proposed Bayesian spectral estimator is model-based and can incorporate knowledge of the underlying model. It is sequential and has higher accuracy than the Rayleigh-quotient spectrum. The use of an accurate model can further improve the precision of the approach.

One significant impact of this thesis is the detection and estimation of low-amplitude sinusoidal components buried under noise and masked by the presence of high-magnitude elements. A similar and practical situation arises while detecting weak induction motor faults. Hence, the case study of detecting weak SCIM faults is used to validate the proposed algorithms. Furthermore, a minimum distance-based hypothesis test is recommended for incorporating the inherent fault information. Two embedded platforms are also presented in this thesis for hardware realization of the suggested algorithms. The SIMULINK Real-Time (SLRT)-based hardware is appropriate for detecting faults in a single motor. However, the hardware is costly, but its flexibility for initial feasibility studies is advantageous. On the other hand, the Internet-of-things-based system has been tailor-made for dedicated fault detection in a multiple-motor scenario.

Keywords: Bayes theorem, closely spaced sinusoids, constrained Kalman filter, current analysis, fault diagnosis, Gauss-Markov process, gravitational waves, hypothesis testing, incipient faults, induction motor, instantaneous frequency estimation, Internet of things, non-stationary signal, Rayleigh-quotient, signal-conditioning, Simulink Real-Time, spectral estimation, time-varying autoregressive process, vibration analysis.

Contents

List of Figures

List of Tables

List of Abbreviations

AC	Alternating current
AR	Autoregressive
ARM	Advaned RISC machine
ARMA	Autoregressive moving average
BRB	Broken rotor bars
CDF	Cumulative distribution function
CRLB	Cramer-Rao lower bound
CWRU	Case Western Reserve University
DC	Direct current
DFT	Discrete Fourier transform
DL	Deep learning
DOS	Disk operating system
EKF	Extended Kalman filter
EMD	Empirical mode decomposition
ESPRIT	Estimation of signal parameters via rotational invariance technique
FA	False alarm
FFT	Fast Fourier transform
GHz	Unit of frequency in giga-Hertz
GLRT	Generalized likelihood ratio test
HTTP	Hypertext transfer protocol
Hz	Unit of frequency in Hertz
IF	Instantaneous frequency
IoT	Internet of things
JSON	Javascript object notation
kW	Unit of power in kilo-Watt
LIGO	Laser interferometer gravitational-wave observatory
MAP	Maximum a posteriori

MC	Monte-carlo
MCS	Monte-carlo simulation
MD	Missed detection
ML	Machine learning
MLE	Maximum likelihood estimation
mm	Unit of length in millimeter
MSE	Mean squared error
MUSIC	Multiple signal classification
NMSE	Normalized mean squared error
PDF	Probability density function
PLL	Phase locked loop
RAM	Random access memory
RANSAC	Random sample consensus
RM	Reassignment method
RQS	Rayleigh quotient spectrum
RT	Real-time
s	Unit of time in seconds
SCIM	Squirrel cage inductions motors
SLRT	SIMULINK Real-Time
SNR	Signal to noise ratio
SPIFFS	Serial peripheral interface flash file system
SST	Synchrosqueezed technique
STFT	Short-time Fourier transform
SVM	Support vector machine
TF	Time-frequency
TVAR	Time-varying autoregressive
UDP	User datagram protocol
VFD	Variable frequency drive
WSS	Wide-sense stationary
WSST	Wavelet synchrosqueezed transform

List of Symbols

Set:

$\mathbb{N}$	Set of natural numbers $\{1, 2, \ldots,\}$
$\mathbb{Z}$	Set of integers $\{0, \pm 1, \pm 2, \ldots,\}$
$\mathbb{Z}^+$	Set of positive integers $\{0, 1, 2, \ldots,\}$
$\mathbb{R}$	Set of real numbers
$\mathbb{C}$	Set of complex numbers

Math operators:

$\exp(\cdot)$, $e^{(\cdot)}$	Exponent operator
$\ln(\cdot)$	Natural logarithm
$\|\cdot\|_2$	2-norm, Euclidean norm.
j	$= \sqrt{-1}$

Probability:

$\mathcal{N}(\mu, \sigma_v^2)$	Gaussian distribution with mean μ and variance σ_v^2
$\mathcal{U}(a, b)$	Uniform distribution within the range a and b.
γ	Decision statistic for probability of resolution, threshold for hypothesis testing
$\mathcal{P}(A)$	The probability of event A
$\mathcal{H}_0$	Null hypothesis
$\mathcal{H}_1$	Alternate hypothesis
$p\left(\cdot\right)$	Probability density function
$\mathcal{T}_i$	Test statistic under i^{th} hypothesis
$\mathcal{P}_e$	Total probability of error
τ	Tolerance
$\mathcal{P}(A\|B)$	Probability of event A given B
$\mathcal{E}$	Expectation operator

Matrix notation:

$(\cdot)^T$	Transpose operation.
$(\cdot)^H$	Hermitian transpose operation
$\boldsymbol{R}$	Observation noise covariance
$\boldsymbol{Q}$	State noise covariance
$\boldsymbol{I}$	Identity matrix
$\mathbb{C}^{p\times p}$	Complex $p \times p$ matrix
$\mathbb{C}^{p}$	Complex p-dimensional vector
$\boldsymbol{K}$	Kalman gain
$\boldsymbol{R}_x$	Autocorrelation matrix
$\boldsymbol{X}$	Data matrix
λ	Eigenvalue
$\boldsymbol{v}$	Eigenvector

Signal parameters:

$\lvert A_i \rvert$	Amplitude
$\omega_i[n]$	Normalized instantaneous frequency of i^{th} component
ω_i	Normalized frequency of i^{th} component
ϕ_i	Phase of i^{th} component
$f_i[n]$	Instantaneous frequency of i^{th} component
f_i	Frequency of i^{th} component
F_s	Sampling rate (samples/s)
$v(n)$	Additive white Gaussian noise with zero mean and variance σ_v^2
p, q	model order
$\tilde{q}$	Number of high-amplitude dominating frequency components
$X_i(z)$	Z-transform of $x_i(n)$
$P_x(\omega, n)$	Spectrogram
L	Autocorrelation matrix size
N	Length of the time-sequence data

Fault analysis:

f_{bv}, f_{bi}	Characteristic vibration and current frequency components for the broken rotor bar

f_{sv}, f_{si}	Characteristic vibration and current components for inter-turn short circuit
f_{ev}, f_{ei}	Characteristic vibration and current components for eccentricity fault
f_{mv}, f_{mi}	Characteristic vibration and current components for mixed eccentricity fault
f_{ov}, f_{oi},	Characteristic vibration and current components for outer-raceway fault
f_{irv}, f_{iri},	Characteristic vibration and current components for inner-raceway fault
f_{rv}, f_{ri},	Characteristic vibration and current components for rolling-element fault
f_{cv}. f_{ci}	Characteristic vibration and current components for cage defect
s	Slip
N_b	Number of rolling elements
b_d	Ball diameter
d_ρ	Ball pitch diameter
β	Contact angle between the ball and the races, chirp-rate
f_o	Fundamental supply frequency
N_r	Number of rotor bars/ rotor slots
f_s	Synchronous frequency
N_s	Synchronous speed

CHAPTER 1

Introduction

A stochastic process is said to be strictly stationary if its statistical properties do not change with time. Majority of signal processing applications, including spectral estimation, detection, general estimation theory, and system modeling assumes the underlying model to be wide sense stationary. However, it is prudent to invoke a test to determine the stationarity of the data. In classical literature, most of the stationarity tests involved finding the whiteness and Gaussanity of the signal. Although, hypothesis testing for detecting stationarity [2–4] and stationary segment of data [5] is recommended. According to Chau [6], "Majority of non-stationarities occur due to temporally unstable variance or variable frequency"

Frequency estimators are classified as stationary and non-stationary depending on the statistical properties of the input signal. Stationary frequency estimators can be classified [7] into (a) classical methods like discrete Fourier transforms, power spectral densities; (b) high-resolution subspace-based spectral estimators like multiple signal classifier (MUSIC) [8], estimation of signal parameters via rotational invariance technique (ESPRIT) [9]; and (c) model-based approaches like autoregressive (AR), autoregressive moving average (ARMA), and moving average spectral estimators [7]. The majority of signals encountered in various applications are non-stationary [10] due to presence of time-varying frequency component. The estimation of instantaneous frequency (IF) have been used to estimate time-varying frequency components. Applications of IF estimation include speech processing [11], power quality estimation [12], disease detection [13], machine fault diagnosis [14], etc.

In this thesis we tackle the problem of estimating frequency under stationary and non-stationary conditions and use the estimates to detect weak faults in electromechanical systems. The primary challenge of fault diagnosis is the detection and estimation of minute fault-specific signatures which are obscured by noise and are vaguely discernible in the presence of multiple other dominant components. The detection of weak faults enable us to elevate the laboratory case study into a practical implementation where incipient faults can be detected with high certainty well before a failure takes place. The detection of early-stage defects can reduce plant downtime, avoid recurring servicing costs, and can help in predictive maintenance. Squirrel cage induction motors (SCIM) are the workhorse of any industry and have been very popular due to their robustness and low-maintenance. We have tested the efficiency of the developed frequency estimators by using a case study of SCIM weak fault detection. For the purpose, we have used a 22-kW SCIM motor setup. Additionally, we have also used the publicly available Case Western Reserve University (CWRU) bearing fault data [15] for comparison and validation.

1.1 Literature Survey

The literature survey starts with a description of different spectral estimators followed by a survey of available IF estimation techniques. The frequency estimation survey is followed by the case-study of SCIM fault diagnosis. Considering the different problems associated with the detection of SCIM faults, we have divided the review of existing literature into different sections. We start with a description of various faults that affect the SCIM. This followed by an account of different input signals that are used for the fault detection. The next section reviews the existing methods of fault detection and classification algorithms.

1.1.1 Review of Existing Spectral Estimators

Spectral estimation of a wide-sense stationary (WSS) signal buried in white noise has seen significant development for the last 50 years. The use of spectral estimates has been phenomenal in detecting SCIM faults [16]. Lower computational complexity and the emergence of digital signal processors made Fourier transform indispensable for many ground-breaking applications. However, the low mean-squared error (MSE) requirement and improved resolution have driven the next level of research.

The orthogonality of eigenvectors of the Hermitian autocorrelation matrix has been of significant consequence. With the initial formulation by Pisarenko and later modifications by Schmidt has led to the MUSIC algorithm [8]. MUSIC still has been able to encourage the research community for further development in iMUSIC [17], Gold-MUSIC [18], etc. When the frequency components are closely-spaced, the interference due to the dominant components degrades the estimation of weak components. [19] reduced the effect of interference mathematically by relegating the interfering eigenvectors to an arbitrary matrix before computing the MUSIC null-spectra.

The subspace-based spectral estimators have inherently higher resolution, but they also require an accurate estimate of the model-order [20]. On the other hand, parametric model-based spectral estimators use the underlying model information to improve the resolution and decrease the MSE. Resolution of the model-based methods is dependent on the model-order instead of the data length (N). Although advantageous under data length restrictions, an arbitrary high-order selection can result in spurious peaks and spectral splitting.

The model-based methods require an inversion of the autocorrelation matrix. Maximum likelihood estimation (MLE) of the spectrum is asymptotically efficient. However, MLE is computationally complex and requires solving a non-convex multi-modal cost function [19]. Faster implementation of the inversion can be achieved by using the structure of the Toeplitz matrix. Spectral estimation with structured Toeplitz constraints can be found in [21]. The absence of regularization in AR-spectrum estimation leads to the inversion of an ill-conditioned matrix. The methods discussed till now have not considered any additional information about the estimated parameters. In [22], the authors have used a Gaussian prior for spectral estimation. The maximum-a-posterior (MAP) estimation solves a regularized least square problem. The regularized least square involves the inversion of a well-conditioned matrix.

Djuric and Li [23] provided the systematic use of prior distribution of signal and noise parameters for posterior-frequency estimation. [24] used Tikhonov prior for both the phase and frequency parameter for MAP estimation. The use of a sparse Bayesian model with l_1-norm minimization can be found in [25]. A Bernoulli-Gaussian prior was used in [26]. The discrete Bernoulli's distribution ascertained the model order, or the number of components present in the signal, whereas the Gaussian prior localized the frequency. The mixture model was then solved using the variational Bayes framework.

Use of Bayesian inference for estimating spectrogram of a quasi-stationary signal was demonstrated in [27]. The literature discussed until now have used a prior on the parameters of the harmonic model. However, the requirement of sequential detection of non-stationarity has been instrumental in defining the model parameters as a first-order Gauss-Markov process [5]. In [5], the authors have considered a linear system's output for a given input to estimate the time-varying parameters. In this thesis, we have modeled the input signal as a time-varying AR (TVAR) process. The parameters of the model are considered to be random, defined by a first-order Gauss-Markov process.

Till now, we have considered the constant frequency under stationary conditions. However, most natural phenomenons are characterized by the presence of time-dependent frequency components. The next section examines the development of IF estimation algorithms.

1.1.2 Survey of Instantaneous Frequency Estimators

IF estimators have mainly revolved around linear transformations like short-time Fourier transform (STFT), wavelet transforms, along with their quadratic counterparts - the spectrogram, and scalogram, respectively [28]. Wigner-Ville-type distributions have overcome the difficulties of bias and low-resolution of classical estimators. However, existence of cross-term while estimating IF of multiple components affected the method invariably [29]. Also, the length of the data window determines the resolving power of the classical estimators.

The S-transform used a Gaussian window-based STFT. The variance of the Gaussian function decides the window length and hence, the resolution of the S-transform. An angle parameter was added to the Gaussian function to tune the window for variable chirp-rates in fractional Fourier transform [30]. A single global parameter cannot select the optimum window of the transformation for multiple components with different chirp-rates. Hence, local optimization were performed to find the optimal window at each point in the time-frequency (TF) plane [31].

A new approach towards TF-analysis emerged with the inclusion of the phase information [28]. The phase information concentrated the TF-energy and resulted in the development of the reassignment method (RM) [32] and the synchrosqueezed technique (SST) [33]. The advantage of SST in extracting the modes of a non-stationary signal like empirical mode decomposition (EMD) makes it advantageous over RM [34]. For multicomponent signals with non-harmonic modes, Pham and Meignen extended the second-order SST [35] to higher orders in [36] for narrow band energy distribution and increased accuracy. The authors in [36] have used the example of gravitational waves as a practical application. An iterative demodulation-based post-processing technique for improving the resolution of SST and RM under low signal to noise ratio (SNR) was proposed in [37].

The demodulation enhances the energy localization in the TF plane. For multiple components, the TF plane is partitioned to accommodate each component separately. The demodulation is repeated until a desired MSE is achieved. A similar approach can also be found in [38], where multiple components are extracted individually by parametric demodulation using the estimate of the IF followed by bandpass filtering. This demodulation results in a stationary component having the initial frequency as its sole constituent. Therefore, the problem with frequency components that are closely-spaced or having intersecting trajectories needs to be addressed. In [39], a fast non-linear least square method was presented for finding the initial frequency and the chirp-rate for a linear-chirp model with real sinusoids. However, its performance in estimating quadratic frequency components needs validation.

The least-squares estimates are perturbed in the presence of outliers. A similar phenomenon is observed when IF is estimated from TF distribution. Random sample consensus (RANSAC) reduced the impact of the outliers for single component estimated using Wigner distribution [40]. However, the MSE was -20 dB for 5 dB SNR. The proposed algorithm has a normalized-MSE (NMSE) of -30 dB under 5 dB SNR . Improvement with RANSAC for multiple overlapping components was shown in [41].

Majority of the methods surveyed are offline, and the IF estimation require individual component decomposition. Sequential estimation with minimum-MSE of the TVAR parameters using Kalman filters and subsequent spectral estimation was shown in [42, 43]. The state propagation and measurement models are linear [42, 43]. However, direct IF estimation from the TVAR process leads to a non-linear observation model. As a result, the extended Kalman filter (EKF) [44] for single component and harmonic components [12] are used.

Ahn et al. [45] have used different strategies for state estimation of a Markovian jump system. Model selection using probabilistic neural networks and Kalman filter for optimal state estimation is reported in [46]. However, for IF estimation, the model is non-linear and may change at each instant of time. As a result, the number of test hypotheses grows exponentially with time, and the estimation becomes intractable [45]. An adaptive notch filter formulation was employed using a recursive prediction error algorithm in [47]. Based on [47], a self-optimizing method was used in [48] for multiple components, with further research in [49]. The use of a phase-locked loop (PLL) for non-sinusoidal frequency estimation [50] is encouraging. However, PLL is limited due to incapability to estimate multiple components. Based on the brief survey of literature, we can summarize that

i. The conventional multi-component IF estimators require the signal to be decomposed into individual subcomponents before determining the ridges in the TF energy distribution [31].

ii. Decomposition of cross-over components and closely-spaced frequencies is yet unsolved.

iii. The IF estimation performance is limited by the Gabor-Heisenberg uncertainty principle in terms time and frequency resolutions where one can only be gained at the expense of the other [51]. The uncertainty severely deteriorates the performance of conventional methods under higher chirp-rates and components exhibiting abrupt changes in frequency.

iv. The resolution of Fourier-based methods is dependent on the window length, and that of the model-based techniques are dependent on the number of parameters or the lags. Over-estimation of the model-order improves the resolution, but it can result in spurious ridges in the TF-plane. On the other hand, the sequential estimators mainly dealt with the estimation of a single component.

1.1.3 Squirrel Cage Induction Motor Faults

Various surveys have estimated that mechanical faults of damaged bearings constitute most of the SCIM faults [52], followed closely by stator faults and broken rotor bars (BRB) [53]. Improvements in the manufacturing and fabrication processes have reduced rotor faults. However, existing challenges of detecting rotor faults fosters relevant research [53]. In recent times, the study of stator fault takes precedence over the rotor and bearing defects, as emphasized by Fig. 1.1. A brief overview of different faults [54] that plague induction motors are described in the following subsection.

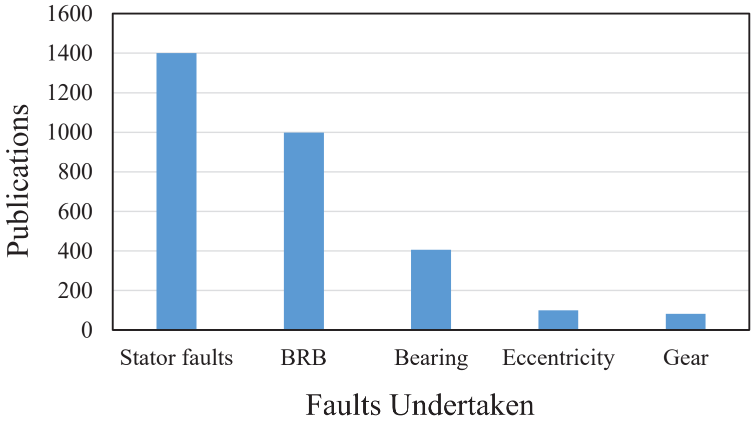

Figure 1.1: Faults undertaken in published works from 2011 to June 2020. Data source: Scopus [1].

1.1.3.1 Bearing Faults

As depicted in Fig. 1.2, bearing faults can be classified into three major categories depending upon the damage to a particular component. These faults are outer-raceway fault, inner-raceway fault, and rolling element fault. Apart from these, faults can also plague the cage that holds the rolling elements.

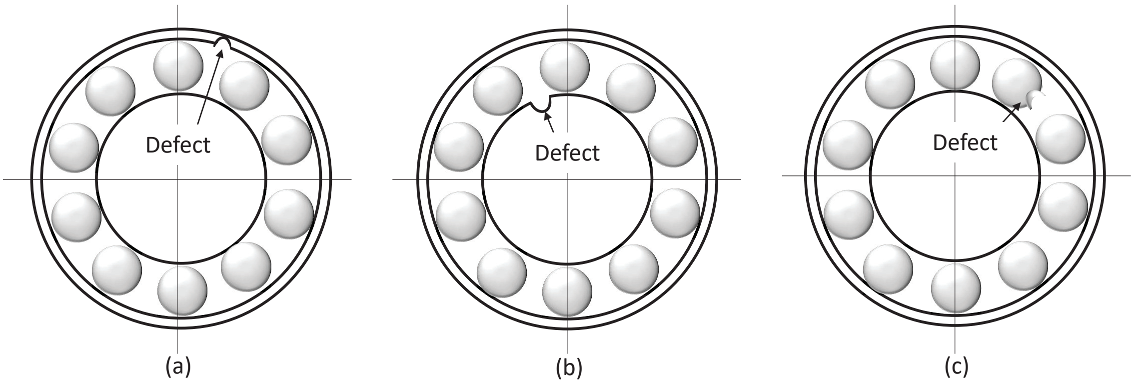

Figure 1.2: Different types of bearing defects. From left to right: Inner-raceway fault, outer-raceway fault, and rolling-element fault.

i. *Outer-raceway fault:* Point faults in the outer raceway exhibit characteristic frequency components in the vibration spectrum, according to (1.1)

$$f_{ov} = \left(\frac{N_b}{2}\right) f_r \left[1 - \frac{b_d}{d_\rho} \cos\beta\right]. \tag{1.1}$$

ii. *Inner-raceway fault:* Similarly, damage to the inner raceway gives fault-specific frequency components in the vibration spectrum as

$$f_{irv} = \left(\frac{N_b}{2}\right) f_r \left[1 + \frac{b_d}{d_\rho} \cos\beta\right]. \tag{1.2}$$

iii. *Rolling element fault:* caused due to point defects in the rolling element giving rise to specific frequency components in the vibration spectrum as provided by

$$f_{rv} = \left(\frac{f_r d_\rho}{2b_d}\right) \left[1 - \left(\frac{b_d}{d_\rho} \cos\beta\right)^2\right]. \tag{1.3}$$

iv. *Cage fault:* the rolling elements are held together in their place by an enclosed cage-like structure. Any damage to the cage gives specific a frequency component in the vibration as

$$f_{cv} = \left(\frac{f_r}{2}\right) \left[1 - \left(\frac{b_d}{d_\rho} \cos\beta\right)^2\right], \tag{1.4}$$

where f_{ov}, f_{irv}, f_{rv}, and f_{cv} are the characteristic vibration fault frequency components (in Hz) for the outer raceway, inner raceway, rolling element, cage, respectively. f_r is the rotational frequency. N_b, b_d, d_ρ, and β are the number of balls, ball diameter, ball pitch diameter, and the contact angle between the ball and the races, respectively. The theoretical fault signatures using stator current can be obtained from the corresponding vibration signatures as follows

$$f_{xi} = f_o \pm m f_{xv}, \tag{1.5}$$

where f_{xi} and f_{xv} are the theoretical current and vibration signature of x-type bearing fault condition. f_o is the fundamental supply frequency and m is the set of natural numbers ($m \in \mathbb{N}$.)

1.1.3.2 Stator faults

Stator windings are the most operation critical and fault-prone elements of a SCIM. The main reason for stator faults can be attributed to the deteriorating insulation of the windings with time. The failure modes associated with winding faults are short-circuit, open-circuit, stator-core faults [55]. The insulation degradation causes turn-to-turn defects, and the corresponding stator current spectral signature is given by

$$f_{si} = f_o \left[\frac{m\,(1-s)}{2p} \pm k \right], \tag{1.6}$$

where m and k are positive integers, $m, k \in \mathbb{Z}^+$. The inherent ambiguity of (1.6) and presence of the same signature in case of eccentricity faults limit its use. As an alternative, the following signature has been used to detect the turn-to-turn short-circuit faults [56]

$$f_{si} = f_o \left[\frac{mN_r\,(1-s)}{2p} \pm k \right], \tag{1.7}$$

where N_r are the number of rotor bars, p is the number of poles of the motor, $m \in \mathbb{N}$, $k = 2l + 1$ and $l \in \mathbb{Z}^+$.

1.1.3.3 Broken Rotor Bar fault

Continual running of the motors with unbalanced magnetic pull and inherent eccentricity leads to cracks at the junction between the end-ring and the rotor bars. The resultant rotor asymmetry leads to harmonic components around the supply frequency [57–59] in the stator current spectrum as

$$f_{bi}(k) = (1 \pm 2ks)f_o, \tag{1.8}$$

where s is the slip and $k \in \mathbb{Z}$. The BRB signature in the vibration spectrum is given as

$$f_{bv}(k) = f_r \pm k(f_s - f_r)p, \tag{1.9}$$

where $f_s = N_s/60$ is the synchronous frequency in Hz, with the synchronous speed N_s in rpm.

1.1.3.4 Eccentricity Faults

Eccentricity faults occur due to the presence of an uneven air-gap between the stator and the rotor [53]. Depending on the non-uniform air-gap characteristics, the eccentricity can be classified into different categories, viz; static, dynamic, and mixed conditions. An eccentric rotor can lead to an unbalanced magnetic pull, resulting in BRB and stator-rotor rub. The unbalanced magnetic field induces fault-specific frequency components in the stator current given by [53, 60]

$$f_{ei} = \left[(kN_r \pm n_d)\,\frac{(1-s)}{p} \pm v\right] f_o, \tag{1.10}$$

Where $v = \pm 1, \pm 3, ...$ are the stator time-harmonic order present in the power supply driving the motor, N_r is the number of rotor slots, and the value of n_d decides type of eccentricity as

i. *Static Eccentricity* - The axis of rotation and the rotor axis are same. However, the rotor axis and stator axis are misaligned. As a result, air-gap is stationary but non-uniform and it does not rotate with the rotor. Static eccentricity is caused due to ovality of the stator or poor positioning of the rotor. Mathematically $n_d = 0$ in (1.10). Static eccentricity fault is illustrated in Fig. 1.3(a).

ii. *Dynamic Eccentricity* - With dynamic eccentricity, the rotor-axis and the rotational axis do not coincide. However, the rotational axis and the stator axis are the same, and the minimum air-gap rotates with the rotor. Mathematically, frequency components are modeled by putting $n_d = 1, 2, 3, ...$ in (1.10). Dynamic eccentricity is illustrated in Fig. 1.3(b). The causes of dynamic eccentricity are due to bent rotor shaft, bearing wear, misalignment, and mechanical resonance due to shaft speed oscillation.

iii. *Mixed Eccentricity* - In practice, both the static and dynamic eccentricities exist together. All the motors studied in this thesis have confirmed this fact. The static and dynamic eccentricity coexists, leading to the mixed eccentricity condition. In mixed eccentricity, none of the three centers coincides as illustrated in Fig. 1.3(c).

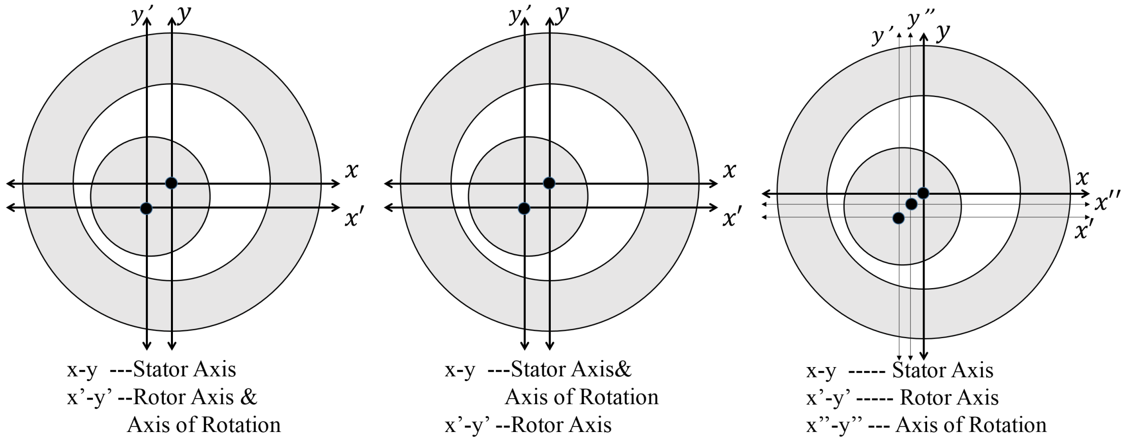

(a) Static eccentricity (b) Dynamic eccentricity (c) Mixed eccentricity

Figure 1.3: Different types of eccentricity faults

The mixed eccentricity condition exists inherently in motors. As a result, most literature uses this mixed eccentricity component to detect the level of eccentricity present. The mixed eccentricity spectral signature in current is defined by (1.11). This component has been used in this thesis for speed estimation.

$$f_{mi} = \left| \frac{1 \pm k(1-s)}{p} \right| f_o. \tag{1.11}$$

For the vibration signal, the mixed eccentricity component is given by [53]

$$f_{mv} = 2f_o \pm f_r. \tag{1.12}$$

This thesis mainly analyzed stator current and motor vibration to detect faults in SCIM. However, other parameters that are analyzed to assess the fault condition of a motor are discussed in the subsequent section.

1.1.4 Choice of Signals for Fault Detection

Multiple signals have been used for condition monitoring of SCIMs [54]. A survey of the keywords from recent publications found stator current to be the most widely used signal, followed by vibration, as shown in Fig. 1.4. A brief review of

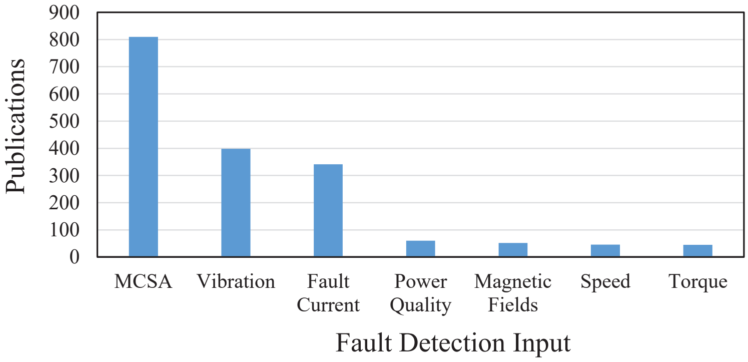

Figure 1.4: Input parameters used for detecting faults in published works from 2011 to June 2020. Data source: Scopus [1].

signals that are used as input for fault detection is given below:

i. *Current* is most popularly used due to its ease of acquisition and low-cost [61, 62] and conventionally known as motor current signature analysis (MCSA). Current detect most of the SCIM faults. It requires only nameplate motor parameters, and the use of clamp-type Hall sensors makes the acquisition non-invasive. The sensors can be clamped around the supply-lines, and their proximity to the motors is inconsequential. However, MCSA requires sophisticated signal processing algorithms for weak fault detection [63], especially for VFD-motors due to the presence of fault-imitating harmonics [64].

ii. *Vibration signals* effectively detect early-stage mechanical faults and have lower spurious harmonic content [65]. Recent use of vibration for fault diagnosis can be found in [66–69]. The use of vibration signals for VFD-motor can be found in [70]. In [71], we have used the inbuilt accelerometer of a smart phone to measure vibration for fault detection. Effective placement of vibration sensors is a significant drawbacks along with its cost and fragility. Also, vibration measurement require elaborate instrumentation.

iii. *Magnetic fields* for detecting faults of SCIMs require the acquisition of stray flux [72], air-gap flux [73], and radial flux [74]. Acquisition of flux needs complex sensor arrangement and fixations for an individual motor. Search coil-based methods require installing pick-up coils near stator slots and the motor frame to capture the flux pattern. However, inaccessible motors and installation of the sensor on existing systems render the use of search coils infeasible. Locating the optimal position of the search coils for capturing the fault-modulated signal is substantially challenging. Moreover, the physical characteristics of the search coil affects the detection procedure.

iv. *Supply voltage modulation* is also used for the detection of SCIM faults [75].

However, the use of voltage requires the sensor to be attached to either of the supply or motor terminals. Also, the acquisition of high-voltage signals requires a sophisticated data acquisition arrangement, which can be costly and unsafe.

v. *Active-reactive power analysis* [76, 77] effective for detecting faults under time-varying loads. Moreover, power analysis can distinguish oscillations due load torque from rotor faults. However, power measurement require the acquisition of voltage, which is disadvantageous.

vi. *Acoustic signals* were employed by [78,79] to detect faults in SCIMs. Though potent for a single motor, its use for a multiple motor environment with several sources of noise is challenging. Specifically, detection and isolation of faults from numerous sources within an enclosed environment impedes the use of acoustic sensors.

vii. *Thermal field analysis* [80], *thermal imaging* [81], and *temperature* [82], although used for fault detection in various heavy industries, are not very popular for SCIMs. Extracting fault-significant information from thermal images is complicated due to the metal enclosures. Although, It can be used for detection of the stator and the bearing related failures.

Signals like flux [83] and instantaneous power factor with phase [77] were used to alleviate the problems faced by MCSA due to load-torque. However, the acquisition of flux and voltage for calculating power factor are major hurdles. As a result, BRB indicators, independent of load-torque oscillations, were proposed [84–86]. Few other signals used for SCIM fault detection are rotational speed [87], efficiency [88], slot harmonics [89], torque [60], and low-voltage off-line testing [90].

In [91], data from multiple sensors like current, vibration, acoustic, and voltage have been integrated using principal components with posterior estimates. The quaternion coefficients of tri-axial vibration and stator current have been used in a decision tree classifier [68]. The use of Sugeno fuzzy integral-based fusion of current and vibration signals is reported in [92]. The use of data from multiple combined sensors reduces the classification errors of a fault detector. However, using multiple expensive sensors for a single motor turns out to be unsuitable for large-scale implementation.

With the logged motor parameter, we need to select an appropriate method for detecting the faults. A review of the recent fault diagnostic procedures are described next.

1.1.5 Review of Existing SCIM Fault Detection and Classification Algorithms

A condition monitoring system for early detection of SCIM faults can significantly enhance the operation efficiency of any industry [16, 93]. Different methods have been proposed in the literature for detecting SCIM faults, as shown in Fig. 1.5. The information from raw time-domain signals from a faulty motor have almost imperceptible features to quantify or classify faults. Example stator current raw signals for different health condition of the SCIM of the experimental setup are shown in Fig. 1.6 to demonstrate this fact.

The central premise of fault diagnosis is concerned with the estimation of fault-frequency components and their amplitudes. Spectral estimation using fast Fourier transform (FFT) [67] and over its envelope [94] has been very accurate in detecting different faults in SCIMs. High-resolution spectral estimators like MUSIC [95, 96] and ESPRIT [97, 98] have gained prominence over the classical power spectrum because of their robustness and resolution capacity for detecting faults under low load conditions. Still, there are concerns over critical issues related to computational complexity and accurate amplitude estimation of the detected fault

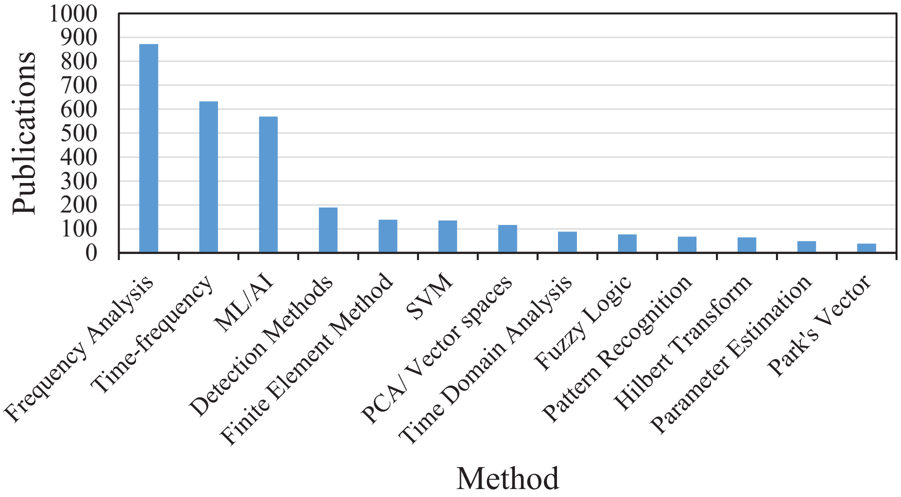

Figure 1.5: Broad classification of methods for detecting faults in published works from 2011 to June 2020. Data source: Scopus [1].

components. Parametric spectral estimators for fault diagnosis using maximum likelihood estimation (MLE) with a given signal model can be found in [99]. Spectral analysis based on total least square methods was developed by [100] for fault detection.

Time-frequency analysis for variable-load conditions using wavelet packet decomposition [101], complex-wavelets [102], and tunable Q-factor wavelets [103] are widely used in literature. The decomposition of the vibration signal into its intrinsic modes using EMD and subsequent classification of faults by a neural network can be found in [104].The use of complete ensemble EMD to avoid mode mixing has been demonstrated in [105]. Faults detection under non-stationarity conditions with variational mode decomposition can be found in [106].

Concentrating the time-frequency energy using phase information with high-order synchrosqueezing is conducted in [107] for fault detection. The use of over-complete dictionaries to represent a signal in the sparse domain and retrieving the frequencies using orthogonal matching pursuit is shown in [108]. A sparsity-based method with group lasso is presented in [109]. In [110], a low-complexity fault detector was designed using the sub-Nyquist strategy. Entropy and mutual information features of vibration and support vector machine (SVM) for classification can be found in [69].

Alternatively, [111] has used linear prediction for recovering fault-specific signals from the noise to detect point faults and general roughness of bearings. Advances in machine learning (ML) tools in conjunction with stationary wavelet extraction, followed by a support vector machine with an artificial immune system for classification was shown in [112]. The remaining useful life of bearings with empirical Bayes was carried out by extracting the features with complete ensemble EMD [113]. Robust thresholding with historical data of a motor was demonstrated in [114]. Simultaneous presence of BRB, eccentricity, and speed oscillations was studied analytically and experimentally in [115]. A method based on the parametric winding function model using current, rotor speed, and torque is presented in [116].

The fault frequency amplitude indicates the fault severity [117, 118]. However, subspace-based methods cannot give exact information about the amplitude of the fault components. Hence, simulated annealing algorithm was used to determine the correct amplitude and fault severity [98]. In [97, 119], least square is used for amplitude estimation. However, least squares estimate is same as computing the DFT for a single component. However, DFT is unsuitable for estimating the amplitude of closely-spaced sinusoids [120, 121]. Moreover, these methods require extra computational resources for their execution when used in conjunction with MUSIC and ESPRIT.

Stator current modulation due to partial BRB is weak. The problem is exacerbated under light load condition when fault components have low amplitude [122] and are close to the fundamental [118]. Motors running partial rotor breakages don't demonstrate any visible degradation in its performance. However with time they result in poor starting performances, excessive vibrations, torque fluctuation, thermal stress, unbalanced magnetic pull leading to multiple broken bars and stator-rotor rub [59, 123]. Hence, early detection of partial breakages are vital for effective predictive maintenance. The fundamental frequency needs to be suppressed without affecting the close fault components. For stationary situations, a sharp notch filter is used [124]. But variable frequency operation with load changes requires the central frequency of the notch filter to track the fundamental component and its cut-off bandwidth to be adaptive to the slip. For unsupervised fault detection, a notch filter with such features is unavailable. We propose an extended Kalman filter-based method for targeted removal of a single dominant component in Chapter 3. The conditioner tracks and attenuates only the fundamental component.

Previously, detection of faults in low load condition were successful using Hilbert modulus with FFT (0.2% slip) [125], Hilbert modulus with ESPRIT (0.33% slip) [126], Teager-Kaiser energy operator (0.4% slip) [127], Fourier analysis [128] (1.38% slip), and [129] (0.11% slip). A high initial sampling of 50 kHz for [129] is disadvantageous for low-cost hardware implementation. Most of the research has concentrated on detecting single and multiple BRB. Detecting partial BRB was demonstrated in [58, 59, 130]. However, the detection of partial BRB under low-slip, for an inverter-fed motor, is yet to be addressed. In this thesis we have detected a partially broken bar for the inverter-fed SCIM with a 0.2% slip.

The extraction of frequency-based features has been the highlight of SCIM fault detection. However, the spectral fault features are numerically suppressed due to the presence of multiple high-magnitude frequency components. For detecting multiple faults and the use of vibration signal, tracking and removing multiple dominant components was necessitated. Methods like Teager-Kaiser energy operator [127], and oblique projection [131], have been mainly used for removing single components. In Chapter 4 we also propose a method that can estimate, track, and eliminate multiple high-magnitude components to condition the input signal and extract the fault features appropriately. The proposed method is adaptive to variable frequency conditions and can remove targeted dominant components without affecting the closely-spaced fault components under low-load situations.

Fault detection and classification literature have been predominantly based on traditional ML approaches, such as neural networks, SVM, random forests, etc. However, the last five years have seen phenomenal growth in the application of deep learning (DL) for fault diagnosis and prognosis [132–134]. Transfer learning [66] has been used to build upon existing networks for accelerating the training process. Razavi et al. [135] have used oversampling to enhance the class imbalanced vibration signal training dataset for machine learning. However, the requirement of large datasets encompassing the overall operating condition of a motor is quite challenging. Moreover, obtaining fault-data from a running plant for training is infeasible due to periodic maintenance. It is still an open problem for the DL models to work when trained using a different motor.

On the other hand, hypothesis testing with generalized likelihood ratio test (GLRT) [131,136] can only detect the presence or absence of the fault-component. The presence of an inherent, non-zero, and low-amplitude fault component in a healthy motor thus results in false alarms. A non-zero magnitude incorporated in the null hypothesis of the GLRT can reduce the false alarms, but it may result in a doubly non-central F-distributed test statistic. Alternatively, we present a simple test based on the minimum distance receiver ([137], Pg. 112) to avoid such complex distributions. The test can account for any fault-like magnitude that might be present in the healthy-motor data. Moreover, unlike DL-based methods, the test requires only a few healthy data cases to determine a threshold.

1.2 Motivations of the Thesis

The adaptation of deep learning (DL) architectures and drive towards an industrial Internet of things have boosted the number of publications in the domain of SCIM fault diagnosis, as observed in Fig. 1.7. However, physics-based models with the capacity to detect the weak-fault signatures can circumvent the infeasibility of obtaining faulty-motor data from a running plant. Some of the existing problems that motivate this thesis are as follows:

i. Majority of the IF-estimators are indirect methods and the frequency information is derived from the time-frequency distribution. A method to directly estimate multiple IFs of an input can be vital.

ii. Available spectral estimators are computationally complex, and the high-resolution estimators are incapable of estimating the amplitude. Moreover, a sequential estimator with data-length independent resolution can be useful for real-time (RT) implementations.

iii. Detecting multiple faults requires removing multiple dominant components dependent on the rotational frequency. Conventional notch filters are not viable for use under variable frequency, and low-slip applications as the filters can suppress the closely-spaced fault components. As evident from the literature, the other methods are mainly useful for removing single components or components with harmonic ordering.

iv. Conventional fault-detectors mainly considers the presence or absence of faults. The GLRT-based methods mainly focus on improving accuracy under noisy conditions. However, it does not assume the inherent fault component that can also be present in a healthy-motor.

v. Industries do not tolerate faults, and periodic maintenance is enforced to avoid stoppages. As a result, the availability of industrial fault data is scarce for training. It is still an open problem for data-driven architectures to train with only available healthy-motor data. Also, algorithms independent of the motor-specification with high-accuracy detection capacity can be advantageous.

1.3 Objective and Contributions of the Thesis

This thesis aims to detect and estimate sinusoidal parameters under stationary as well as non-stationary conditions, and apply the estimates for diagnosing weak faults in SCIMs. The contributions of the thesis are summarized below:

i. The IF estimation of multiple sinusoidal frequency components simultaneously using a linearized-observation and constrained Kalman filter.

ii. The IF estimator is enhanced for eliminating the multiple dominant components, which leads to efficient signal conditioning.

iii. A Rayleigh-quotient-based spectral estimator is proposed, which has high estimation accuracy and is computationally efficient. It can also estimate the amplitude of constituent frequency components efficiently. The spectral estimator has been used to detect various faults of SCIM using both stator current and vibration as input.

iv. We propose a minimum-distance-based detector that can incorporate the inherent fault component information for making the decision.

v. We also propose a Bayesian MAP-based sequential spectral estimator for detecting SCIM faults. The estimator uses a first-order Gauss-Markov process as the prior distribution. The recursive nature of the spectral estimator has enabled its implementation in an IoT-based framework for detecting defects in multiple motors.

vi. Two embedded and hardware realizations are proposed comprising of a SIMULINK Real-time (SLRT) based method for single motor and an IoT-enabled framework for multiple motor health monitoring.

The proposed methods have been tested and validated on a 22-kW SCIM laboratory setup described in section 3.5. The use of vibration has also been validated using the publicly available Case Western Reserve University (CWRU) drive-end, 12 kHz bearing data [15]. The problem statement of the thesis is described in the next section.

1.4 The Problem Statement

Considering the motivations and objectives of this research, we formulate the problem statement using a mathematical model where the n^{th} instance of a band-limited signal $x(n)$, used as an input is given as

$$x(n) = \sum_{i=1}^{q} |A_i| \, e^{j(n\omega_i[n]+\phi_i)} + v(n), \tag{1.13}$$

where $|A_i|$, $\omega_i[n]$, ϕ_i are the individual amplitude, normalized IF, and phase of the i^{th} component, respectively. $\omega_i[n] = 2\pi f_i[n]/F_s$, $j = \sqrt{-1}$, F_s is the sampling rate (samples/s), and e is the exponential operator, respectively. $f_i[n]$ is the IF (in Hz) of the i^{th} component. $v(n)$ is the additive white Gaussian noise with zero mean and variance σ_v^2, i.e., $v[n] \sim \mathcal{N}(0, \sigma_v^2)$. $x(n)$ consists of $\tilde{q}$ number of high-amplitude dominating frequency components out of q. We assume that the frequency has temporal variation. Any diversion otherwise can be accommodated using a constant frequency, i.e., $\omega_i(n) = \omega_i$.

The process of fault detection starts with selecting and recording an appropriate signal that should be convenient to acquire and carries vital features of the fault. The second problem is the pre-conditioning of the input signal to extract maximum fault information. The preprocessing is accomplished by the targeted elimination of $\tilde{q}$ dominant components. The variable frequency drives (VFD) aggravates the problem as the supply frequency can vary with time. After signal conditioning, the third problem is to extract vital features that carry information about the faults. For the model described by (1.13), feature extraction mainly involves the estimation of frequency and amplitude of the remaining $(q - \tilde{q})$ components. Lastly, based on the extracted features, fault detection and identification is carried out.

1.5 Organization of the Thesis

The thesis is organized as follows:

Chapter 1: This chapter provides the background, motivation, and objective of this thesis to detect and estimate low-amplitude frequency components and their utility in diagnosing SCIM faults.

Chapter 2: Proposes a generalized framework for RT tracking of multiple time-varying sinusoidal frequencies of a non-stationary signal.

Chapter 3: Introduces the Rayleigh-quotient-based spectral estimator and uses it for detecting partially broken rotor bar faults using stator current. This chapter uses an EKF-based method for eliminating the single dominant supply frequency component from the stator current. However, the necessity of eliminating multiple dominant components from vibration signals to detect different faults takes us to the next chapter. The SCIM experimental setup is also described in this chapter.

Chapter 4: This chapter has modified the IF-estimator of Chapter 2 to eliminate multiple dominant components from an input signal. A minimum distance-based detector is proposed for generalized fault detection. Using the Rayleigh-quotient-based spectral estimator, we show the overall framework's utility for detecting multiple SCIM faults using vibration signatures.

Chapter 5: Proposed a Bayesian MAP-based sequential spectral estimator for detecting SCIM faults using a single-phase stator current input. The method has been used for presenting an online IoT-based framework for detecting defects in multiple induction motors.

Chapter 6: Describes two hardware and embedded implementations for detecting SCIM faults. The first system discussed is a SLRT-based hardware for detecting faults of single motor. Whereas, the second application shows the use of an IoT-based framework for detecting faults in a factory-setup with multiple SCIMs.

Chapter 7: This chapter concludes the thesis and provides a peek into future research directions.

A pictorial representation of different parts of the thesis and the chapter dependencies are provided in Fig. 1.8.

1.6 Conclusions

This chapter provides an overview of the existing estimators of frequency under stationary and non-stationary conditions. This is followed by a description of different faults in SCIMS, their signatures, and methods for detecting the faults.

The survey of existing IF-estimators have shown the scarcity of direct estimators of frequency. Most methods estimate the time-frequency distribution before finding the frequency. On the other hand, high-resolutions spectral estimators are incapable of estimating the amplitude of constituent components and require model-order information. Fault detection of SCIMs can be classified into physics-based and data-driven methods. The physics-based models mainly estimate fault-characteristic frequency components and spectral-leakage is a major hurdle in the detectability of faults. Notch-filters can only remove single dominant component or ordered-harmonics. Alternatively, data-driven methods need difficult-to-obtain fault-condition data. As a consequence, targeted removal of dominant components in conjunction with high-resolution spectral estimators can detect weak faults under a variety of conditions. The chapter is concluded by the motivation, objective, and contributions of this dissertation along-with its organization.

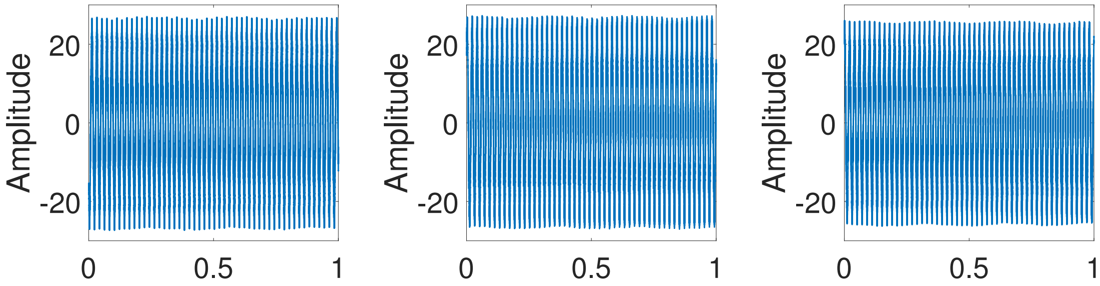

(a) Healthy motor (0.2% slip) (b) Broken rotor bar (0.2% slip) (c) Outer Raceway (0.2% slip)

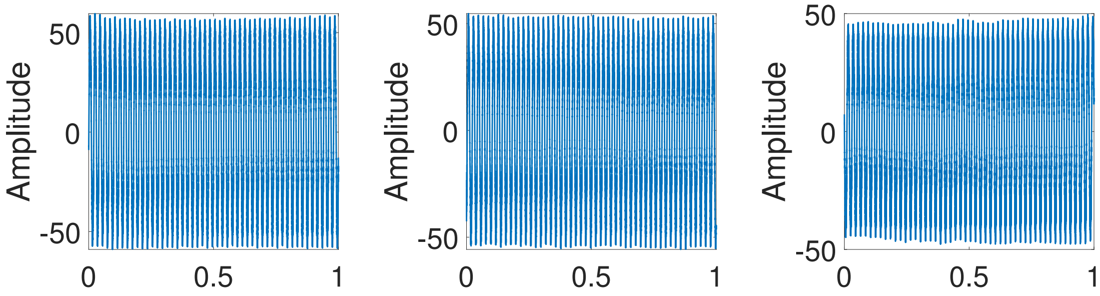

(d) Healthy motor (1.93% slip) (e) Broken rotor bar (1.8% slip) (f) Outer Raceway (2% slip)

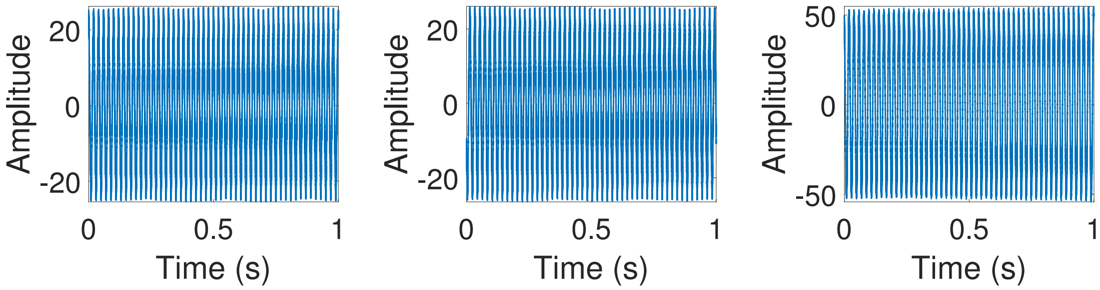

(g) Cage (0.2% slip) (h) Inner Racway (0.2% slip) (i) Inner Racway (2.26% slip)

Figure 1.6: Raw time domain stator current for different running and fault conditions of the motor.

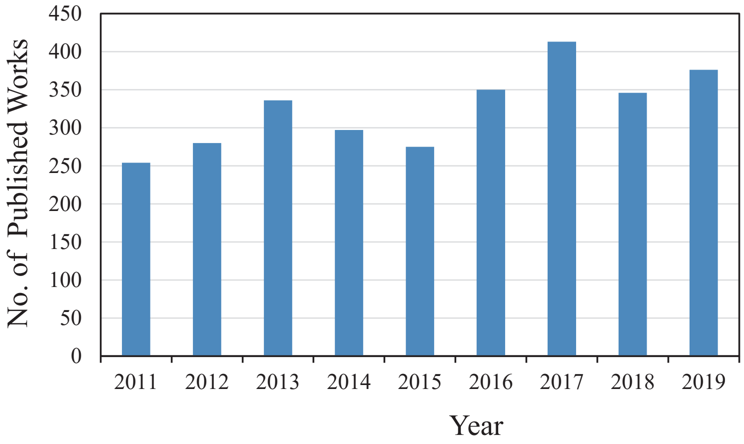

Figure 1.7: Year-wise distribution of published works on Fault diagnosis of SCIMs. Data source: Scopus [1]

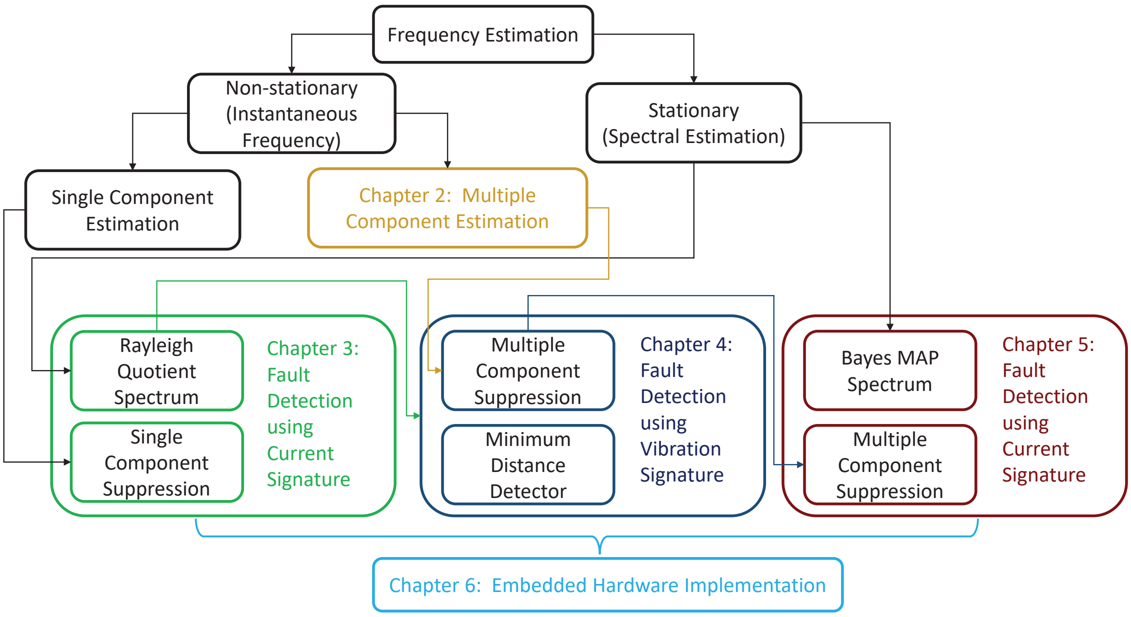

Figure 1.8: The organization of the thesis and chapter dependencies

CHAPTER 2

Direct Estimation of Multiple Time-varying Frequencies of Non-stationary Signals

This chapter proposes a generalized framework for real-time (RT) tracking of multiple time-varying sinusoidal frequencies of a non-stationary signal. The non-stationary signal is modeled as a TVAR process. A non-linear state-space model is formed to truly represent the TVAR process, considering the frequencies as state variables. We have defined the observation and its Jacobian by the modified roots of a polynomial formed by the state variables. Numerical derivatives have been substituted by the analytic form of the Jacobian matrix for improved numerical accuracy. A constrained Kalman filter is then applied for RT tracking of the frequencies. We have compared the statistical performance of the proposed method with other established methods using Monte-Carlo simulations. The proposed method is found to have superior error performance under different conditions of chirp-rate, resolution, noise variance, and abrupt changes in frequency. Additionally, we have taken the bat echolocation signal, gravitational waves of a binary black hole merger, and abrupt change in mains frequency supplied to a three-phase squirrel cage induction motor as practical examples to demonstrate the applicability and efficacy of the proposed method in real-world scenarios.

2.1 Contributions of the Chapter

In this chapter, we present a method for sequential estimation of multiple time-varying frequency components simultaneously. For this, we will model the non-stationary signal as a TVAR process. The model can incorporate information about multiple components. Additionally, through statistical results, the performance of the proposed method for different chirp-rates will be evaluated. We will derive the analytic form of the non-linear observation matrix and apply a constrained Kalman filter to estimate the multiple time-varying frequencies. For a non-stationary signal with slowly varying parameters, it is assumed that the TVAR coefficients are constant at each instant [138]. Existing literature has estimated the TVAR model parameters using Bayesian maximum a posteriori (MAP) estimate [5] when the prior information about the parameters is known. Alternatively, maximum likelihood estimation (MLE) [4] can be used when the prior information is unavailable. Additionally, it will be shown that unlike conventional methods, over-estimation of the model order is not required, and satisfactory resolution can be achieved with correct knowledge about the model order. It will be shown that the proposed sequential estimator is capable of estimating the frequencies of closely-spaced components. Also, the error-performance and the recovery time during an abrupt change of frequency of the IF estimator will be shown to be superior. Three real-world examples for IF estimation of gravitational waves, bat echolocation signal, and stator current of an induction motor are used to demonstrate the practical application of the method. The novelty of the present work can be enumerated as

1. Majority of the literature uses a time-frequency (TF) representation to find the energy distribution and then maximizes the distribution for IF estimation. The methods are non-sequential and require a batch of windowed data to find the TF distribution. On the other hand, sequential estimation using a linearized Kalman filter has mainly focused on estimating a single dominant frequency or its harmonics. This chapter evaluates the frequency of multiple time-varying components using a linearized and constrained Kalman filter. The efficacy of the method has been established with various Monte-Carlo (MC) simulations, and its comparison with established methods like SST, wavelet-SST (WSST), RM, and S-transform.

2. We have avoided numerical derivatives by deriving the analytic closed-form of the observation matrix and its Jacobian for multiple frequencies leading to higher accuracy.

3. We have also used a constrained optimization to find the optimum gain of the Kalman filter for resolving the inherent phase unwrapping problem of frequency estimates.

Outline: We have structured the chapter as follows: Section 2.2 describes the signal model and defines the problem. Section 2.3 proposes the frequency estimation methodology for the complex exponential model and extends it to a two-component real signal, which will be used for evaluation and analysis. Subsequently, we demonstrate the efficacy of the proposed method with simulated and real-world data, along with performance comparisons with existing state-of-the-art frequency estimation methods in Section 2.4. Section 2.5 concludes the chapter.

2.2 The Time-varying Autoregressive Process

A p-component signal $x[n]$ with individual components $\tilde{x}_i[n]$ is represented as

$$x[n] = \sum_{i=1}^{p} \tilde{x}_i[n] + v[n], \tag{2.1}$$

where

$$\tilde{x}_i[n] = |A_i| e^{j(n\omega_i[n]+\phi_i)}, \tag{2.2}$$

and $\omega_i[n]$, $|A_i|$, ϕ_i are the instantaneous normalized frequency, amplitude, and phase of the i^{th} component, respectively. $\omega_i[n] = 2\pi f_i[n]/F_s$, and $j = \sqrt{-1}$. $f_i[n]$ and F_s are the i^{th} instantaneous signal frequency (Hz) and sampling rate (samples/s), respectively. $v[n]$ is the additive white Gaussian noise with zero mean and variance $\boldsymbol{R} = \sigma_v^2$, i.e., $v[n] \sim \mathcal{N}(0, \sigma_v^2)$. We want to estimate $\omega_i[n]$ of (2.2) for every i, sequentially. p is defined as the number of components and is assumed to be known. Alternatively, [4, 5] have estimated the number of components of a time-varying process.

Assimilating the initial phase into the amplitude of (2.2), we have $\tilde{x}_i[n] = A_i e^{jn\omega_i[n]}$ with $A_i = |A_i|\, e^{j\phi_i}$. We model $\tilde{x}_i[n]$ as an AR process for slowly-varying parameters by assuming a frozen state with constant coefficients (i.e., $\omega_i[n] \approx \omega_i$) for a short duration [138] as

$$\tilde{x}_i[n] = e^{j\omega_i} \tilde{x}_i[n-1]. \tag{2.3}$$

The z-transform of (2.3) gives

$$\left(1 - e^{j\omega_i} z^{-1}\right) \tilde{X}_i(z) = 0, \tag{2.4}$$

where the z-transform of $\tilde{x}_i(n)$ is given by $\tilde{X}_i(z)$. We define the polynomial $A(z)$ having roots $e^{j\omega_i}$ as

$$A(z) = \prod_{i=1}^{p} \left(1 - e^{j\omega_i} z^{-1}\right). \tag{2.5}$$

From (2.4), we see that $A(z)\tilde{X}_i(z) = 0$. Defining $\tilde{x}[n] = \sum_{i=1}^{p} \tilde{x}_i[n]$, with its z-transform given as $\tilde{X}(z) = \sum_{i=1}^{p} \tilde{X}_i(z)$, we can prove that $A(z)\tilde{X}(z) = 0$. Therefore,

$$\tilde{X}(z) \prod_{i=1}^{p} \left(1 - e^{j\omega_i} z^{-1}\right) = 0; \tag{2.6}$$

hence,

$$\tilde{X}(z) \left\{ \begin{array}{l} 1 - z^{-1} \sum\limits_{i=1}^{p} e^{j\omega_i} + z^{-2} \sum\limits_{i=1}^{p} \sum\limits_{j'=1, i \neq j'}^{p} e^{j\omega_i} e^{j\omega_{j'}} \\ -z^{-3} \sum\limits_{i=1}^{p} \sum\limits_{j'=1}^{p} \sum\limits_{k=1, i \neq j' \neq k}^{p} e^{j\omega_i} e^{j\omega_{j'}} e^{j\omega_k} + \\ \cdots (-1)^{p+1} z^{-p} \prod\limits_{i=1}^{p} e^{j\omega_i} \end{array} \right\} = 0. \tag{2.7}$$

The inverse z-transform of (2.7), gives the observation model as a non-linear function of the frequencies as $\tilde{x}[n] = h(\boldsymbol{\theta}[n])$, and $\boldsymbol{\theta}[n]$ is the state vector defined as

$$\boldsymbol{\theta}[n] = \left[\omega_1[n], \omega_2[n], \cdots, \omega_p[n]\right]^T, \quad 0 \leq \omega_i[n] < 2\pi,$$

where $(\cdot)^T$ denotes the transpose operation. A signal with multiple time-varying frequency components $\boldsymbol{\theta}[n]$ can be represented by a p^{th} order TVAR process [139] with time-varying parameters $a_i[n]$ as

$$x[n] = \sum_{i=1}^{p} a_i[n]x[n-i] + v[n]. \tag{2.8}$$

Using $x[n] = \tilde{x}[n] + v[n]$, and putting the value of $\tilde{x}[n]$, we get

$$x[n] = h(\boldsymbol{\theta}[n]) + v[n]. \tag{2.9}$$

Comparing (2.8) and (2.9), we get $h\left(\boldsymbol{\theta}[n]\right)$ as

$$h\left(\boldsymbol{\theta}[n]\right) = \begin{bmatrix} e^{j\omega_1[n]} + e^{j\omega_2[n]} + \cdots + e^{j\omega_p[n]} \\ -e^{j\omega_1[n]}e^{j\omega_2[n]} - \cdots - e^{j\omega_{p-1}[n]}e^{j\omega_p[n]} \\ \vdots \\ (-1)^{p+1}\left(e^{j\omega_1[n]}e^{j\omega_2[n]}\cdots e^{j\omega_p[n]}\right) \end{bmatrix}^T \boldsymbol{x}[n-1], \tag{2.10}$$

where $\boldsymbol{x}[n] = \begin{bmatrix} x[n] & x[n-1] & \cdots & x[n-p+1] \end{bmatrix}^T$. Algorithm 1 constructs $h\left(\boldsymbol{\theta}[n]\right)$ online using $\boldsymbol{x}[n-1]$, $\boldsymbol{\theta}[n]$, and p.

Algorithm 1 Construction of $h\left(\boldsymbol{\theta}[n]\right)$

```
Input: $\boldsymbol{\theta}[n] = [\omega_1[n], \ldots, \omega_p[n]]^T$, $\boldsymbol{x}[n-1]$, $p$
Output: $h\left(\boldsymbol{\theta}[n]\right)$
Form the polynomial roots by the vector $\boldsymbol{r} = \exp(j\boldsymbol{\theta}[n])$
Find the coefficients of the polynomial with roots $\boldsymbol{r}$. MATLAB uses the function 'poly.' $\boldsymbol{b} = poly(\boldsymbol{r})$ and $\boldsymbol{b} \in \mathbb{C}^{(p+1)}$.
$h\left(\boldsymbol{\theta}[n]\right) = [\boldsymbol{b}]^T_{i=2,3,\ldots,p+1}\,\boldsymbol{x}[n-1]$, where $[\boldsymbol{b}]^T_{i=2,3,\ldots,p+1}$ is the transpose of $\boldsymbol{b}$ with the first element removed.
```

2.3 Time-varying Frequency Estimation

The time-varying parameters of (2.8) can be estimated using the Kalman filter. The estimated parameters then can be used to estimate the power spectrum as given by (2.11).

$$P_x(\omega, n) = \hat{\sigma}_v^2 \bigg/ \left| \sum_{k=1}^{p} \hat{a}_i[n] e^{-jk\omega} \right|^2, \tag{2.11}$$

where $\hat{a}_i[n]$ and $\hat{\sigma}_v^2$ are the estimated time-varying parameters and observation noise variance, respectively. However, our aim is to estimate the frequency directly. Direct estimation requires solving the non-linear equation of (2.7).

2.3.1 Direct Frequency Estimation

In this work, we directly estimate the time-varying sinusoidal frequencies using the observation model given by (2.9). A first-order Gauss-Markov process define the state update as

$$\boldsymbol{\theta}[n] = \boldsymbol{\theta}[n-1] + \boldsymbol{u}[n], \tag{2.12}$$

where $\boldsymbol{u}[n]$ is zero-mean white Gaussian with covariance $\boldsymbol{Q}$, and $\boldsymbol{Q} = \sigma_u^2 \boldsymbol{I}$, and $\boldsymbol{I}$ is a $(p \times p)$ identity matrix. Therefore, $\boldsymbol{u}[n] \sim \mathcal{N}(\mathbf{0}, \sigma_u^2 \boldsymbol{I})$, and $\mathbf{0}$ is a vector with p zeros. Using a first-order Taylor expansion and neglecting the higher-order terms, we have $h(\boldsymbol{\theta}[n])$ as

$$h(\boldsymbol{\theta}[n]) = h(\hat{\boldsymbol{\theta}}[n|n-1]) + \left[\frac{\partial h(\boldsymbol{\theta}[n])}{\partial(\boldsymbol{\theta}[n])} \right]_{\boldsymbol{\theta}[n] = \hat{\boldsymbol{\theta}}[n|n-1]} \Big(\boldsymbol{\theta}[n] - \hat{\boldsymbol{\theta}}[n|n-1] \Big), \tag{2.13}$$

where $\hat{\boldsymbol{\theta}}[n|m] = \mathcal{E}(\boldsymbol{\theta}[n] | x[m], x[m-1], \ldots, x[m-p+1])$ and $\mathcal{E}(\cdot)$ is the expectation operator. Now substituting the value of $h(\boldsymbol{\theta}[n])$ from (2.13) into (2.9), we obtain the linear observation model as

$$x[n] = h(\hat{\boldsymbol{\theta}}[n|n-1]) + \boldsymbol{H}[n] \Big(\boldsymbol{\theta}[n] - \hat{\boldsymbol{\theta}}[n|n-1] \Big) + v[n],$$

where $\boldsymbol{H}[n] = \frac{\partial h(\boldsymbol{\theta}[n])}{\partial(\boldsymbol{\theta}[n])}$, evaluated at $\boldsymbol{\theta}[n] = \hat{\boldsymbol{\theta}}[n|n-1]$, and can be decomposed (proof in Appendix B) as

$$\boldsymbol{H}[\boldsymbol{n}] = (\boldsymbol{\phi} \boldsymbol{W} \boldsymbol{x}[n-1])^T, \tag{2.14}$$

with $\boldsymbol{\phi} = j \operatorname{diag}\begin{pmatrix} e^{j\omega_1[n]} & \dots & e^{j\omega_p[n]} \end{pmatrix}$, and

$$\boldsymbol{W} = \begin{bmatrix} 1 & -\sum\limits_{i=2}^{p} e^{j\omega_i[n]} & \sum\limits_{i=2}^{p} \sum\limits_{j'=2, i\neq j'}^{p} e^{j\omega_i[n]} e^{j\omega_{j'}[n]} & \cdots & (-1)^{p+1} \prod\limits_{i=2}^{p} e^{j\omega_i[n]} \\ 1 & -\sum\limits_{i=1, i\neq 2}^{p} e^{j\omega_i[n]} & \sum\limits_{i=1}^{p} \sum\limits_{j'=1, i\neq j'\neq 2}^{p} e^{j\omega_i[n]} e^{j\omega_{j'}[n]} & \cdots & (-1)^{p+1} \prod\limits_{i=1, i\neq 2}^{p} e^{j\omega_i[n]} \\ . & . & . & . & . \\ 1 & -\sum\limits_{i=1}^{p-1} e^{j\omega_i[n]} & \sum\limits_{i=1}^{p-1} \sum\limits_{j'=1, i\neq j'}^{p-1} e^{j\omega_i[n]} e^{j\omega_{j'}[n]} & \cdots & (-1)^{p+1} \prod\limits_{i=1}^{p-1} e^{j\omega_i[n]} \end{bmatrix}.$$

The dimension of the matrices are given as $\boldsymbol{\phi} \in \mathbb{C}^{p\times p}$, $\boldsymbol{W} \in \mathbb{C}^{p\times p}$, and $\boldsymbol{H}^T[n] \in \mathbb{C}^p$. We use Algorithm 2 to construct $\boldsymbol{W}$. Using the values of $h(\boldsymbol{\theta}[n])$, $\boldsymbol{H}[n]$, and the constrained Kalman filter [140] approach, we propose Algorithm 3 for estimating the IFs of multiple components. The optimization finds the optimal Kalman gain so that the frequency estimate of the complex exponential is restricted within 0

Algorithm 2 Construction of $\boldsymbol{W}$

```
Input: $\boldsymbol{\theta}[n] = [\omega_1[n], \omega_2[n], \cdots, \omega_p[n]]^T$, $p$
Output: $\boldsymbol{W}$
for all $i$ such that $1 \leq i \leq p$ do
    $\boldsymbol{\theta}[n] \leftarrow \tilde{\boldsymbol{\theta}}[n] = [\cdots, \omega_{i-1}[n], \omega_{i+1}[n], \cdots]^T$
    Form roots as $\tilde{\boldsymbol{r}} = \exp(j\tilde{\boldsymbol{\theta}}[n])$
    $\boldsymbol{W}(i,:) = poly(\tilde{\boldsymbol{r}})$
end for
```

to 2π. The Kalman gain is given as

$$\begin{aligned}
&\hat{\boldsymbol{K}} = \underset{K}{\operatorname{argmin}}\,\operatorname{Trace}\left[(\boldsymbol{I}-\boldsymbol{K}\boldsymbol{H}[n])\,\boldsymbol{P}[n|n-1](\boldsymbol{I}-\boldsymbol{K}\boldsymbol{H}[n])^{H} + \boldsymbol{K}\boldsymbol{R}\boldsymbol{K}^{H}\right] \\
&\text{subject to : } 0 < \hat{\theta}_i[n|n-1] + K_i\left(x[n] - h(\hat{\boldsymbol{\theta}}[n|n-1])\right) < 2\pi, \quad \forall i
\end{aligned} \tag{2.15}$$

in which $\boldsymbol{K}$, $\boldsymbol{R}$, $\boldsymbol{P}$ are the Kalman gain, observation error covariance, and state error covariance, respectively. K_i is the Kalman gain for the state θ_i, and $i = 1, 2, \ldots, p$. $\boldsymbol{I}$ is an $p \times p$ identity matrix and $(\cdot)^H$ denotes the conjugate transpose operation. The quadratic convex optimization problem with affine constraints was solved using *fmincon* program of MATLAB. It can also be solved using a semidefinite problem solver *SDPT3* from MATLAB [141].

Algorithm 3 Sequential estimation of multiple frequencies

```
Input: $\hat{\boldsymbol{\theta}}[n-1]$, $x[n]$, $\boldsymbol{P}[n-1]$, $\boldsymbol{Q}$, $\boldsymbol{R}$.
Output: $\hat{\boldsymbol{\theta}}[n]$, $\boldsymbol{P}[n]$.
 1: for all $n$ such that $n > p$ do
 2:     Prediction of state
            $\hat{\boldsymbol{\theta}}[n|n-1] = \hat{\boldsymbol{\theta}}[n-1]$
 3:     Prediction of Minimum Mean Square Error
            $\boldsymbol{P}[n|n-1] = \boldsymbol{P}[n-1] + \boldsymbol{Q}$
 4:     Evaluation of Kalman Gain
            $\boldsymbol{K} = \boldsymbol{P}[n|n-1]\boldsymbol{H}^T[n]\{\boldsymbol{H}[n]\boldsymbol{P}[n|n-1]\boldsymbol{H}^T[n] + \boldsymbol{R}\}^{-1}$
 5:     Correction
            $\hat{\boldsymbol{\theta}}[n] = \hat{\boldsymbol{\theta}}[n|n-1] + \boldsymbol{K}\left\{x[n] - h(\hat{\boldsymbol{\theta}}[n|n-1])\right\}$
 6:     If ($\hat{\theta}_i[n] < 0$) or ($\hat{\theta}_i[n] > 2\pi$)
 7:         Re-evaluate the Kalman gain with (2.15) and go to step 5.
 8:     End If
 9:     Minimum Mean Square Error
            $\boldsymbol{P}[n] = \boldsymbol{I} - \boldsymbol{K}\boldsymbol{H}[n]\boldsymbol{P}[n|n-1]$
10: end for
```

2.3.2 Example: Synthetic Signal Consisting of Two Sinusoids with Time-varying Frequencies

For real sinusoids, two parameters define a single component. The TVAR model for time-varying real sinusoid with two components ($p = 2$) is given by (2.16)

$$x[n] = \sum_{i=1}^{2p} a_i[n]x[n-i] + v[n], \tag{2.16}$$

For real sinusoids, the polynomial of (2.5) is modified as

$$\begin{aligned} A(z) &= \prod_{i=1}^{p} \left(1 - e^{-j\omega_i} z^{-1}\right)\left(1 - e^{j\omega_i} z^{-1}\right) \\ &= \prod_{i=1}^{p} \left(1 - 2z^{-1}\cos\omega_i + z^{-2}\right). \end{aligned} \tag{2.17}$$

Therefore,

$$\begin{aligned} h(\boldsymbol{\theta}[n]) &= 2\left(\cos\omega_1 + \cos\omega_2\right)x[n-1] - \left(2 + 4\cos\omega_1\cos\omega_2\right)x[n-2] \\ &\quad +2\left(\cos\omega_1 + \cos\omega_2\right)x[n-3] - x[n-4]. \end{aligned} \tag{2.18}$$

From (2.18), we see that the observation requires four parameters for a model with two time-varying real sinusoids. The Jacobian of (2.18) is given by

$$\boldsymbol{H}[n] = \frac{\partial h(\boldsymbol{\theta}[n])}{\partial(\boldsymbol{\theta}[n])} = \left[\begin{array}{cc} \dfrac{\partial h(\boldsymbol{\theta}[n])}{\partial\omega_1[n]} & \dfrac{\partial h(\boldsymbol{\theta}[n])}{\partial\omega_2[n]} \end{array}\right]. \tag{2.19}$$

Solving (2.19) we have $\boldsymbol{H}[n]$ as

$$\boldsymbol{H}[n] = \left[\left[\begin{array}{ccc} -2\sin\omega_1[n] & 4\cos\omega_2[n]\sin\omega_1[n] & -2\sin\omega_1[n] \\ -2\sin\omega_2[n] & 4\cos\omega_1[n]\sin\omega_2[n] & -2\sin\omega_2[n] \end{array}\right]\left[\begin{array}{c} x[n-1] \\ x[n-2] \\ x[n-3] \end{array}\right]\right]^T.$$

The construction of a generalized model for multiple time-varying sinusoids is quite challenging. However, naturally occurring signals are real and sinusoidal. Hence, for real-world applications, an analytic signal is first obtained using Hilbert transformation. The tools developed for complex exponential are then applied to estimate the IF. The bat-echolocation problem is one such example, as will be shown in Section 2.4.3.

2.4 Simulation Results, Real-world Examples, and Discussions

We model signals having time-varying frequencies $\omega_i[n]$ to simulate various scenarios for testing our algorithm as

$$\omega_i[n] = \frac{2\pi}{F_s}\left(\alpha_i + \frac{\beta_i n}{F_s}\right), \tag{2.20}$$

where α_i, β_i are the initial frequency (Hz) and chirp-rate, respectively. $F_s = 200$ samples/s. The initial values of $\boldsymbol{R}$, $\boldsymbol{Q}$, and $\boldsymbol{P}$ for the simulations are determined using the Kalman filter-based particle swarm optimization [142].

2.4.1 General Frequency Estimation Result

For the first simulation, we consider a signal with two distant time-varying frequency components ($\alpha_1 = 10, \alpha_2 = 20, \beta_1 = \beta_2 = 1$) having a constant 10 Hz difference. The true and estimated frequency components are shown in Figure 2.1.

Next, we consider two closely-spaced components $\omega_1[n]$ and $\omega_2[n]$ ($\alpha_1 = 10, \alpha_2 = 11, \beta_1 = \beta_2 = 1$) with a constant 1 Hz difference between them as illustrated in Fig. 2.2. The SNR of individual components for both test cases is chosen as 40

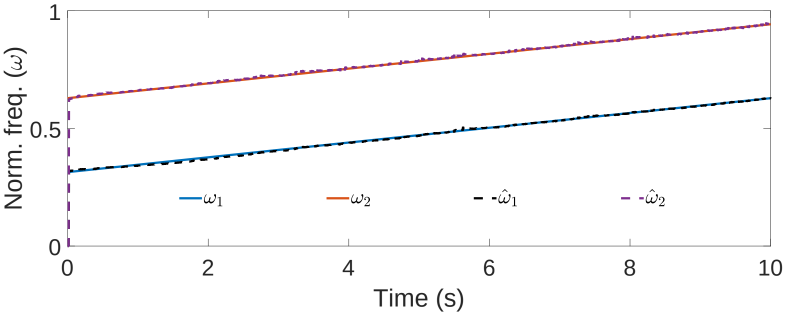

Figure 2.1: Frequency estimate of well-separated sinusoids with a constant 10 Hz difference, $\Delta\omega = 0.1\pi$ radians/sample, and SNR = 40 dB

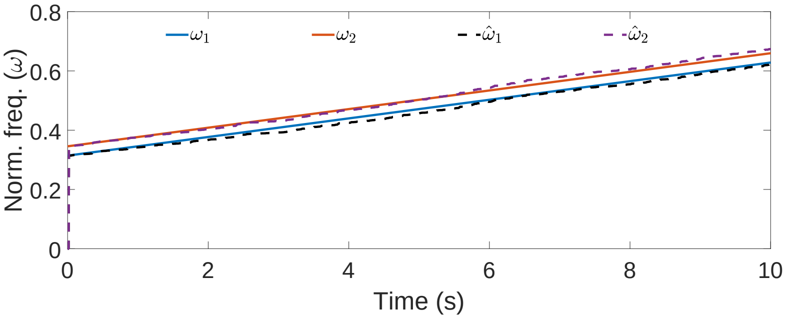

Figure 2.2: Frequency estimate of closely spaced sinusoids with constant 1 Hz difference, $\Delta\omega = 0.01\pi$ radians/sample, and SNR = 40 dB.

dB.

In Fig. 2.3, estimation of two quadratic components with different chirp-rates are demonstrated. The normalized frequencies of the two components are $\omega_1[n] = 0.01\pi(10 + n^2/F_s^2)$ and $\omega_2[n] = 0.01\pi(20 + 3n^2/F_s^2)$ and the SNR is taken as 40 dB.

A compelling case with two overlapping components is shown in Fig. 2.4. The first frequency component $\omega_1[n]$ is linear ($\alpha_1 = 12$, $\beta_1 = 2$). Whereas, the second component $\omega_2[n] = 0.01\pi(10+0.4n^2/F_s^2)$ is a quadratic function of time. The true components has cross-over at 5.45 seconds. It is observed that the frequency estimates do not intersect, as shown in the inset of Fig. 2.4. However, the individual trajectory information is preserved after the crossover, as shown in Fig. 2.4. The

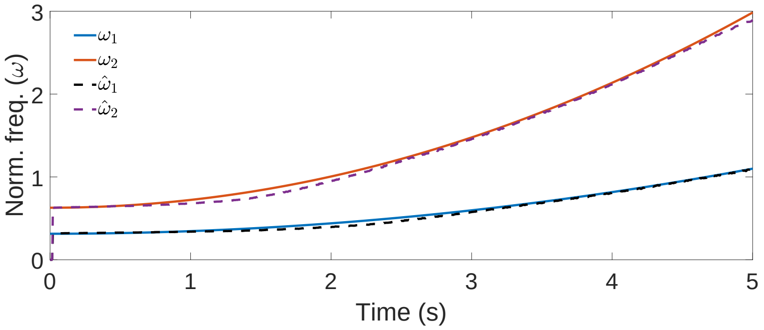

Figure 2.3: Frequency estimate of non-linear components with nonlinear frequencies as $f_1(t) = 10 + t^2$ and $f_2(t) = 20 + 3t^2$, with SNR = 40 dB.

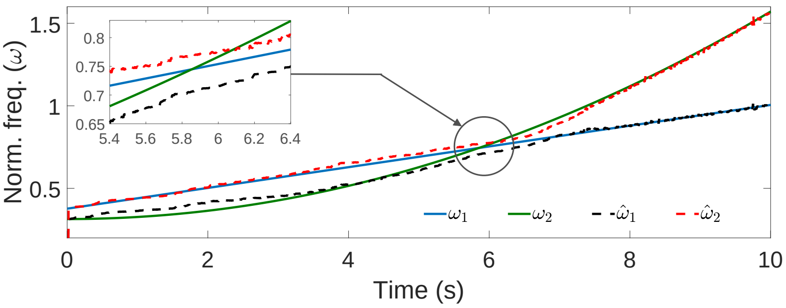

Figure 2.4: Frequency estimate of closely-spaced mixed-function sinusoids with initial 1 Hz difference. $f_1(t) = 11 + 2t$, $f_2(t) = 10 + 0.4t^2$.

experiment indicates good performance for components that are closely-spaced and have quadratic IF. The frequency estimate for an abrupt change in frequency of a single component is demonstrated in Fig. 2.5(a), where $\omega_1[n] = 0.01\pi(10+2n/F_s)$ was changed to $\omega_1[n] = 0.01\pi(30 + 2(n - 1000)/F_s)$ at $n = 1000$. This resulted in a sharp change of $\omega_1[n]$ from 0.2π to 0.3π at 5s. In Fig. 2.5(b), one fixed frequency component, and another having an abrupt change in frequency are tracked together. It is observed that a sharp change in one component affects the other component's estimation briefly.

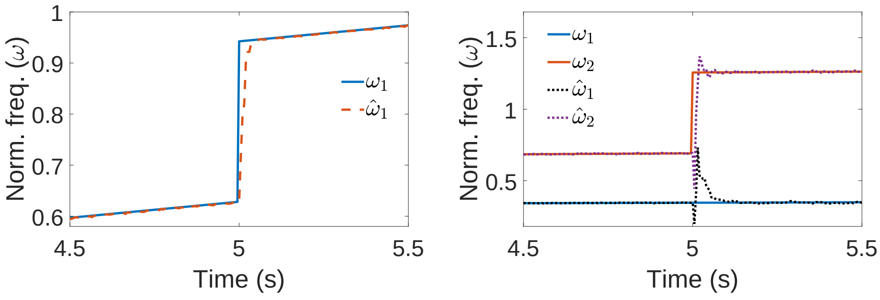

(a) Single component (b) Dual component

Figure 2.5: Frequency estimate with the proposed method with an abrupt change at 5 seconds and 60 dB SNR.

2.4.2 Statistical Evaluation of the Frequency Estimates

Different statistical measures are adopted to determine the performance of the IF estimator. A comparison with four established methods for IF estimation are also carried out. The compared methods are Gaussian-windowed STFT, Morlet-WSST [33], Fourier-SST [28], and reassignment method (RM) [28]. The STFT, RM, and SST used a Gaussian window with $\sigma = 0.025$. The IF of the methods compared are extracted from the TF-distribution by extracting the ridge as proposed in [28]. For WSST, the ridge is extracted with the method given in [33]. Normalized mean-squared error (NMSE) is used to compare the methods in terms of SNR, chirp-rate, resolution, and the performance under an abrupt change of frequency. The NMSE is defined as

$$\text{NMSE} = \frac{1}{ML}\sum_{m=1}^{M}\sum_{n=0}^{L-1}\left(\frac{\omega[n]-\hat{\omega}[n]}{\omega[n]}\right)^2, \tag{2.21}$$

where $\omega[n]$ and $\hat{\omega}[n]$ are the true and estimated IF at n^{th} instant, L is the length of the sequence, and M is the total number of MC simulation. 1000 MC simulations for different noise realizations are used to evaluate the NMSE.

Figure 2.6 compares the performance of all the methods under different SNR

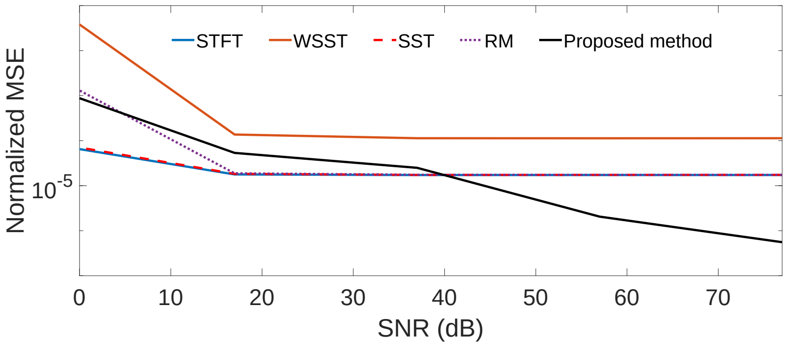

Figure 2.6: NMSE for frequency estimation at different SNR levels with 1000 Monte-Carlo simulations for each SNR.

levels. The NMSE of the proposed method for estimating a single component ($\alpha_1 = 10$, $\beta_1 = 2$) is high when the noise is high. However, with increasing SNR, the NMSE of the proposed method decreases drastically compared to the other methods. It is observed that the NMSE of the other methods converges asymptotically to particular error variances. When the SNR increases, the proposed estimator starts giving more priority to the measurement than the model. As a result, the NMSE decreases with increasing SNR when compared to the other methods. The performance of the estimator under low-SNR can be improved by online estimation of the noise parameters using expectation maximization [43].

The validity of IF estimators revolve around the assumption that the frequency components vary slowly with time. In the next simulation, we investigate the NMSE for signals having different chirp-rates. As observed in Fig. 2.7, the proposed method has an NMSE, which is quite less for a constant component. The NMSE increases slightly with increasing chirp-rate. However, it is lower than the other methods within the chirp-rate range $\beta_1 \in [0, 2]$. For the simulation, we have considered a single frequency component with different chirp-rates ($\alpha_1 = 10$, and β_1 was varied from 0 to 2 Hz/s). The NMSE for each chirp-rate is calculated for 1000 trials with different realization of noise having a constant SNR of 60 dB.

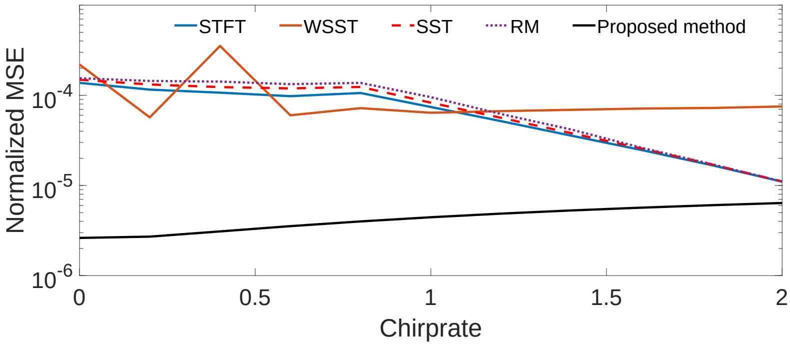

Figure 2.7: Variation of NMSE versus the chirp-rate with 1000 Monte-Carlo simulations.

For multiple components, it is essential to evaluate performance of the estimator when the components are close to each other. Figure 2.8 shows how the frequency difference between the two components in a signal affects the estimation accuracy. Two linear frequencies with different spacing are used for the simulation. The spacing between the components is kept constant for 1000 trials with different noise realizations, and the NMSE is assessed. The SNR of each component is fixed at 60 dB. The NMSE is evaluated between the true and estimated mean-frequency instead of the individual components. Due to better localization of energy in the time-frequency plane, RM, SST, and WSST perform better than STFT, as observed in Fig. 2.8. However, the error of the proposed method is lower than the others, and it could separate the closely-spaced components even though the estimation was carried out recursively. As the separation increases, the NMSE of the proposed method also decreases, as anticipated. Although, no such trend could be verified for the other methods.

The NMSE between the true and estimated frequency for an abrupt change of frequency at $t = 5$ s ($n = 1000$) is shown in Fig. 2.9. In this case, the NMSE is evaluated and plotted for each time instance with 1000 MC simulations. It is observed that the recovery time for the proposed method is less than the other

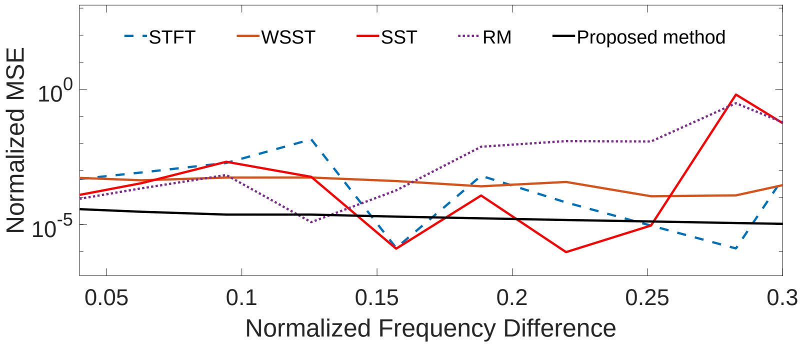

Figure 2.8: NMSE versus variation of frequency difference with 1000 Monte-Carlo simulation (SNR = 60 dB).

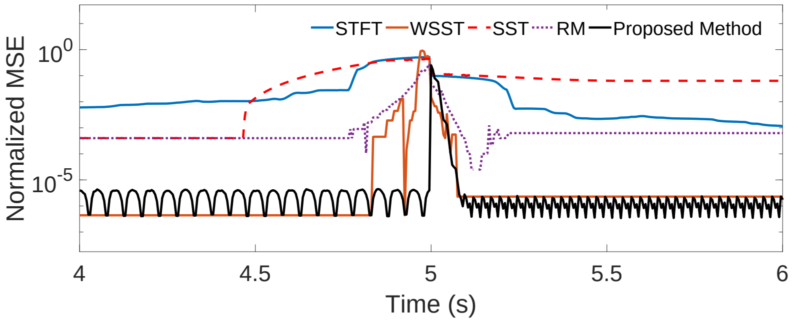

Figure 2.9: Frequency estimate with the proposed method with an abrupt change at 5 seconds for two components. SNR = 60 dB.

methods. Also, the NMSE of the proposed method decreases after the abrupt change. A sudden change in frequency resets the Kalman gain. The Kalman gain settling to lower values results in a lower correction. Once reset, the higher penalty has led to a further drop in the NMSE. It is observed that the proposed method has the lowest recovery time during an abrupt change in terms of the error, and the overall NMSE is also lower than the other methods. The temporal localization of the proposed method method under abrupt change is best compared to the others as observed in Fig. 2.9.

We can summarize that the proposed method has superior error performance for variable chirp-rate, resolution, and abrupt changes in frequency. The performance under high-SNR is also better than the state-of-the-art. However, online estimation of the noise parameters can aid in improving the low-SNR error performance. We use three examples to demonstrate the use of the method under unknown noise variances, as described in the subsequent sub-section.

2.4.3 Frequency Estimation of Real-world Examples

Three practical test cases are used to demonstrate the use of the proposed method. The first example is the echolocation problem, where the ultrasonic sound emitted by a big brown bat (Eptesicus fuscus) [143, 144] is analyzed. The short-duration signal is considered a multicomponent cubic-phase signal acquired with a sampling interval of 7 μs. The analytic signal is derived from the real signal using the Hilbert transform and is modeled by three components ($p = 3$). The frequency information obtained from the signal is shown in Fig. 2.10. For comparison, TF-distribution using WSST has been plotted in the same figure. When compared to WSST in Fig. 2.10, it is observed that the proposed method has successfully detected and estimated all three components with certainty. Whereas WSST has estimated only two components. Besides, the proposed method can track time-varying frequencies through the TVAR model parameters. However, in WSST, no such assumptions are made, and the frequency estimation is solely based on the segment of data used.

The second test case is taken to analyze gravitational waves originating due to a distant binary black hole merger. The signal from the laser interferometer gravitational-wave observatory (LIGO) detector at Hanford, Washington, is used to analyze the GW150914 event [145]. In this case, the original signal has been decimated by a factor of eight before using the IF estimators. A real mono-component model with two parameters is used for the proposed method. The observation of gravitational waves consists of three phases [146]. Gravitational

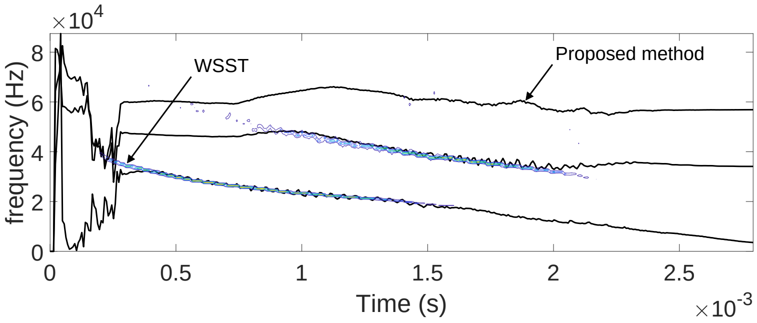

Figure 2.10: Time-frequency analysis of the echolocation pulse emitted by a big brown bat.

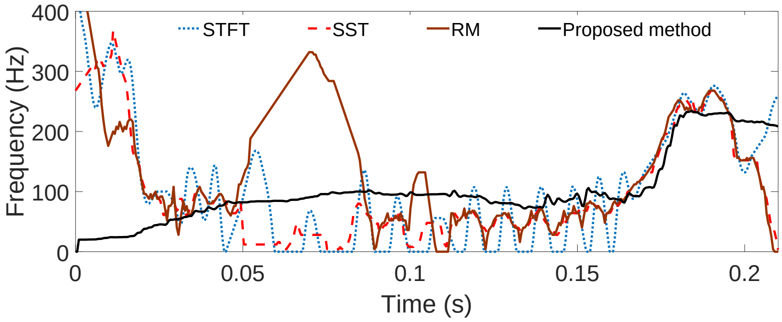

Figure 2.11: Frequency estimation for the binary black hole collision event GW150914 observed at Hanford, Washington (H1).

waves in the initial stage are emitted due to the gradual loss of orbital energy between two spinning black holes. This phase is known as the inspiral. During the inspiral-phase, the frequency is almost chirp-like. This information is best relayed by the proposed method. The other methods compared here exudes an oscillatory behavior in the frequency, as seen in Fig. 10. Eventually, during the merger-phase, the orbits shrink, and the black holes collide with speeds close to the speed of light, resulting in a Kerr black hole. During the merger, due to an increased acceleration between the colliding black holes, space-time fabric is distorted sharply. Theoretically, this results in a sharp change in the IF. A similar observation can be seen in Fig. 2.11 after 0.15 s.

A third case-study estimates the supply frequency of a variable frequency driven three-phase squirrel cage induction motor. This experiment finds the performance of the proposed method under abrupt changes. The VFD accelerated the motor from 0 Hz to 50 Hz in a span of 0.2 s. The 0.2 s limit was reached due to the physical and electrical constraints of the VFD for its safe operation. A single-phase stator current was used for this demonstration. The details of the experimental setup are presented in Section 3.5. A sampling frequency of 20 ksamples/s is used, and the data is analyzed in MATLAB. The VFD requiring a settling-time to stabilize into the final frequency is evident from the jittery time samples after 6 s, as shown in the bottom of Fig. 2.12. The 0.2 s transition band and the non-linear dynamics of the VFD are best captured with the proposed method, as is evident from the top image of Fig. 2.12. The inset figure shows the temporal resolution of the proposed method around 5.7 s using a log-scale. STFT, SST, and RM have also estimated the transition of the IF. However, an initial bias is observed in the estimate of SST and STFT when the signal is not present. Minor values in the region before six seconds and presence of noise in the input signal have resulted a bias in the ridge detection algorithm for SST and STFT.

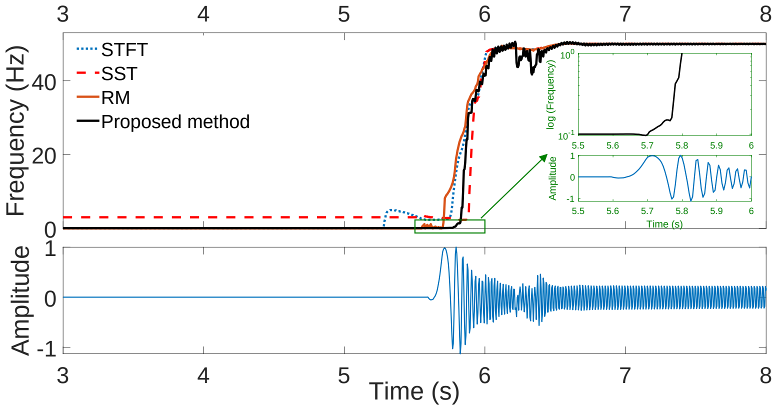

Figure 2.12: Estimating abrupt change in fundamental supply frequency using stator current of a squirrel cage induction motor. The temporal resolution during the initial stages of the abrupt change is depicted in the inset in log-scale.

2.5 Conclusions

This chapter has derived the analytic form of a linearized observation model and used a constrained Kalman filter for direct estimation of multiple time-varying frequencies. The method developed is sequential and gives an estimate of all the components of a multi-component signal simultaneously. We have replaced the dynamic linearization process using structured matrices in analytic closed-form for better accuracy. We have formed the matrices by using the coefficients of a polynomial with modified roots. Modern Eigen-based methods can accurately determine the coefficients of large polynomials [147]. From the simulation results, we can conclude that the estimator is suitable for estimating time-varying closely spaced frequency components or components having sharp changes in the frequency. The recovery time in case of the abrupt transition is better than other state-of-the-art methods. We have also observed that the technique outperforms other methods while estimating the frequency with a higher chirp-rate. The performance of the proposed method under high-SNR is proficient. However, its performance in low-SNR condition needs improvement. As a future research direction, we have to estimate the state and observation noise parameters in each time instance, when the present state is unknown for better model fitting and improved low-SNR performance.

Furthermore, use of time-varying ARMA model for low-SNR IF estimation shall be investigated. Also, the use of higher-order Gauss-Markov processes for state propagation can help in defining complex physical processes. We have taken three real-world examples to demonstrate the applicability and superiority of the proposed method under unknown SNR levels. Our approach has the advantage of using a model in addition to the data for better performance. Incorporating an accurate model in the case of the binary black hole merger can give better insight into the process that has taken place a long time ago.

CHAPTER 3

Rayleigh Quotient Spectrum for Online Detection of Partial Broken Bar in Induction Motors

In this chapter, a fast and accurate spectral estimator based on the theory of Rayleigh quotient is proposed. The Rayleigh quotient spectral (RQS) estimator can precisely determine the relative amplitude of fault side-bands and has low complexity compared to available high-resolution subspace-based spectral estimators. Detection of low-amplitude fault components has been further improved by removing the single high-amplitude fundamental frequency using an extended-Kalman-based signal conditioner. The slip of the motor is estimated from only a single phase stator current for accurate localization of the fault component. The evaluation of threshold and fault diagnosis are carried out under different load and fault severity conditions using empirical cumulative distribution function. The complete fault detection algorithm has been used for detecting partial broken rotor bar (BRB) of an inverter-fed squirrel cage induction motor under light load conditions. This system with minor modifications can detect any fault that affects the stator current.

3.1 Contribution of the Chapter

The major contributions of this chapter can be enumerated by (a) the development of a novel spectral estimator that can

1. estimate the location of fault frequency components with very high accuracy in a noisy environment and has lower computational complexity than MUSIC,
2. estimate the magnitude of fault frequencies accurately, unlike subspace-based methods like MUSIC and ESPRIT,
3. avoid spurious peaks as it do not require any information on model-order, thus, decreasing the chance of false alarms and missed detections,

(b) An elegant fault detection algorithm is developed using the novel spectral estimator having the following attributes:

1. can detect a single BRB fault with different levels of damage under low-slip. The lowest slip for the medium-sized motor to detect a partially broken bar is 0.2% under 1.9% of the rated load,
2. a novel EKF-based signal conditioner can estimate and remove the fundamental supply frequency of the input. This conditioning has improved the detectability of closely spaced fault frequencies due to partial BRB under low slip. Moreover, being a time-domain based sequential technique, it can also be used for non-stationary applications.

Outline: The chapter is structured as follows: Section 3.2 describes the proposed spectral estimator and its statistical evaluation, followed by a discussion on the statistical resolution of the method in section 3.3. Section 3.4 offers the fault detection scheme and a method for single dominant component suppression and slip estimation followed by fault detection results in section 3.6. Section 3.7 summarizes and concludes the chapter.

3.2 The Proposed Spectral Estimator

The signal model of (1.13) with time-invariant frequency is given as

$$x(n) = \sum_{i=1}^{q} |A_i| \, e^{j(n\omega_i + \phi_i)} + v(n). \tag{3.1}$$

The autocorrelation matrix ($\boldsymbol{R}_x$) of size L, is constructed from the data matrix ($\boldsymbol{X}$) of same size [120] without any interleaved samples, as given by (3.2).

$$\boldsymbol{X} = \begin{bmatrix} x(0) & \cdots & x(L-1) \\ . & \cdots & . \\ x(L-1) & \cdots & x(2L-2) \end{bmatrix} \tag{3.2}$$

Assuming the process to be ergodic, $\boldsymbol{R}_x$ can be estimated by

$$\hat{\boldsymbol{R}}_x = \frac{1}{L}\{\boldsymbol{X}^H \cdot \boldsymbol{X}\} \tag{3.3}$$

3.2.1 Theoretical Background of the Spectral Estimator

For a symmetric matrix $\boldsymbol{A}$, with known eigenvector $\boldsymbol{v}$, corresponding eigenvalue (λ) can be approximated by using the theory of Rayleigh quotients ([148], Pg.

301-304) as

$$\hat{\lambda} = \frac{\boldsymbol{v}^H \boldsymbol{A} \boldsymbol{v}}{\boldsymbol{v}^H \boldsymbol{v}} \tag{3.4}$$

For the present problem, $\hat{\boldsymbol{R}}_x$ is symmetric and its eigenvectors are related to the independent frequency components present in the signal. The vector $\boldsymbol{w}(\omega)$ of (3.5) will become an eigenvector of $\hat{\boldsymbol{R}}_x$ if a sinusoid of frequency ω is present ([149], Pg. 452) in the signal. Sweeping ω between 0 to 2π will give a peak of $\hat{h}(\omega)$ (3.6) when ω matches the frequency of a sinusoid present in the signal. The peak $\hat{h}(\omega)$ is the eigenvalue corresponding to the eigenvector $\boldsymbol{w}(\omega)$ and is related to the amplitude of the sinusoid present in the signal.

$$\boldsymbol{w}(\omega) = \left[\begin{array}{cccc} e^{j\omega \cdot 0} & e^{j\omega} & \cdots & e^{j\omega \cdot (L-1)} \end{array} \right]^H \tag{3.5}$$

and $\boldsymbol{w}(\omega)^H \boldsymbol{w}(\omega) = L$, and $\omega \in [0, 2\pi]$.

$$\hat{h}(\omega) = \frac{\boldsymbol{w}(\omega)^H \hat{\boldsymbol{R}}_x \boldsymbol{w}(\omega)}{\boldsymbol{w}(\omega)^H \boldsymbol{w}(\omega)} \tag{3.6}$$

3.2.2 Amplitude Estimation

Putting the estimate of (3.3) in (3.6) gives

$$\hat{h}(\omega) = \frac{1}{L^2} \left[\left(\boldsymbol{X} \boldsymbol{w}\left(\omega\right) \right)^H \cdot \left(\boldsymbol{X} \boldsymbol{w}\left(\omega\right) \right) \right]. \tag{3.7}$$

The product $\boldsymbol{X}\boldsymbol{w}\left(\omega\right)$ of (3.7) can be found as

$$\begin{aligned} \boldsymbol{X}\boldsymbol{w}(\omega) &= \left[\begin{array}{ccc} x(0) & \cdots & x(L-1) \\ . & \cdots & . \\ x(L-1) & \cdots & x(2L-2) \end{array} \right] \left[\begin{array}{c} e^{-j\omega \cdot 0} \\ \vdots \\ e^{-j\omega (L-1)} \end{array} \right] \\ &= \left[\begin{array}{ccc} \sum_{i=0}^{L-1} x(i) e^{-j\omega i} & \cdots & \sum_{i=0}^{L-1} x(i+L-1) e^{-j\omega i} \end{array} \right]^T \end{aligned} \tag{3.8}$$

Now, we define that

$$X_q(\omega) = \sum_{r=0}^{L-1} x(r+q)e^{-j\omega r}, \tag{3.9}$$

and using this in (3.8), it is obtained that

$$\boldsymbol{X}\boldsymbol{w}(\omega) = \begin{bmatrix} X_0(\omega) & \cdots & X_{L-1}(\omega) \end{bmatrix}^T \tag{3.10}$$

putting the value of (3.10) in (3.7) gives

$$\hat{h}(\omega) = \frac{1}{L^2}\sum_{i=0}^{L-1} |X_i(\omega)|^2 \tag{3.11}$$

Now taking the square of the absolute value on both sides in (3.9) and putting it in (3.11) gives

$$\hat{h}(\omega) = \frac{1}{L^2}\sum_{i=0}^{L-1} \left|\sum_{v=0}^{L-1} x(v+i)e^{-j\omega v}\right|^2 \tag{3.12}$$

In the next section, a simplified way to implement this method in matrix form will be discussed. Now a single sinusoid at ω_k with spectral peak magnitude $\hat{h}(\omega_k)$ without any noise can be modeled using (3.1) as

$$x[n] = A_k e^{j(\omega_k n + \phi_k)} \tag{3.13}$$

Putting $x[n]$ in (3.12) gives

$$\begin{aligned}
\hat{h}(\omega_k) &= \tfrac{1}{L^2}\sum_{i=0}^{L-1}\left|\sum_{v=0}^{L-1} A_k e^{j\omega_k(v+i)} e^{j\phi_k} e^{-j\omega_k v}\right|^2 \\
&= \tfrac{1}{L^2}\sum_{i=0}^{L-1}\left|A_k e^{j\omega_k i} e^{j\phi_k}\sum_{v=0}^{L-1} 1\right|^2 \\
&= \tfrac{A_k^2 L^2}{L^2}\sum_{i=0}^{L-1} 1 \\
&= LA_k^2
\end{aligned} \tag{3.14}$$

From (3.14), the amplitude a_k is estimated by $\hat{A}_k$ as

$$\hat{A}_k = \sqrt{\hat{h}(\omega_k)\Big/L} \tag{3.15}$$

Fig. 3.1 shows the amplitude estimation efficacy of the RQS estimator in estimating the amplitude of closely spaced sinusoids. Two sinusoids at 49.8 Hz and 50 Hz with equal amplitude have been used as input for this experiment. Different SNR has been achieved by varying the sinusoidal amplitude and keeping the noise variance constant. The peak has been detected from the spectrum, and its amplitude is evaluated by (3.15). It is observed that the amplitude estimation error is very low, even in low SNR. Hence, the spectral estimator can be used to quantify the severity of faults accurately under light loads when the fault components are weak and close to the fundamental.

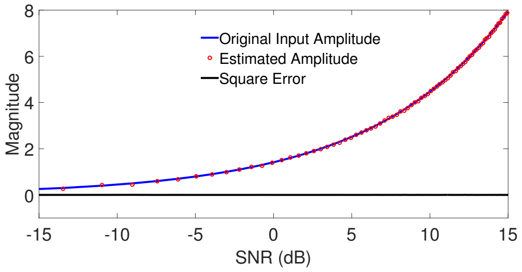

Figure 3.1: Estimation of amplitude, $L = 2000$, $F_s = 200Hz$.

The performance of the RQS estimator is evaluated in terms of its execution time, frequency estimation accuracy, and resolvability of closely spaced sinusoids. A comparison between the the proposed method, MUSIC, and DFT for estimating the spectrum is shown in Fig. 3.2. The RQS estimator doesn't require windowing to avoid spectral leakage. Whereas DFT without windowing gives rise to false peaks, as shown in Fig. 3.2a. This can be disadvantageous for motor fault diagnosis. A Chebyshev window [124] was used for DFT to reduce the false peaks as in Fig. 3.2b. Also, it was found that the presence of another sinusoid hampers the frequency estimates of the DFT, as shown in Fig. 3.3a. For this simulation, two sinusoids (50Hz, 53 Hz) with unity amplitude were used. The frequency estimate for a sinusoid in the presence of other sinusoids using DFT can be improved by using a window over the input samples, as shown in Fig. 3.3b. However, on the application of a window, the location error estimates of DFT is found to be inferior compared to the proposed method. The performance of the proposed method against MUSIC is identical.

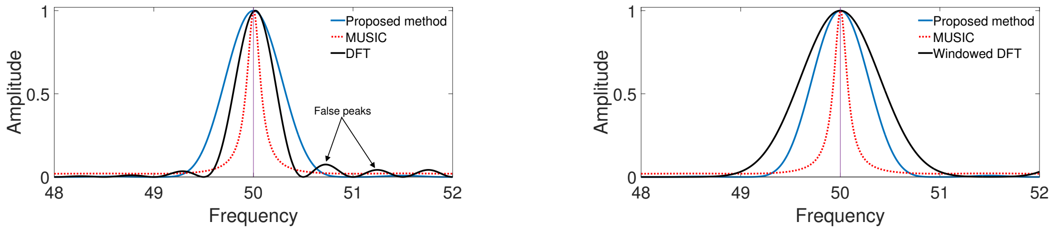

(a) Spectrum without windowing for DFT.

(b) Spectrum with windowed input data for DFT.

Figure 3.2: Comparison of spectral estimators for possible spectral leakages resulting in false peaks. The frequency $f_1 = 50Hz$ was used for this simulation, $N = 399$.

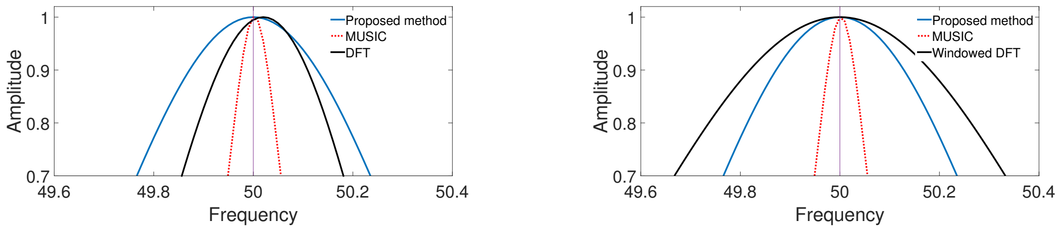

(a) Spectrum without windowing for DFT.

(b) Spectrum with windowed input data for DFT.

Figure 3.3: Comparison of spectral estimators for peak frequency estimation in the presence of another sinusoid. The frequency $f_1 = 50$ Hz and $f_2 = 53$ Hz was used for this simulation, $N = 399$.

The mean execution time was evaluated over 1000 trials for each N for the proposed spectral estimator, MUSIC, and DFT. It is evident from Fig. 3.4 that the proposed spectral estimator has a lower time complexity than MUSIC but is slightly slower than DFT.

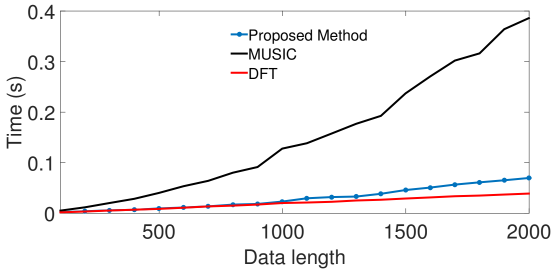

Figure 3.4: Mean execution time for DFT, MUSIC, and the proposed method over 1000 trials for each data length (N).

The accuracy of peak-frequency estimation and the robustness of the proposed method has been compared with DFT and MUSIC. In Fig. 3.5a, the MSE between the input sinusoidal frequency and the location of the peak obtained from the respective spectral estimator is evaluated by 100 trials for each N. It is inferred that MUSIC and the proposed spectral estimator have slightly higher accuracy for similar data length when compared to DFT with windowed data. In Fig. 3.5b, MSE is evaluated with different SNR levels for 100 trials each. It is found that the performance of the proposed spectral estimator in a noisy environment is quite robust and is similar to that of MUSIC and is better than DFT with windowed data. A single sinusoid of 50.1111 Hz and unity amplitude has been used for both experiments. $F_s = 200$ Hz was used.

The proposed method is most suitable for fault detection as it is fast and can estimate the fault frequency and its amplitude accurately without any information about the number of sinusoids. The simulations were conducted with the offline system described in Appendix A.4. The Cramer-Rao lower bound (CRLB) for single-frequency estimation (derivation in Appendix C) is given as

$$\mathrm{var}(f) \geq \frac{3\sigma_v^2 F_s^2}{\pi^2 A_1^2 N(N-1)(2N-1)} \tag{3.16}$$

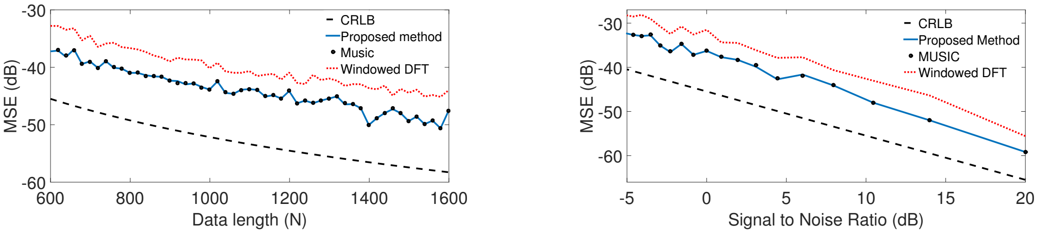

(a) Frequency estimation error for different values of N.

(b) Frequency estimation error for different SNR levels, $N = 599$.

Figure 3.5: Evaluation of frequency estimate error for different data length and SNR levels.

3.3 Optimal Choice of Data Length with Probability of Resolution

For accurately resolving two closely spaced sinusoids, with minimum execution time, an optimal length of data (N) needs to be set for any spectral estimator [150]. The optimum value of N for the proposed spectral estimator is determined statistically with probability of resolution. The decision statistic, γ as in (3.17) decides whether two known frequency components (f_1 and f_2) are resolved with a particular estimator [151].

$$\gamma(f_1, f_2) \triangleq h(f_m) - \frac{1}{2}\{h(f_1) + h(f_2)\} < 0, \tag{3.17}$$

where f_m is the mean of f_1 and f_2, and $h(f_i)$ is the magnitude of the ${f_i}^{\text{th}}$ component obtained from the spectrum. The probability of resolution for various data lengths with three levels of SNR is shown in Fig. 3.6a. Two sinusoids of unity amplitude and a frequency difference of 1 Hz are considered. For each N, 100 trials have been conducted to find whether the sinusoids are resolved. It is evident from the figure that $N = 400$ is sufficient to resolve two sinusoids of equal magnitude having a frequency difference of 1 Hz and SNR > 0 dB with 100% probability. The required minimum value of N decreases with decreasing noise.

From Fig. 3.6b, it is observed that the classical periodogram without windowing has a higher resolution than the proposed method. The high-resolution is mainly because the proposed spectral estimation action is based on an average spectrum obtained from each column of the data matrix. In contrast, the classical periodogram uses a single vector of data-length that is approximately twice that of each column of the proposed method's data-matrix. The use of windowing is necessary for fault detection to avoid spectral leakage and false alarms while using a classical periodogram. However, using windowed data, the classical periodogram has a lower resolution shown in Fig. 3.6c compared to the proposed method. In this thesis, the value of L is fixed at 2000 ($N = 3999$) to detect weak faults under low-slip.

3.4 The Proposed Fault Detection Scheme

A schematic block diagram of the proposed fault detector is shown in Fig. 3.7. The signal conditioner estimates and removes the fundamental frequency component from the input. The spectrum of the conditioned signal is used for finding the slip and the fault specific frequency components. The slip information is used to construct the fault search band. Fault specific frequencies and their peak magnitudes are evaluated in the search band. The amplitude estimator uses (3.15) to determines the peak amplitude and sends them to the decision block for threshold comparisons. The major subsystems other than the spectral estimator involved in the fault detection scheme are discussed in the following section.

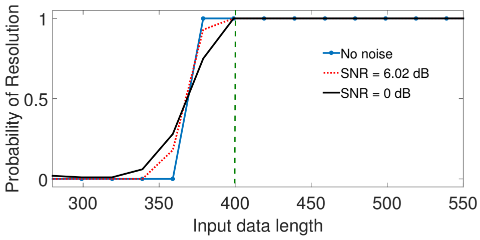

(a) Probability of resolution for the proposed method

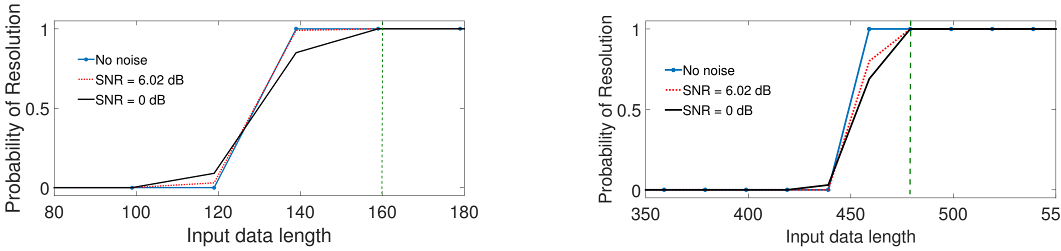

(b) Probability of resolution for classical periodogram without windowing

(c) Probability of resolution for classical periodogram with windowing

Figure 3.6: Probability of resolution versus data length (N) for different levels of SNR ($F_s = 200$ Hz).

3.4.1 Estimation of Fundamental Frequency and Signal Conditioning with EKF

The pioneering work of Routray et al. [44] can efficiently estimate and track the fundamental frequency of single-phase current using EKF. In this chapter, the algorithm was modified to estimate the fundamental signal $y_o(k)$ in addition to the fundamental frequency $f_o(k)$. The estimated fundamental signal is then subtracted from the measured stator current $y(k)$ to generate the conditioned signal $\varepsilon(k)$, which is void of the supply component. Fig. 3.8 illustrates the method used in this chapter. The state vector is given by (3.18).

$$\hat{x}_s(k) = [2\cos(\omega) \quad \hat{y}(k-1) \quad \hat{y}(k-2)]^T \tag{3.18}$$

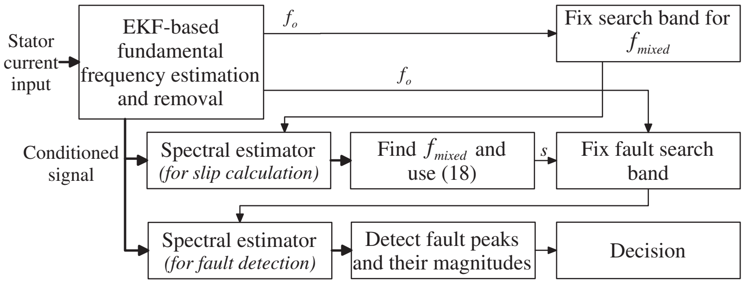

Figure 3.7: The complete SCIM fault detection scheme.

Detailed implementation and analysis of EKF can be found in [44].

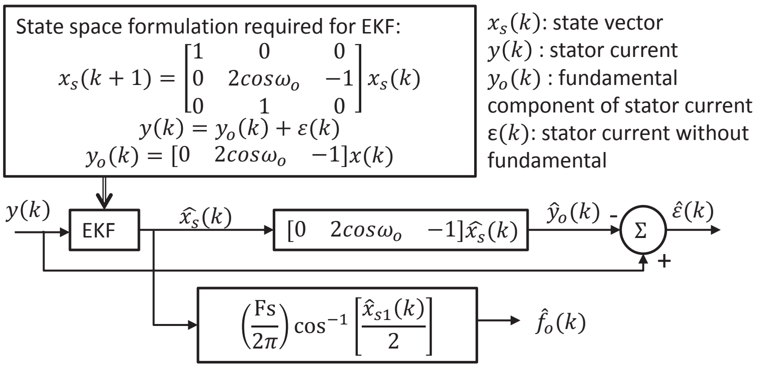

Figure 3.8: The signal conditioning and fundamental frequency estimator. $\hat{x}_{s1}(k)$ is the first element of the estimated state vector.

This method, though simple, is very useful in eliminating the fundamental component. The spectrum of the stator current without input signal conditioning is shown in Fig. 3.9a. It is observed in Fig. 3.9b that, with EKF signal conditioning, the amplitude of the fundamental component is effectively attenuated. Consequently, the spectral leakage due to the fundamental is reduced, and the detectability of low amplitude side-bands close to the fundamental frequency is enhanced. The spectra were obtained using the proposed spectral estimator.

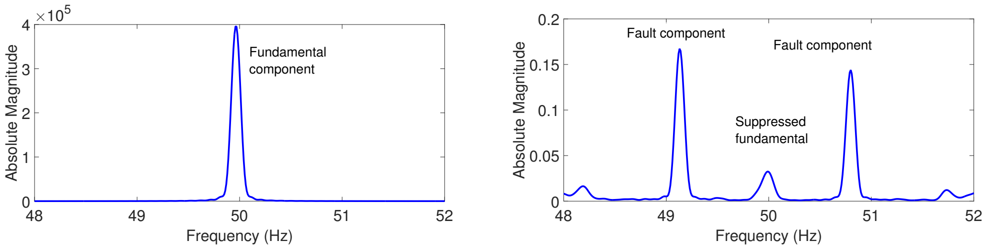

(a) Unconditioned stator current with undetectable fault components

(b) Conditioned stator current with suppressed fundamental and clearly visible fault components

Figure 3.9: Effect of signal conditioning with EKF (the motor running with 33% load and 0.9% slip under single BRB fault)

3.4.2 Estimation of Slip

Fault frequency components related to BRB are motor slip dependent. The value of slip is used to form the fault frequency search bands for the spectral estimator. The motor slip can be measured using a speed sensor or can be estimated using observer-based soft-sensing techniques [152], and slot-harmonic-based [153] methods. The observer methods require the acquisition of all the phase voltages and currents. It also requires accurate estimate of certain motor parameters that are difficult to determine and may change with time. The slot harmonic based method requires a high sampling rate, which has its own disadvantage. Most SCIMs carry an inherent low-frequency mixed eccentricity (1.11) component due to machine saturation [153]. The SCIMs used for this work also exhibited the mixed eccentricity component which is reproduced below for convenience

$$f_{mi} = \left| \frac{1 \pm k(1-s)}{p} \right| f_o$$

This component was present even when all precautions were taken during the fault incorporation and motor assembling process. Using the lower component of (1.11), and putting $k = 1$ (the principal frequency component) and $p = 2$ (number of pole-pairs for experimental motor under test), the slip is obtained as

$$s = \frac{2f_{mi} - f_o}{f_o} \tag{3.19}$$

The proposed spectral estimator (Section 3.2) is used for finding f_{mi} in the frequency band of $0.5f_o$ to $0.6f_o$, with $F_s = 200$ samples/s. This band is obtained by evaluating f_{mi} from (3.19) with the slip ranging from 0% to 20% for the four-pole machine. The highest peak obtained in this band is the mixed eccentricity component given by f_{mi}. The mean of the relative square error for the speed estimator was found to be 1.908E-07. The error was evaluated from full BRB fault dataset (refer Table 3.1), which consisted of 72 datasets for different loads. The error was calculated from the measurement obtained from the proximity speed sensor (see Section 3.5).

3.5 The Experimental Setup

A schematic diagram of the experimental setup is illustrated in Fig. 3.10. The experimental setup consists of a 22 kW, four-pole, and three-phase SCIM manufactured by ABB. Power to the motor was supplied with VFD from ABB (model: ACS550-U1-045A-4). We have used multiple sensors to record different signals of the motor, as shown in Fig. 3.10. Complete specifications of the experimental setup are provided in Appendix A.1. A three-phase tacho-generator was coupled to a generator for speed estimation. A photograph of the motor-generator setup is shown in Fig. 3.11. Variable loading was achieved through rheostatic loads, with a 24-kW separately excited DC generator coupled to the motor shown in Fig. 3.11.

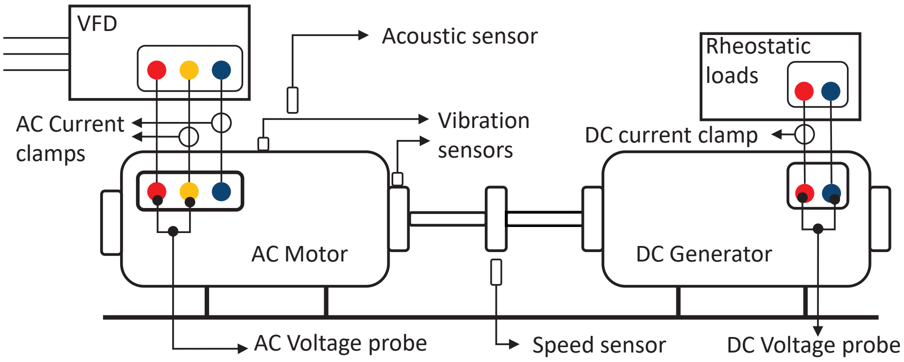

Figure 3.10: The schematic diagram of the experimental setup

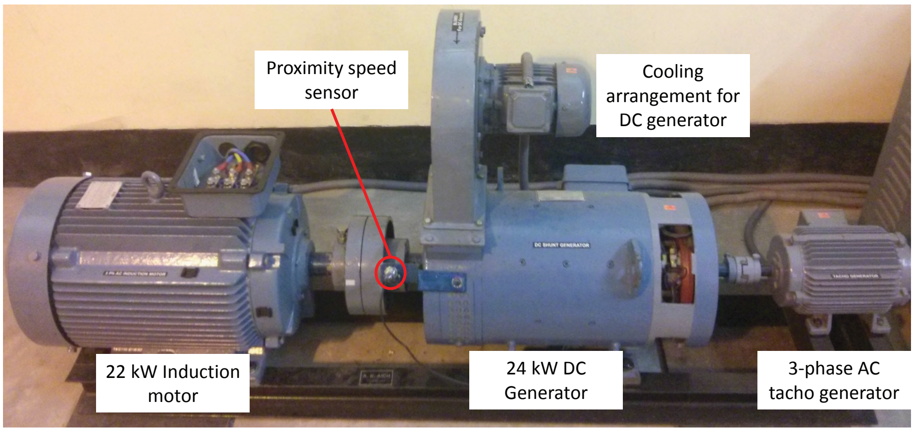

Figure 3.11: A photograph of the motor-generator experimental setup

3.5.1 Signal Acquisition

A 16-channel Yokogawa 850v data acquisition system (see Appendix A.5 for details) simultaneously recorded multiple signals with a sampling frequency of 20 kHz. The inbuilt analog low-pass filter of the data acquisition system was configured with a 4-kHz cutoff to avoid aliasing. For steady-state analysis, the motor was run for three minutes before every acquisition. For the SCIM, we have recorded two phases of the stator current and three phase-voltages. For acquiring the stator current, we have used Fluke i1000 clamp-type current transducer. The phase voltages were tapped using Fluke voltage probes. We have illustrated only one-

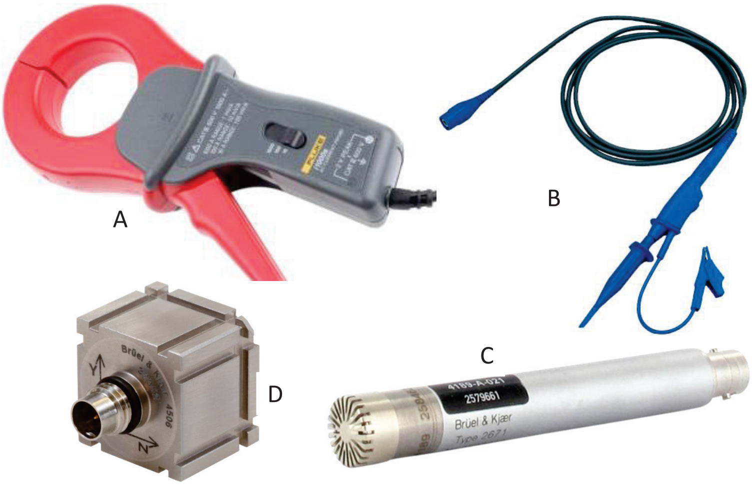

Figure 3.12: The different sensors used for signal acquisition. Clockwise from top (A) current sensor, (B) voltage sensor, (C) acoustic sensor, (D) vibration sensor.

phase voltage acquisition in Fig. 3.10 for clarity. We have recorded the vibration of the SCIM using two tri-axial vibration sensors (Brüel & Kjær, model: 4506). One sensor was mounted on the driving end, while the other was mounted in the middle of the motor. Data from the radially oriented axis of the driving-end sensor is only used in this thesis for uniformity. The rotational speed of the motor was measured using a proximity-based sensor mounted atop the coupling, as shown in Fig. 3.11. We have also recorded the acoustic emission using (Brüel & Kjær, model: 2579661) unidirectional microphone. The photograph of the sensors used in the experimental setup is shown in Fig. 3.12. The offline analysis was carried out with MATLAB. The specification of the computational platform is given in Appendix A.4. Other than the SCIM signatures, we have recorded load current and armature voltage of the DC generator and two phase-voltage of the three-phase tacho-generator.

Table 3.1: Description of different BRB faults used for the experiments

Fault	healthy BRB	partial BRB	half BRB	full BRB
Drill Depth	0 mm	4 mm	16 mm	34 mm

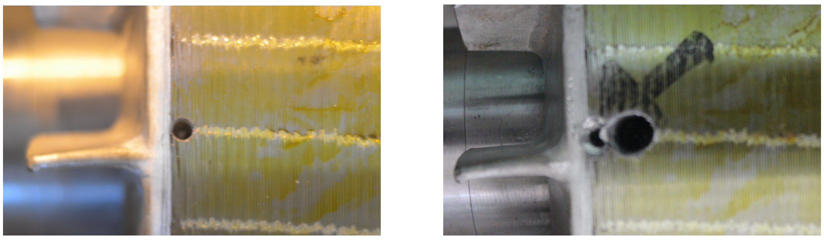

(a) Half BRB fault (b) Full BRB fault

Figure 3.13: Photograph of different levels of BRB fault

3.5.2 Incorporation of Faults

For simulating BRB, a single rotor was damaged at different depth-levels, as given in Table 3.1 and shown in Fig. 3.13 for the experiment. For damaging the bearing, single 2-mm holes, as shown in Fig. 3.14, were machined into the outer raceway, the inner raceway, and the rolling element of the driving-end bearing using spark electric discharge machining. Figure 3.15 shows the machining process and one of the copper electrodes that was used for machining the holes in different parts of the bearing. Additionally, we have used the CWRU dataset [15] for validating the vibration-based algorithm for bearing fault detection. The specification of the bearing used in the CWRU dataset is given in Appendix A.3. Characteristic primary fault frequencies in terms of f_r for both the tested bearings are given in Table 3.2.

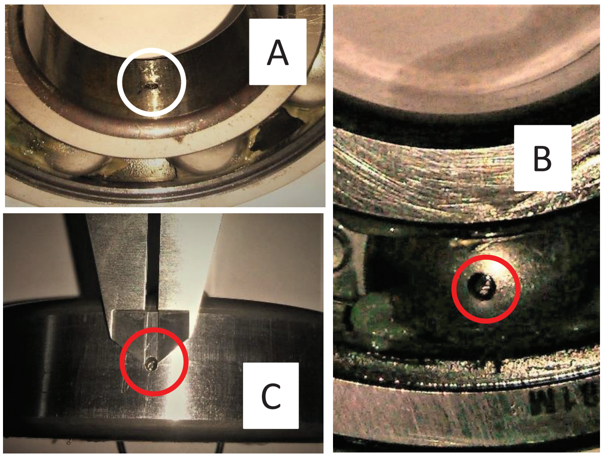

Figure 3.14: Different kind of bearing faults (A) Inner raceway fault, (B) Rolling element and cage fault, (C) Outer race fault.

Figure 3.15: Electrical discharge machining underway for creating outer raceway fault and one of the sample copper electrodes used.

Table 3.2: Bearing vibration fault frequencies (multiple of f_r in Hz)

Bearing	Outer	Inner	Rolling	Cage
SKF 6310-2ZR (Lab)	3.0476	4.9524	3.9619	0.3810
SKF 6205-2RS (CWRU)	3.5848	5.4152	4.7134	0.3938

3.6 Experimental Results and Discussion

Experiments for BRB and its analyses can be classified into two categories. With the first set of analysis, detectability with partial damage to a single bar with different slips is illustrated. For these experiments, frequency spectra with the proposed method and MUSIC are compared. For uniform plots, each spectrum has been normalized by its fundamental peak value obtained after EKF-conditioning.

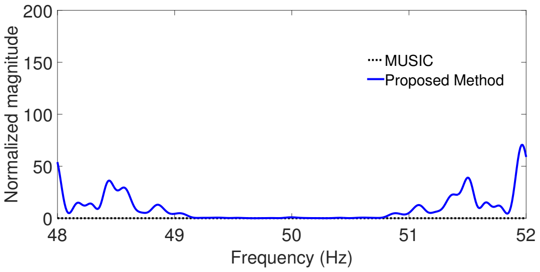

Figure 3.16: Normalized stator current spectrum of a healthy motor with 1.9% load and 0.2% slip using MUSIC and the proposed spectral estimator.

In Fig. 3.16, the experiment results with 1.9% load and a 0.2% slip for healthy BRB are shown. In Fig. 3.17, results with 1.9% load and 0.2% slip for partial BRB fault is presented. In this case, the upper and lower side-bands at $(1 \pm 2s)f_o$ appears in the spectrum, and the difference between healthy and faulty condition is quite comprehensive.

Fig. 3.18 illustrates the partial BRB fault with a 0.33% slip. Spectral signature with increased fault severity in the form of the half BRB is shown in Fig. 3.19. The motor has been operating with 0.33% slip on the application of 9% load. It is observed that MUSIC doesn't give rise to fault peaks, which may be due to improper estimation of the number of sinusoids. The effectiveness of the method for the detection of BRB fault with high load is demonstrated in Fig. 3.20. The peaks obtained by MUSIC don't provide any information about the fault

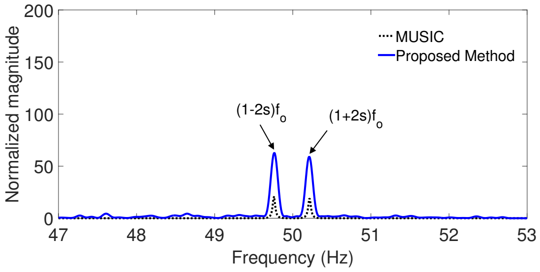

Figure 3.17: Normalized stator current spectrum of the motor with partial BRB running with 1.9% load and 0.2% slip using MUSIC and the proposed spectral estimator.

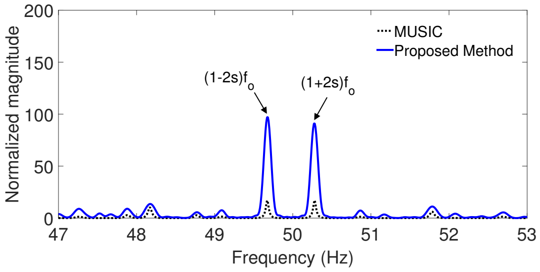

Figure 3.18: Normalized spectrum of stator current with partial BRB running with 13% load and 0.46% slip.

severity. It is also to be noted that the location of fault frequencies obtained by both the spectral estimators are equivalent. This experiment demonstrates the effectiveness and reliability of the proposed spectral estimator compared with MUSIC for detecting weak BRB faults.

The second set of analysis deals with different BRB fault levels on the magnitude spectra, with similar loading in all the cases. The spectrum for this set has also been normalized with the magnitude of the attenuated fundamental component. It is observed in Fig. 3.21 that, with increasing BRB severity, the magnitude of the fault component also increases. The fault frequency peaks for different cases don't exactly match due to slight variations in each case's supply frequency. For partial and half BRB cases, fault components with $k = 4$, and $k = 5$ in (1.8) are exceptionally prominent for the 50 Hz supply. Fig. 3.22 shows the spectrum of

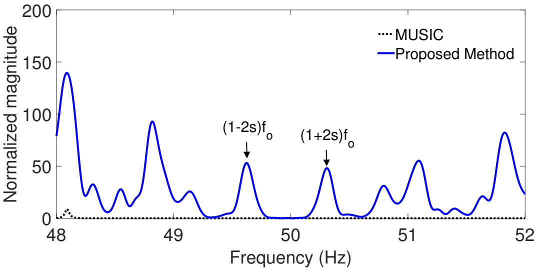

Figure 3.19: Motor with half BRB with 9% load and 0.33% slip.

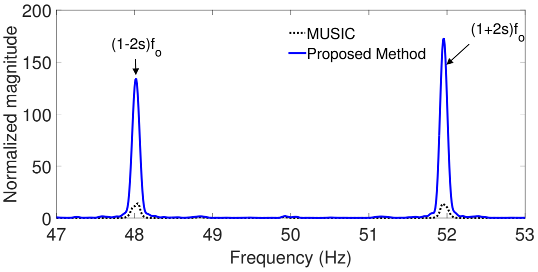

Figure 3.20: Motor with full BRB operating under a high load of 71% and 2.06% slip.

the stator current obtained by the proposed spectral estimator for 40 Hz supply frequency and 0.33% slip for all the cases. Fig. 3.23 shows the spectrum with 30 Hz supply frequency and 0.45% slip for all the fault cases. With 40 Hz and 30 Hz supply, the fault components with $k = 1$ are most prominent, and the peak magnitude increase with increasing fault severity.

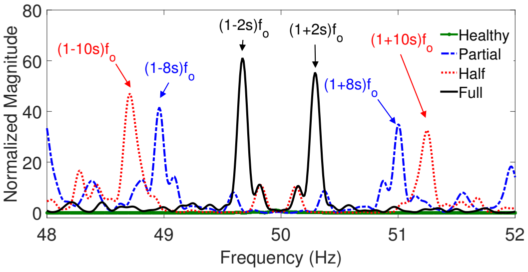

Figure 3.21: Spectrum of stator current with different BRB fault levels for 50 Hz supply (0.26% slip) using the proposed spectral estimator.

From the above results, it is clear that the side-band peaks normalized by the

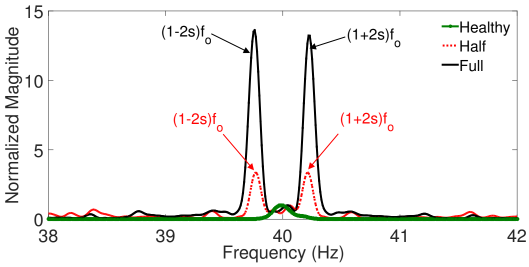

Figure 3.22: Spectrum of stator current with different BRB fault levels for 40 Hz supply (0.33% slip) using the proposed spectral estimator.

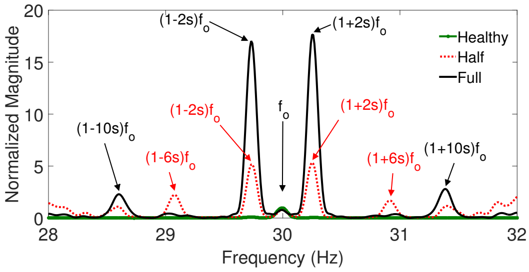

Figure 3.23: Spectrum of stator current with different BRB fault levels for 30 Hz supply (0.45% slip) using the proposed spectral estimator.

fundamental frequency magnitude can distinguish between the healthy and the faulty cases. The normalized magnitude (Y) is the ratio of the magnitude of the fault specific magnitude ($\hat{h}_{fault}$) to the magnitude of the fundamental component ($\hat{h}_{f_o}$) obtained after suppression given by

$$Y = \frac{\hat{h}_{fault}}{\hat{h}_{f_o}} \tag{3.20}$$

The dispersed nature of the peak magnitudes makes it prudent to employ a probabilistic measure to fix a threshold. Hence, the cumulative distribution function (CDF) of the normalized side-bands has been computed as plotted in Fig. 3.24. The distribution function is given by ([149], Pg. 61)

$$F_Y(\alpha) = \mathcal{P}(Y \leq \alpha) \tag{3.21}$$

Table 3.3: Statistics for BRB fault

Threshold Value	Missed Detection	False Alarm
20.30	27.38%	0.00%
17.65	23.50%	1.09%
14.16	19.35%	8.70%
10.03	13.00%	23.00%

where Y is a random variable and α is any number. In the present scenario, Y represents the normalized peak magnitude of a particular dataset (healthy/faulty) and α is the chosen threshold. An overlap between the CDF magnitudes corresponding to the faulty and the healthy cases have been observed. Therefore, an optimal threshold is found to represent the acceptable tradeoff between the missed detection and false alarm rates. Any normalized peak value above α is considered as faulty. The fraction of data on the right side of the threshold in Fig. 3.24 for the healthy CDF representing the false-alarm (FA) is given by

$$FA = 1 - \mathcal{P}(Y_{healthy} \leq \alpha), \tag{3.22}$$

while the fraction of data on the left side of the threshold for faulty CDF representing the missed detection (MD) is given by

$$MD = \mathcal{P}(Y_{faulty} \leq \alpha), \tag{3.23}$$

where $Y_{healthy}$ and Y_{faulty} are the normalized peak magnitudes of healthy and faulty data, respectively. A range of suitable threshold from Fig. 3.24, are given in Table 3.3. It is observed that a normalized side-band peak magnitude greater than 20.3 can be considered as faulty without any false alarm.

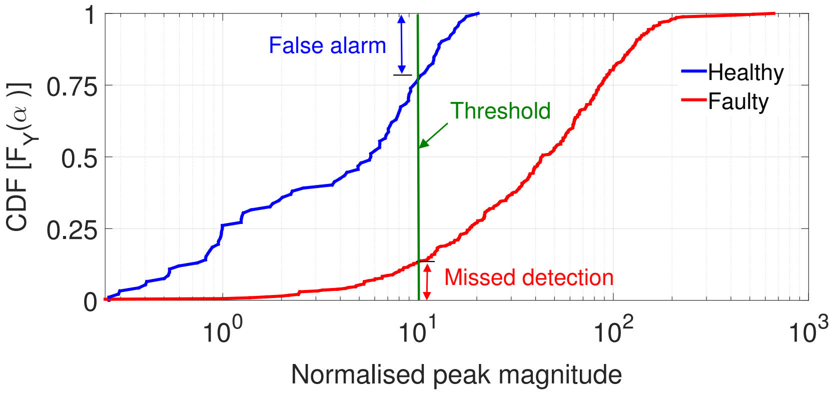

Figure 3.24: Empirical CDF of normalized peak magnitude (in log scale) for healthy and faulty cases (50 Hz data), with all the fault-motor cases augmented in a single vector.

3.7 Conclusions

This chapter presented the development of an online SCIM fault detection system based on the spectral analysis of a single-phase stator current. The theory of Rayleigh quotient was utilized for designing the proposed spectral estimator. The performance of the spectral estimator for detecting frequency components is better than DFT and is similar to that of MUSIC. Additionally, it can estimate the amplitude of the fault components and is also faster, unlike MUSIC. An EKF-based signal conditioner was used for removing single dominant component. The conditioner has enhanced the detection of partial BRB fault under ultra-low load conditions. The system is adaptive to changes in supply frequency and loads for a particular frame of data but is unsuitable for detecting defects under transient and non-stationary conditions.

The proposed fault detection system was validated by extensive experiments with different fault levels of BRB fault under various loading conditions. Empirical CDF was adopted to determine a threshold required for the assessment of the faults. Detection of low-amplitude closely-spaced sinusoids makes this method a powerful tool for detecting weak failure modes such as partial BRB in low-load applications.

CHAPTER 4

Minimum Distance-based Detection of Incipient Induction Motor Faults using Rayleigh Quotient Spectrum of Conditioned Vibration Signal

This chapter proposes a single vibration sensor-based method for detecting incipient faults in SCIMs. We consider defects in different parts of the bearing (inner raceway, outer raceway, cage train, and rolling element) and a single bar of the rotor. The vibration signal is dominated by the fundamental rotational frequency and its harmonics. The dominant components result in numerical errors while estimating the relatively indistinct fault-specific spectral features. In this chapter, we precondition the vibration signal by suppressing multiple dominant components using an extended Kalman filter-based method. The suppression of the significant components reduces the spectral leakage, exposes minute fault components, and improves the overall amplitude estimation. Subsequently, we estimate the fault frequency and amplitude using the Rayleigh-quotient-based spectral estimator outlined in Chapter 3. The thresholds for fault detection are determined from a small number of healthy data. An adaptive minimum distance-based detector is then used for hypothesis testing. The proposed test improves detection and reduces false alarms under noisy conditions. We test the complete algorithm using data from a 22-kW SCIM lab-setup (see Section 3.5) and the publicly available data from Case Western Reserve University [15].

4.1 Contribution of the Chapter

In our previous works, we have used stator current to detect a single BRB using MUSIC [95] and RQS estimator [16]. The advantages of the latter in terms of reduced-complexity, accuracy in frequency estimation, and amplitude estimation make it suitable for analyzing vibration signals. Chapter 3 uses a Kalman filter-based method to track and remove a single dominant frequency. However, for detecting multiple faults using vibration, we need to track and remove multiple dominant components. This chapter proposes a method that can identify weak-faults due to incipient anomalies in the bearings and rotor bars using single-axis vibration data. The novel contributions of this chapter can be outlined as follows.

1. The use of single-axis vibration data to identify weak faults under various loading conditions in SCIMs.

2. For conditioning the vibration signal, we improvise our recently proposed Kalman-based method (chapter 2, [93]) to track and remove multiple dominating components of rotational frequency and its harmonics. The conditioning reduces the spectral leakage and improves the detectability of incipient

faults. The proposed method can also be employed under non-stationary conditions when the dominant frequencies vary with time.

3. A minimum distance detector [137] has been constructed to detect faults and incorporate information about the inherent fault component, which can be present even when the motor is healthy. Unlike the recently used data-driven techniques, the proposed method only requires a few healthy-motor instances of data for threshold selection.

The proposed method has been tested and validated on a 22-kW SCIM laboratory setup (described in section 3.5), as well as with the publicly available CWRU drive-end, 12 kHz bearing data [15].

Outline: We have structured the chapter as follows: Section 4.2 extends the IF estimator of chapter 2 for eliminating multiple dominant components of the vibration signal. Section 4.3 proposes the minimum distance detector for considering inherent fault component magnitude. The implementation of the overall vibration-based fault detection algorithm is provided in section 4.4. The experimental results and performance comparison, and a discussion on the results, are given in section 4.5. Section 4.6 summarizes and concludes the chapter.

4.2 Preconditioning of the Vibration Signal

In chapter 2, we have tracked and estimated the instantaneous frequencies of a non-stationary signal. In this section, we modify the method to estimate the contribution of multiple dominant components in the signal and use the information to eliminate them for reducing the effect of spectral leakage. We assume that the dominating i^{th} component without the noise of (1.13) is represented by $\tilde{x}_i[n]$ as

$$\tilde{x}_i[n] = |A_i| e^{j(n\omega_i[n]+\phi_i)}. \tag{4.1}$$

We will estimate $\omega_i[n]$ and $\tilde{x}_i[n]$ for multiple dominant components for each instance of n, and then use the estimated $\tilde{x}_i[n]$ for its elimination from the input signal $x[n]$. We define $\tilde{q}$ as the number of dominating components, assumed to be a known quantity. We presume that magnitude of the dominating $\tilde{q}$ components are significantly higher than the other $(q-\tilde{q})$ components, i.e., $|A_i| \gg |A_j|$, $\forall \{(i,j) : i \in [1,\tilde{q}], j \in [\tilde{q}+1, q]\}$. With complex amplitude representation (4.1), we have $\tilde{x}_i[n] = A_i e^{jn\omega_i[n]}$ with $A_i = |A_i|\, e^{j\phi_i}$. Now, following the derivation given in chapter 2 (2.3 - 2.9) and replacing $p = \tilde{q}$, we have from (2.9)

$$x[n] = h(\boldsymbol{\theta}[n]) + v[n].$$

The conditioned signal $\hat{x}_0[n]$ is obtained by eliminating the estimated $h(\hat{\boldsymbol{\theta}}[n])$ (2.10) from the input $x[n]$ as

$$\hat{x}_0[n] = x[n] - h(\hat{\boldsymbol{\theta}}[n]). \tag{4.2}$$

We directly estimate the sinusoidal frequencies using the observation model (2.9) and then eliminate the frequency component from the input signal. The modified algorithm for the suppression of dominant frequencies is given in Algorithm 4

An example test case to compare the spectrum of the raw and conditioned vibration signal obtained from one of the faulty motor with BRB is shown Fig. 4.1. We observe in Fig. 4.1(a) that the spectral leakage from the dominant rotational frequency and its harmonics has obscured the fault components. The proposed signal conditioning has attenuated the dominant components and reduced the spectral leakage. As a result, the fault component peaks have conspicuously emerged in Fig. 4.1(b). The RQS estimator, as discussed in Chapter 3, has been used to plot Fig. 4.1.

Algorithm 4 Elimination of dominant frequencies

Input: $\hat{\boldsymbol{\theta}}[n-1]$, $x[n]$, $\boldsymbol{P}[n-1]$, $\boldsymbol{Q}$, $\boldsymbol{R}$.
Output: $\hat{\boldsymbol{\theta}}[n]$, $\boldsymbol{P}[n]$, $\hat{x}_0[n]$.

```
1: for all $n$ such that $n > \tilde{q}$ do
2:     Prediction of state
           $\hat{\boldsymbol{\theta}}[n|n-1] = \hat{\boldsymbol{\theta}}[n-1]$
3:     Prediction of minimum mean squared error
           $\boldsymbol{P}[n|n-1] = \boldsymbol{P}[n-1] + \boldsymbol{Q}$
4:     Evaluation of Kalman gain
           $\boldsymbol{K} = \boldsymbol{P}[n|n-1]\boldsymbol{H}^T[n]\big\{\boldsymbol{H}[n]\boldsymbol{P}[n|n-1]\boldsymbol{H}^T[n] + \boldsymbol{R}\big\}^{-1}$
5:     Correction
           $\hat{\boldsymbol{\theta}}[n] = \hat{\boldsymbol{\theta}}[n|n-1] + \boldsymbol{K}\left\{x[n] - h(\hat{\boldsymbol{\theta}}[n|n-1])\right\}$
6:     If $(\hat{\theta}_i[n] < 0)$ or $(\hat{\theta}_i[n] > 2\pi)$
7:         Re-evaluate Kalman gain with (2.15) and go to step 5.
8:     End If
9:     Signal conditioning
           $\hat{x}_0[n] = x[n] - h(\hat{\boldsymbol{\theta}}[n])$
10:    Minimum mean squared error
           $\boldsymbol{P}[n] = \boldsymbol{I} - \boldsymbol{K}\boldsymbol{H}[n]\boldsymbol{P}[n|n-1]$
11: end for
```

4.3 Minimum Distance Based Detection

To design the test, we use the real part of (1.13) as

$$x(n) = A\cos(\omega n + \phi) + v(n). \tag{4.3}$$

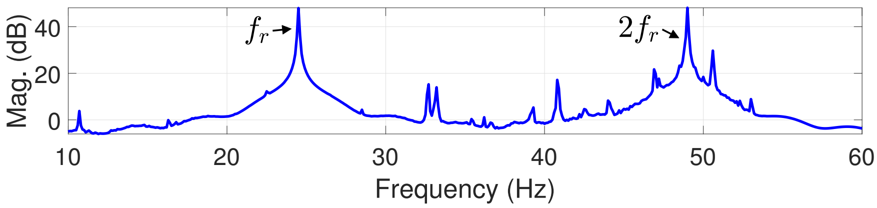

(a) before signal conditioning

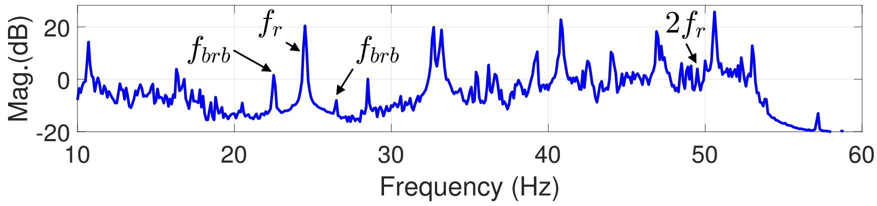

(b) after signal conditioning

Figure 4.1: Spectrum analysis of motor vibration (a) before and (b) after signal conditioning.

The fault frequency (ω) is assumed to be time-invariant, and the hypothesis testing (4.4) is formulated under the assumption that $v(n) \sim \mathcal{N}(0, \sigma^2)$ as

$$\begin{aligned} \mathcal{H}_0 :\quad & x(n) = A\cos(\omega n + \phi) + v(n); \quad A < \gamma, \\ \mathcal{H}_1 :\quad & x(n) = A\cos(\omega n + \phi) + v(n); \quad A \geq \gamma, \end{aligned} \tag{4.4}$$

where γ is the tunable threshold that can be learned from the healthy data. The fault component with noise is represented as

$$x(n) = \alpha_1 \cos(\omega n) + \alpha_2 \sin(\omega n) + v(n),$$

where $A = \sqrt{\alpha_1^2 + \alpha_2^2}$, and $\phi = \arctan\left(-\alpha_2/\alpha_1\right)$. Collating N data points, the observation $\boldsymbol{x}$ is represented as

$$\boldsymbol{x} = \boldsymbol{M}\boldsymbol{\alpha} + \boldsymbol{v},$$

where $\boldsymbol{M} = \begin{bmatrix} 1 & \cdots & \cos(N-1)\omega \\ 0 & \cdots & \sin(N-1)\omega \end{bmatrix}^T$, and $\boldsymbol{\alpha} = \begin{bmatrix} \alpha_1 \\ \alpha_2 \end{bmatrix}$. With $C = \left(2\pi\sigma^2\right)^{-N/2}$, the probability density function of $\boldsymbol{x}$ is given by

$$p\left(\boldsymbol{x};\boldsymbol{\alpha},\sigma^2\right) = C\exp\left[-\left(\boldsymbol{x}-\boldsymbol{M}\boldsymbol{\alpha}\right)^T\left(\boldsymbol{x}-\boldsymbol{M}\boldsymbol{\alpha}\right)/2\sigma^2\right].$$

4.3.1 Parameter Estimates under i^{th} Hypothesis

Under the hypotheses, the parameter estimation turns out to be a constrained optimization problem. The maximum likelihood estimate of the parameters under each hypothesis is obtained by solving the following optimizations using the interior-point algorithm:

$$\mathcal{H}_0: \begin{array}{rl} \hat{\boldsymbol{\alpha}}_0 = \text{minimize}: & \left(\boldsymbol{x}-\boldsymbol{M}\boldsymbol{\alpha}\right)^T\left(\boldsymbol{x}-\boldsymbol{M}\boldsymbol{\alpha}\right) \\ \text{subject to}: & \boldsymbol{\alpha}^T\boldsymbol{\alpha} < \gamma^2, \end{array} \tag{4.5}$$

$$\mathcal{H}_1: \begin{array}{rl} \hat{\boldsymbol{\alpha}}_1 = \text{minimize}: & \left(\boldsymbol{x}-\boldsymbol{M}\boldsymbol{\alpha}\right)^T\left(\boldsymbol{x}-\boldsymbol{M}\boldsymbol{\alpha}\right) \\ \text{subject to}: & \boldsymbol{\alpha}^T\boldsymbol{\alpha} \geq \gamma^2. \end{array} \tag{4.6}$$

4.3.2 Minimum Distance Detector

The minimum distance detector chooses the hypothesis that has the higher conditional likelihood $p\left(\boldsymbol{x};\hat{\boldsymbol{\alpha}}_i,\hat{\sigma}_i^2|\mathcal{H}_i\right)$ [137],

$$p\left(\boldsymbol{x};\hat{\boldsymbol{\alpha}}_i,\hat{\sigma}_i^2|\mathcal{H}_i\right) = C\exp\left[-\frac{\left(\boldsymbol{x}-\boldsymbol{M}\hat{\boldsymbol{\alpha}}_i\right)^T\left(\boldsymbol{x}-\boldsymbol{M}\hat{\boldsymbol{\alpha}}_i\right)}{2\hat{\sigma}_i^2}\right],$$

Alternatively, the hypothesis $\mathcal{H}_i$ is chosen, if the $\mathcal{D}_i^2(x) = \left(\boldsymbol{x}-\boldsymbol{M}\hat{\boldsymbol{\alpha}}_i\right)^T\left(\boldsymbol{x}-\boldsymbol{M}\hat{\boldsymbol{\alpha}}_i\right)$ under that hypothesis is minimum. Neglecting the $\boldsymbol{x}^T\boldsymbol{x}$ term as it is same under both the hypothesis, we have

$$\mathcal{D}_i^2(x) = -2\boldsymbol{x}^T \boldsymbol{M}\hat{\boldsymbol{\alpha}}_i + \hat{\boldsymbol{\alpha}}_i^T \boldsymbol{M}^T \boldsymbol{M}\hat{\boldsymbol{\alpha}}_i. \tag{4.7}$$

Rearranging the terms of (4.7), we define the test statistic for $\mathcal{H}_i$ as

$$\mathcal{T}_i(x) = \boldsymbol{x}^T \boldsymbol{M}\hat{\boldsymbol{\alpha}}_i - \frac{1}{2}\hat{\boldsymbol{\alpha}}_i^T \boldsymbol{M}^T \boldsymbol{M}\hat{\boldsymbol{\alpha}}_i. \tag{4.8}$$

The individual hypotheses are obtained by using the value of α_i from (4.5) and (4.6). The hypothesis $\mathcal{H}_i$ is selected for which the $\mathcal{T}_i(x)$ is maximum. The total probability of error $\mathcal{P}_e$ is

$$\mathcal{P}_e = \mathcal{P}(\mathcal{H}_1|\mathcal{H}_0)\mathcal{P}(\mathcal{H}_0) + \mathcal{P}(\mathcal{H}_0|\mathcal{H}_1)\mathcal{P}(\mathcal{H}_1),$$

where $\mathcal{P}(\mathcal{H}_i|\mathcal{H}_j)$ is the conditional probability of $\mathcal{H}_i$ given $\mathcal{H}_j$. We assign the prior probability $p(\mathcal{H}_i) = 0.5$ for both the hypotheses. Therefore,

$$\mathcal{P}_e = 0.5\mathcal{P}(T_1(x) > T_0(x)|\mathcal{H}_0) + 0.5\mathcal{P}(T_0(x) > T_1(x)|\mathcal{H}_1)$$

$$= 0.5\mathcal{P}(T_1(x) - T_0(x) > 0|\mathcal{H}_0) + 0.5\mathcal{P}(T_1(x) - T_0(x) < 0|\mathcal{H}_1). \tag{4.9}$$

The aggregate error of classification is given by $\mathcal{P}_e$. Also, $\mathcal{P}(\mathcal{H}_i)$ can be updated with the history of the motor.

4.4 Implementation of the Algorithm

The implementation of the fault detection system, as illustrated in Fig. 4.2, is described as follows:

1. The acquired vibration signal, $x(n)$, is down-sampled for adequate frequency

resolution with appropriate anti-alias filtering. The data is then sent to the signal conditioner. In this work, the sampling rate is fixed to 400 samples/s for all the data.

2. The signal conditioner estimates the fundamental rotational frequency (f_r) and removes the dominant components. The conditioned vibration signal $\hat{x}_0(n)$ is then stored in a buffer.
3. The specification of the motor, bearings, and value of the f_r is used to find the theoretical fault frequency.
4. A small band is searched around the central frequency by the RQS estimator (Chapter 3), and the peak (ω) is detected.
5. The threshold (γ), buffered $\hat{x}_0(n)$, and ω are then sent for hypothesis testing, and the presence of fault is decided by the test statistic $T_0(x)$ and $T_1(x)$.

4.5 Experimental Results

This spectral plots of this chapter are normalized by the rotational frequency magnitude and are then scaled between zero and one for uniformity. The RQS estimator (chapter 3) is used for obtaining the spectrum.

4.5.1 Inner Raceway Fault Detection

We have used the damaged inner raceway for multiple experiments using the lab-setup to compare the faulty motor signature with a healthy motor. Figure 4.3 shows the spectrum of the conditioned vibration signal from the single axis (driving end) sensor with two different load conditions. With increased loading, identifying the inner-raceway fault component has improved considerably as the number of

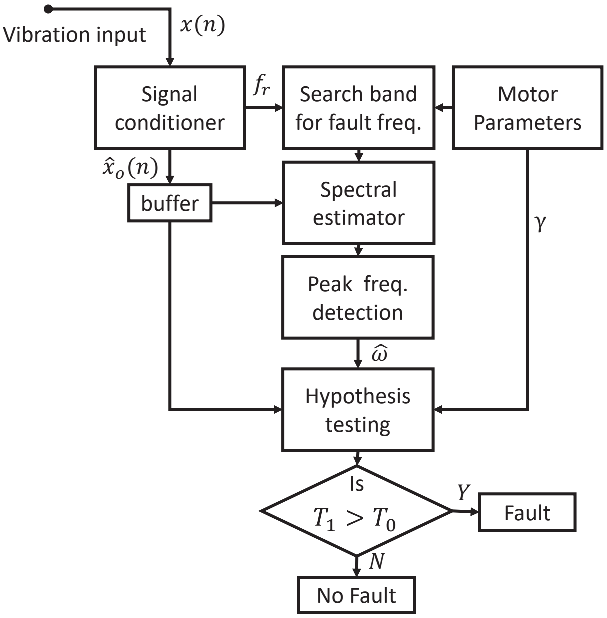

(a)

Figure 4.2: Implementation of the complete fault detection algorithm.

spurious peaks has reduced. The fault component for the CWRU data is quite prominent for all the cases. Figure 4.4 gives the vibration spectrum with a 0.007-inch (0.1778 mm) fault for no-load and 3-HP load, respectively. The vibration spectrum for increased severity with the 0.028-inch (0.7112 mm) fault in the inner-raceway for two load conditions is shown in Fig. 4.5. For the CWRU data, the fault components are considerably prominent for all the cases, and they match with the theoretical fault component.

4.5.2 Outer Raceway Fault Detection

In the case of an outer-raceway fault, we have carried out the same experiment set with a hole drilled into the outer raceway. Proper care was taken so as not to damage the rolling element. Figure 4.6 shows the conditioned vibration spectrum of the experimental setup for two load cases. With increased loading, few

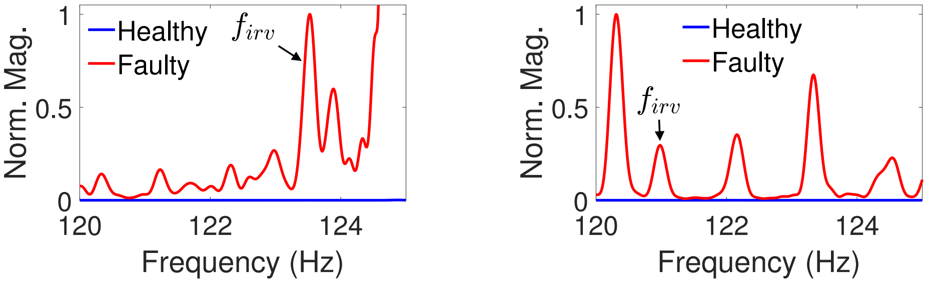

(a) Low load, 0.2% slip, $f_r = 24.95$ Hz, $f_{irv} = 123.5$ Hz.

(b) 67% load, 1.93% slip, $f_r = 24.52$ Hz, $f_{irv} = 121$ Hz.

Figure 4.3: Spectrum of the conditioned vibration signal obtained from the lab-setup, with inner-race fault for different load levels.

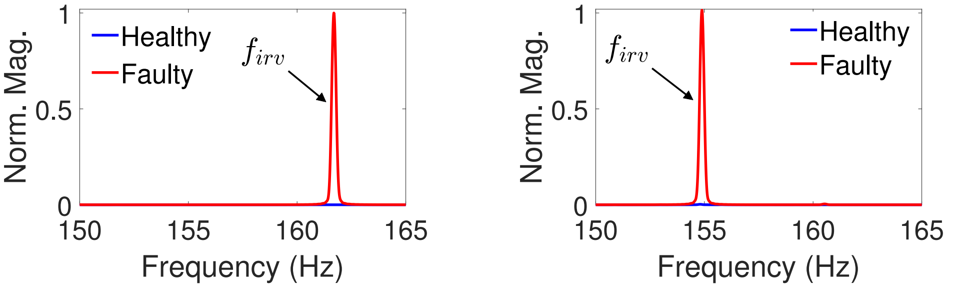

(a) Low load of 0 HP, $f_r = 29.95$ Hz, $f_{irv} = 161.7$ Hz.

(b) High load of 3 HP, $f_r = 28.83$ Hz, $f_{irv} = 155$ Hz.

Figure 4.4: Vibration spectrum of CWRU data for detecting a 0.007-inch inner raceway fault for two load levels.

additional components appear in the vicinity of the fault-component. However, the outer-raceway fault component magnitude normalized by the magnitude of the rotation frequency component is prominent in both cases. Accurate frequency estimation by the proposed method reduces the chances of misclassification due to spurious peaks. We have applied the same set of analyses to the CWRU data for detecting the outer raceway fault. We have selected two load cases for the two levels of fault severity. The spectrum with the 0.007-inch defect for the two loads is shown in Fig. 4.7. The fault components are pronounced, and they match

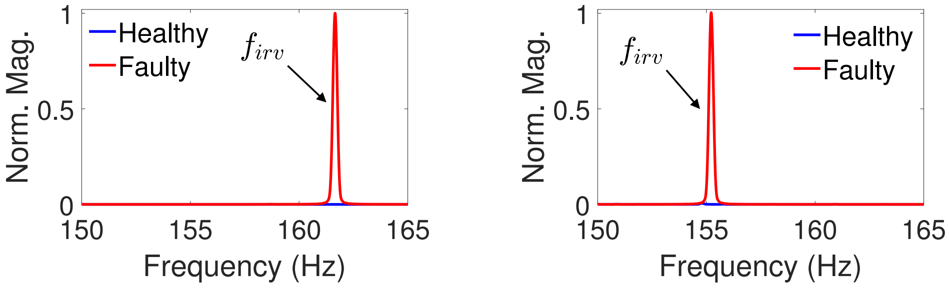

(a) 0 HP load, $f_r = 29.95$ Hz, $f_{irv} = 161.7$ Hz.

(b) 3 HP load, $f_r = 28.83$ Hz, $f_{irv} = 155.2$ Hz.

Figure 4.5: Vibration spectrum of CWRU data for detecting a damaged inner raceway with increased severity of 0.028-inch fault for two load cases.

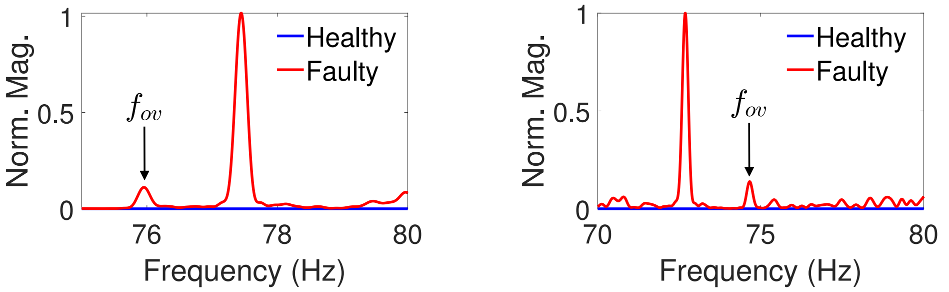

(a) Low load, 0.13% slip, $f_r = 24.96$ Hz, $f_{orv} = 75.95$ Hz.

(b) 60% load, 1.8% slip, $f_r = 24.55$ Hz, $f_{orv} = 74.67$ Hz.

Figure 4.6: Spectrum of the conditioned vibration signal obtained from the lab-setup, with an outer raceway fault for different load levels.

with the theoretical component. The vibration spectrum with increased severity of the 0.021-inch (0.5334 mm) fault is shown in Fig. 4.8. The healthy data exhibits minor frequency components in the observed band for the higher load. However, the magnitudes are low, and they do not match the theoretical fault frequency. When compared with the healthy cases, it can be summarized that the proposed method is successful in separating the faulty cases from healthy ones.

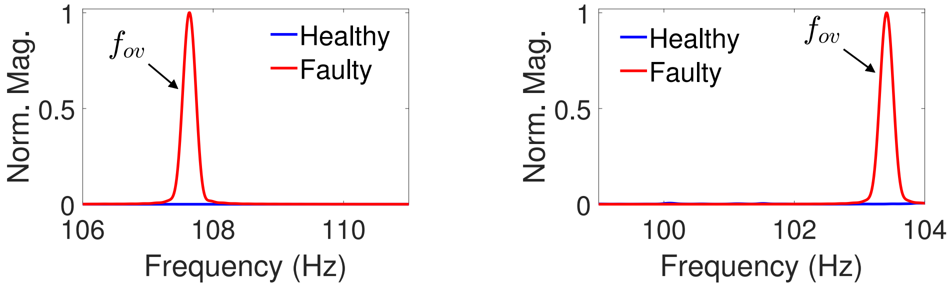

(a) Low load of 0 HP, $f_r = 29.95$ Hz, $f_{orv} = 107.6$ Hz.

(b) High load of 3 HP, $f_r = 28.83$ Hz, $f_{orv} = 103.4$ Hz.

Figure 4.7: Vibration spectrum of CWRU data for detecting an incipient 0.007-inch outer raceway fault.

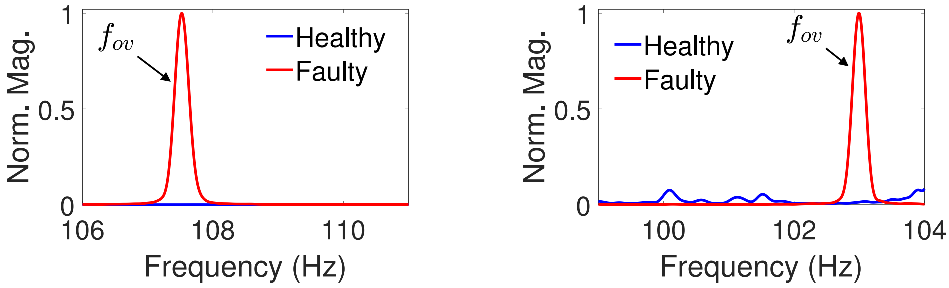

(a) Low load of 0 HP, $f_r = 29.95$ Hz, $f_{orv} = 107.5$ Hz.

(b) High load of 3 HP, $f_r = 28.83$ Hz, $f_{orv} = 103$ Hz.

Figure 4.8: Vibration spectrum of CWRU data for detecting a 0.021-inch outer raceway fault.

4.5.3 Rolling Element Fault Detection

The rolling element fault signature of bearing is presented in Fig. 4.9. The detectability with the lab-setup bearing is quite challenging due to the high magnitude frequency component in the vicinity of the theoretical fault component. The fault component is further subdued when the load is increased. However, a narrow search band and an accurate frequency estimate can correctly identify the fault-component.

For the small-sized CWRU bearings, the visibility of the fault-frequency com-

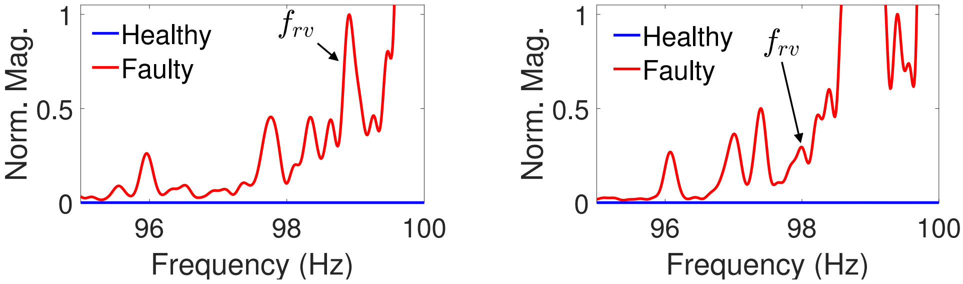

(a) Low load, 0.06% slip, $f_r = 24.99$ Hz, $f_{rv} = 98.91$ Hz.

(b) 40% load, 1.13% slip, $f_r = 24.73$ Hz, $f_{rv} = 98$ Hz.

Figure 4.9: Rolling element fault vibration spectrum for different load scenarios, obtained from the lab-setup.

ponent is quite pronounced. Figure 4.10 shows the vibration spectrum of the CWRU data with a 0.007-inch defect for two load cases, whereas Fig. 4.11 shows the spectrum for a 0.028-inch fault in the rolling element. It is seen in Fig. 4.11(b) that multiple frequency components appear in the healthy motor spectrum for the high load. However, misclassification due to its presence is minimal as the components do not match with the theoretical fault component.

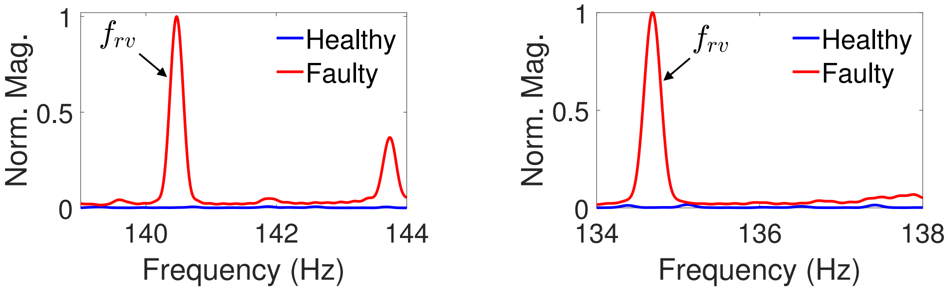

(a) 0 HP load, $f_r = 29.95$ Hz, $f_{rv} = 140.5$ Hz.

(b) 3 HP load, $f_r = 28.83$, $f_{rv} = 134.7$ Hz.

Figure 4.10: Vibration spectrum of CWRU data for detecting an incipient 0.007-inch rolling element fault for different loads.

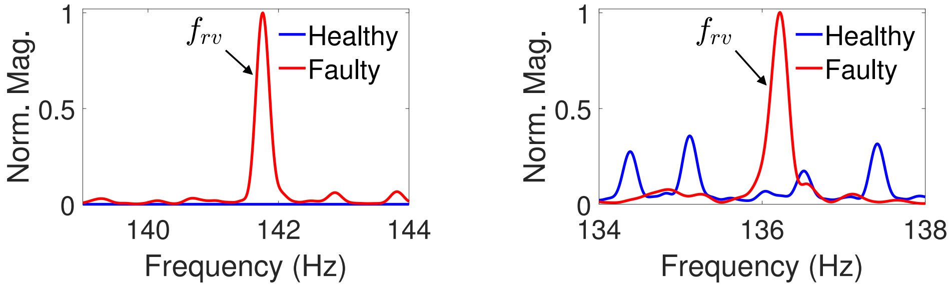

(a) 0 HP load, $f_r = 29.95$ Hz, $f_{rv} = 141.8$ Hz.

(b) 3 HP load, $f_r = 28.83$ Hz, $f_{rv} = 136.2$ Hz.

Figure 4.11: Vibration spectrum of CWRU data for detecting a severe 0.028-inch rolling element fault for two load levels.

4.5.4 Cage Fault Detection

The cage of the rolling element was inadvertently damaged while simulating the rolling element fault. Specific frequency regions were searched, and it was found in Fig. 4.12 that the proposed method has successfully detected the fault-component. With increased loading, the fault component has become more pronounced and can be easily distinguished.

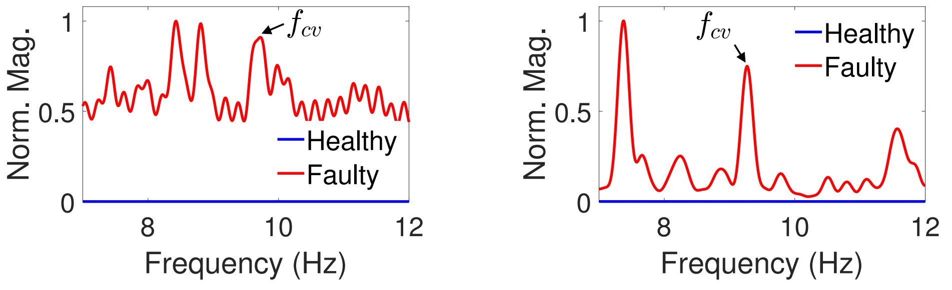

(a) Low load, 0.2% slip, $f_r = 24.95$ Hz, $f_{cv} = 9.72$ Hz.

(b) 67% load, 1.93% slip, $f_r = 24.51$ Hz, $f_{cv} = 9.26$ Hz.

Figure 4.12: Cage fault spectrum extracted from the vibration signal using the lab-setup.

Similar results were also observed with the CWRU data. However, there was no information regarding the cage fault defect in CWRU data [15]. The rolling-element data was used for detecting the presence of cage fault components. Figure 4.13 and Fig. 4.14 shows the spectrum relevant to the frequency band of cage fault for 0.007-inch and 0.028-inch rolling element fault, respectively. We assume that the cages were damaged while introducing faults in the rolling element. The presence of the cage-fault specific frequency in all the cases validates the assumption. In the low-load instances, for both the severity of CWRU data, multiple frequency components are observed in the vicinity of the fault component. However, with increased load, fault magnitude has increased considerably, and has become more prominent.

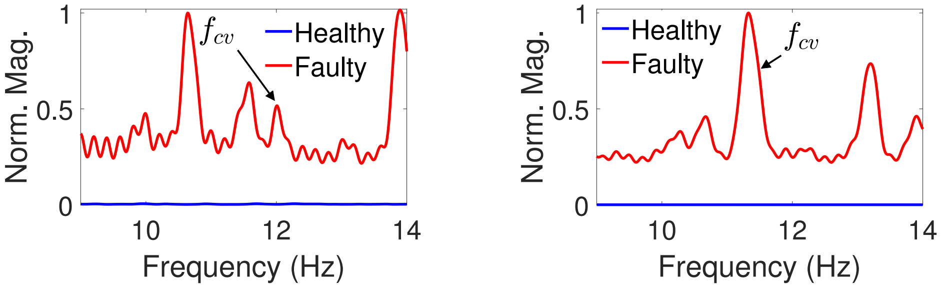

(a) Low load, 0 HP, f_r = 29.95 Hz, f_{cv} = 12.02 Hz.

(b) High load, 3 HP, f_r = 28.83 Hz, f_{cv} = 11.33 Hz.

Figure 4.13: Vibration spectrum of CWRU data for detecting a 0.007-inch cage-train fault.

4.5.5 Broken Rotor Bar Detection

The damaged rotor of the motor was used for validating the signatures under a single broken rotor bar fault. The first condition is tested with the motor running under no external load, except the inertia of the coupled generator. The spectrum of the faulty case, when compared to the healthy motor, is shown in Fig. 4.15(a). In this case, the slip is low, and the fault component is close to the fundamental rotational frequency. However, signal conditioning by removing the

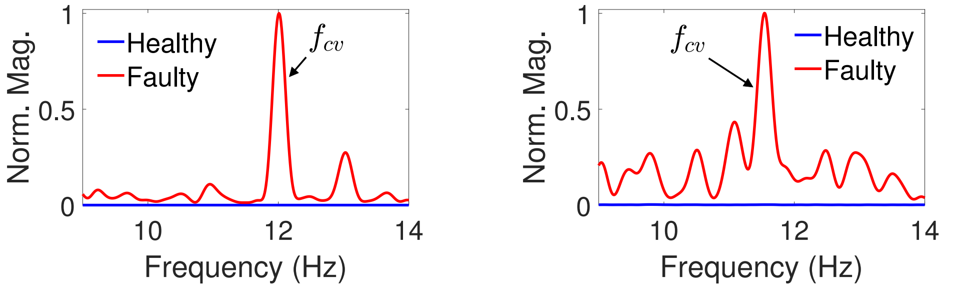

(a) Low load, 0 HP, f_r = 29.95 Hz, f_{cv} = 12.01 Hz.

(b) High load of 3 HP, f_r = 28.83 Hz, f_{cv} = 11.55 Hz.

Figure 4.14: Vibration spectrum of CWRU data for detecting a 0.028-inch cage-train fault.

rotational frequency and its harmonic has negated the spectral leakage, and the fault harmonics are visible. Specifically, the fourth fault harmonic is observed for the low-load. No such component is visible for the healthy case. For the healthy motor, signal conditioning had almost removed the rotational frequency. When the load is increased, the principal fault component has become more prominent, as seen in Fig. 4.15(b), and the magnitudes are also higher compared to the healthy case.

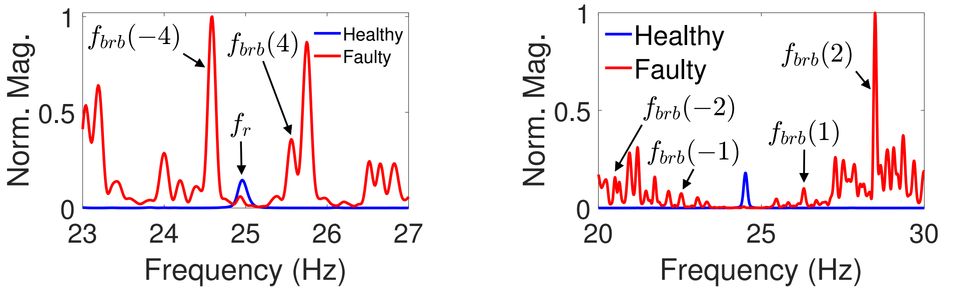

(a) Low load, 0.2% slip.

(b) 70%load, 2% slip

Figure 4.15: Vibration spectrum of experimental data for detecting a single broken rotor bar fault. For (a) $f_{brb}(-4)$ = 24.58 Hz, $f_{brb}(4)$ = 25.56 Hz, and for (b) $f_{brb}(-2)$ = 20.51 Hz, $f_{brb}(-1)$ = 22.54 Hz, $f_{brb}(1)$ = 26.31 Hz, $f_{brb}(2)$ = 28.49 Hz.

4.5.6 Hypothesis Testing and Fault Detection Statistics

A Monte-Carlo simulation (MCS) is conducted to determine the detector performance using a synthetic signal. The parameters of the input signal (4.3) used for the MCS are $\omega \sim \mathcal{U}(0.01\pi, 0.5\pi)$, $\phi \sim \mathcal{U}(0, \pi)$, $\mathcal{P}(A|\mathcal{H}_0) \sim \mathcal{U}(0, \gamma - \tau)$, $\mathcal{P}(A|\mathcal{H}_1) \sim \mathcal{U}(\gamma + \tau, 10)$, and $\gamma = 5$, $\mathcal{U}(a, b)$ denotes the uniform distribution within the range a and b. The tolerance τ decides the separation between the two hypotheses from which A is drawn. Figure 4.16 shows the effect of the input SNR on the detector's performance for different values of tolerance. We observe that with increasing SNR, the detector performance improves as the probability of detection increases, and the likelihood of false alarm decreases, which demonstrates the noise-robustness of the detector. Also, the performance of the detector improves as τ increases. We have carried out 1000 trials for each SNR value.

The robustness of the overall fault detection scheme can be judged by the noise performance of individual modules of the algorithm. The components that are to be suppressed, in general, have high-SNR. The performance of the signal conditioner can be assessed by its frequency estimation accuracy, which is superior under high-SNR [93]. Similarly, the spectral estimator can estimate the low-magnitude fault components accurately, as shown in [16].

The data from the lab-setup and CWRU were analyzed separately to gauge the accuracy of the overall fault detection unit. We have conditioned the data and then estimated the spectrum in a small band around the theoretical fault frequency. The peak spectral amplitude of all the healthy-motor data is augmented, and the maximum value is set as the threshold γ. The conditioned data from each faulty and healthy cases were tested for the given hypothesis (4.4) using γ. The test was repeated for different loads of each healthy and faulty data. The performance of the overall fault detection algorithm is provided in Table 4.1. From Table 4.1, we observe that all the fault cases from CWRU were successfully detected using the

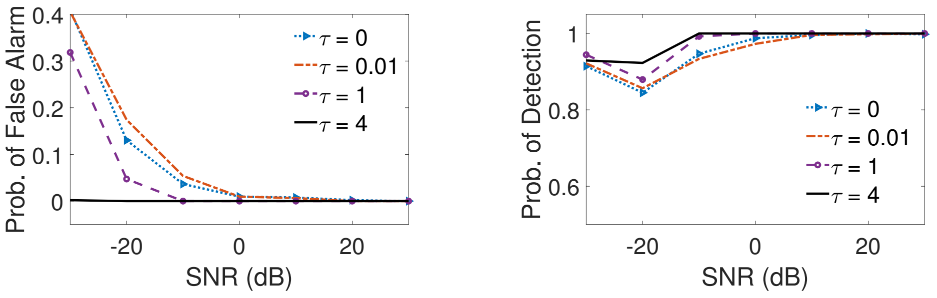

(a) Effect on the probability of false alarm

(b) Effect on the probability of detection

Figure 4.16: Effect of SNR for different values of tolerances (τ) on the probability of false alarm and probability of detection for the designed detector.

proposed method. The detection accuracy with the lab-setup data is also high. The percentage accuracy can be calculated as $(1 - \mathcal{P}_e) * 100$ by using the value of $\mathcal{P}_e$ from (4.9). The existing margin of classification error of the lab-setup data can be attributed to multiple low-load data and the well-known challenges of detecting faults of a medium-sized SCIM.

Table 4.1: Fault detection performance

Fault type	Percentage accuracy	
	lab-setup data	CWRU data
Broken rotor bar	95.09 %	Not available
Rolling element fault	98.44 %	100 %
Cage defect	98.36 %	100 %
Inner raceway fault	90.33 %	100 %
Outer raceway fault	96.77 %	100 %

A comparison with the best performers that have used CWRU data is given in Table 4.2. The proposed method has achieved 100% accuracy like few existing state-of-the-art methods. However, the non-requirement of fault data for fixing the threshold, minimal use of computational resources for training, and proposed generic nature of the algorithm set it apart from the others.

Table 4.2: Detection accuracy for CWRU dataset

Reference, year	Detection Accuracy (%)	Fault data required (Y/N)
[154], 2020	99.58	Y
[155], 2020	100	Y
[156], 2019	99.93	Y
[157], 2019	100	Y
[66], 2018	99.95	Y
[158], 2018	100	Y
[159], 2016	99.83	Y
[160], 2015	99.55	Y
Proposed work	100	N

4.6 Conclusions

This chapter has proposed a fault detection method for SCIMs using single-axis data from a tri-axial vibration sensor. The algorithm has been used to detect different bearing faults and a single BRB under low and high loads using data from a 22-kW SCIM laboratory setup. Additionally, publicly available CWRU data was also used for evaluation. The method can also be extended for detecting other faults whose spectral signatures are known.

The EKF-based conditioning can track, estimate, and remove multiple dominant frequency components. The conditioning reduces the spectral leakage and aids in the accurate estimation of the fault amplitude. The spectral estimator used in this work has low-complexity and is suitable for portable embedded implementations, which is quite necessary for the Internet of things (IoT)-enabled Industry 4.0 standard. We observed that the magnitude of the rotational frequency component plays a vital role in normalizing and distinguishing the fault cases. The hypothesis testing scheme improves the detection under noisy conditions and reduces false alarms by incorporating the inherent fault magnitude in healthy cases.

The proposed method has successfully detected all the healthy and faulty-motor cases of the drive-end 12 kHz CWRU data with 100% accuracy. Moreover, unlike DL and ML-based methods, this method only needs a few healthy cases for determining the threshold. The method can be expanded to IoT-based Edge devices for cloud-based anomaly detection of SCIMs. However, this would require further studies into the method's memory, speed, and power requirement. Additionally, the procedure can be extended to detect faults in associated loads coupled to the motors and their bearings from the motor vibrations themselves.

CHAPTER 5

Bayes Maximum a-Posterior Spectral Estimation for Stator Current Analysis

A Bayesian framework for spectral estimation of a stationary signal is proposed. The prior probability of the parameters is chosen based on the first-order Gauss-Markov process. The posterior density is defined for a time-varying autoregressive (TVAR) model conditioned on the prior density. We have used maximum-a-posterior estimation to find the TVAR parameters. The estimation involves a regularized least square solution. The regularization step circumvents the inversion of the ill-conditioned autocorrelation matrix. The resolution of the proposed method is independent of the data length. However, increased observation results in the reduction of the mean squared error. The state and observation noise variances have been estimated iteratively. The overall implementation of the algorithm is also provided. Additionally, we have compared the proposed method with established available methods.

The proposed method has been used to estimate the spectrum of the conditioned stator current for detecting SCIM defects. The fault detection algorithm has been tested and validated on the experimental laboratory setup, as discussed in Section 3.5.

5.1 Contribution of the Chapter

The contribution of this chapter can be enumerated as

1. We propose a Bayesian model-based sequential spectral estimator. A Gauss-Markov random walk model has been used to model the uncertainty of the TVAR process. The accuracy is better than classical methods and is on par with AR-spectrum and MUSIC. It is especially suited for low-data and RT applications. A sequential algorithm is also established to estimate the associated latent variables.
2. The proposed high-resolution spectral estimator has been applied for detecting different faults of a SCIM.
3. The proposed method is implemented on an IoT-based framework for low data-rate applications.

Outline: The chapter is structured as follows: Section 3.2 describes the proposed spectral estimator and its statistical evaluation, followed by a discussion on the statistical resolution of the method in Section 3.3. Section 3.4 presents the fault detection scheme using the previously proposed signal conditioning and slip estimation, followed by fault detection results in Section 3.6. Section 3.7 summarizes and concludes the chapter.

5.2 Signal Model and Problem Formulation

A $q-$component sinusoidal signal $x(n)$ with amplitude A_i, normalized frequency ω_i, and phase ϕ_i defined as the real component of (1.13) is given as

$$x(n) = \sum_{i=1}^{q} A_i \cos(n\omega_i + \phi_i), \tag{5.1}$$

and $\omega_i = 2\pi f_i/F_s$ with $j = \sqrt{-1}$. f_i and F_s are the i^{th} signal frequency (Hz) and sampling rate (samples/s), respectively. A TVAR model with parameters a_i can represent the above signal as

$$x(n) = \sum_{i=1}^{p} a_i(n)x(n-i) + v(n), \tag{5.2}$$

where $p = 2q$, and $v(n)$ is the additive white Gaussian noise with zero mean and covariance σ_v^2, i.e., $v(n) \sim N(0, \sigma_v^2)$. We start the iteration from $n = p$ to maintain causality. Hence, (5.2) can be expressed by a linear model as

$$x(n) = \boldsymbol{a}^T(n)\boldsymbol{x}(n-1) + v(n),$$

where $\boldsymbol{a}(n) = \begin{bmatrix} a_1(n) & a_2(n) & \cdots & a_p(n) \end{bmatrix}^T$, and

$$\boldsymbol{x}(n) = \begin{bmatrix} x(n) & x(n-1) & \cdots & x(n-p+1) \end{bmatrix}^T.$$

Now suppose we are observing the n^{th} input data. Based on this input, we intend to estimate $\boldsymbol{a}(n)$ at n^{th} sample instance. During the transition from p^{th} sample to n^{th} sample, we assume that the parameters $a_i(n)$'s do not change. A non-changing parameter-set is a valid assumption as the signal under consideration is stationary with invariable frequency components.

5.3 Maximum-a-posteriori Spectral Estimation

The probability density function (PDF) of $x(n)$ conditioned on parameters $a_i(n)$ is given as

$$p\left(x(n)|\boldsymbol{x}(n-1),\boldsymbol{a}(n)\right)=\frac{1}{\sqrt{2\pi\sigma_v^2}}\exp\left\{\frac{-\left[x(n)-\boldsymbol{a}^T(n)\boldsymbol{x}(n-1)\right]^2}{2\sigma_v^2}\right\}.$$

The joint distribution of the observation using the chain rule is given as

$$p\left(\boldsymbol{x}(n)|\boldsymbol{x}(n-1),\boldsymbol{a}(n)\right)=\prod_{i=p}^{n}p\left(x(i)|x(i-1)\cdots x(i-p+1),\boldsymbol{a}(n),\sigma_v^2\right) \tag{5.3}$$

Hence,

$$p\left(\boldsymbol{x}(n)|\boldsymbol{x}(n-1),\boldsymbol{a}(n)\right)=k_1\exp\left\{-\sum_{i=p}^{n}\frac{\left[x(i)-\boldsymbol{a}^T(n)\boldsymbol{x}(i-1)\right]^2}{2\sigma_v^2}\right\} \tag{5.4}$$

where $k_1=(2\pi\sigma_v^2)^{-(n-p+1)/2}$. To introduce uncertainty in the model parameters, we define the parameter $\boldsymbol{a}(n)$ as a first-order Gauss-Markov random walk. The random-walk enables the sequential estimation paradigm and is given as

$$\boldsymbol{a}(n)=\boldsymbol{a}(n-1)+\boldsymbol{u}(n), \tag{5.5}$$

where $\boldsymbol{u}(n)\sim\mathcal{N}\left(\boldsymbol{0},\sigma_u^2\boldsymbol{I}\right)$, $\boldsymbol{0}$ is a vector with p zeros, and $\boldsymbol{I}$ is the $p-$dimensional identity matrix.

5.3.1 Posterior Probability Density of the Parameter

The posterior probability of the parameter $\boldsymbol{a}(n)$ conditioned on the observation is given by

$$p\left(\boldsymbol{a}(n)|\boldsymbol{x}(n)\right)=\frac{p\left(\boldsymbol{x}(n)|\boldsymbol{a}(n)\right)p\left(\boldsymbol{a}(n)\right)}{p\left(\boldsymbol{x}(n)\right)} \tag{5.6}$$

The prior distribution of the parameter denoted by $p(\boldsymbol{a}(n))$ is derived from (5.5) as

$$p\left(\boldsymbol{a}(n)\right) = k_2 \exp\left\{-\frac{1}{2\sigma_u^2}\left[\boldsymbol{a}(n)-\boldsymbol{a}(n-1)\right]^T\left[\boldsymbol{a}(n)-\boldsymbol{a}(n-1)\right]\right\}, \tag{5.7}$$

where $k_2 = (2\pi\sigma_u^2)^{-p/2}$. Therefore, putting (5.4) and (5.7) in (5.6), we have

$$\begin{aligned} p\left(\boldsymbol{a}(n)|\boldsymbol{x}(n)\right) \propto & k_1 k_2 \exp\left\{-\sum_{i=p}^{n}\frac{\left[x(i)-\boldsymbol{a}^T(n)\boldsymbol{x}(i-1)\right]^2}{2\sigma_v^2}\right\} \\ & \exp\left\{-\frac{1}{2\sigma_u^2}\left[\boldsymbol{a}(n)-\boldsymbol{a}(n-1)\right]^T\left[\boldsymbol{a}(n)-\boldsymbol{a}(n-1)\right]\right\} \end{aligned} \tag{5.8}$$

5.3.2 Parameter Estimation

For simplification, we take natural logarithms on both sides of (5.8). Maximizing the log-function with respect to the unknown parameter maximizes the posterior PDF. The value of the parameter, where the posterior PDF is maximized is the MAP-estimate of the parameter. The log-PDF is given as

$$\begin{aligned} \ln p\left(\mathbf{a}(n)|\boldsymbol{x}(n)\right) = c_2 - & \sum_{i=p}^{n}\frac{\left[x(i)-\boldsymbol{a}^T(n)\boldsymbol{x}(i-1)\right]^2}{2\sigma_v^2} \\ & -\frac{1}{2\sigma_u^2}\left[\boldsymbol{a}(n)-\boldsymbol{a}(n-1)\right]^T\left[\boldsymbol{a}(n)-\boldsymbol{a}(n-1)\right], \end{aligned} \tag{5.9}$$

where $c_2 = \ln(k_1 k_2)$ is a constant independent of $\boldsymbol{a}(n)$. Now, by equating

$$\partial \ln p\left(\boldsymbol{a}(n)|\boldsymbol{x}(n)\right)/\partial \boldsymbol{a}(n) = 0,$$

we have:

$$\sum_{i=p}^{n}\boldsymbol{x}(i-1)x(i) = \left\{\sum_{i=p}^{n}\boldsymbol{x}(i-1)\boldsymbol{x}^T(i-1)\right\}\boldsymbol{a}(n) + \frac{\sigma_v^2}{\sigma_u^2}\left[\boldsymbol{a}(n)-\boldsymbol{a}(n-1)\right]. \tag{5.10}$$

From (5.10) we denote $\boldsymbol{\rho}_{\boldsymbol{x}}(n) = \sum_{i=p}^{n} \boldsymbol{x}(i-1)x(i)$, $\boldsymbol{R}_{\boldsymbol{xx}}(n) = \sum_{i=p}^{n} \boldsymbol{x}(i-1)\boldsymbol{x}^T(i-1)$, and $\kappa = \sigma_v^2/\sigma_u^2$, to get

$$\boldsymbol{\rho}_{\boldsymbol{x}}(n) + \kappa \boldsymbol{a}(n-1) = \{\boldsymbol{R}_{\boldsymbol{xx}}(n) + \kappa \boldsymbol{I}\} \boldsymbol{a}(n)$$

therefore, a recursive estimate of the parameter $\boldsymbol{a}(n)$ in terms of its past value is obtained by regularized least squares as

$$\hat{\boldsymbol{a}}(n) = \left[\boldsymbol{R}_{\boldsymbol{xx}}(n) + \kappa \boldsymbol{I}\right]^{-1} \left[\boldsymbol{\rho}_{\boldsymbol{x}}(n) + \kappa \boldsymbol{a}(n-1)\right] \tag{5.11}$$

5.3.3 Recursive estimation of $\boldsymbol{R}_{\boldsymbol{xx}}(n)$ and $\boldsymbol{\rho}_{\boldsymbol{x}}(n)$

We have defined $\boldsymbol{\rho}_{\boldsymbol{x}}(n)$ as

$$\boldsymbol{\rho}_{\boldsymbol{x}}(n) = \sum_{i=p}^{n} \boldsymbol{x}(i-1)x(i).$$

We can decompose $\boldsymbol{\rho}_{\boldsymbol{x}}(n)$ as

$$\boldsymbol{\rho}_{\boldsymbol{x}}(n) = \sum_{i=p}^{n-1} \boldsymbol{x}(i-1)x(i) + \boldsymbol{x}(n-1)x(n).$$

Therefore,

$$\boldsymbol{\rho}_{\boldsymbol{x}}(n) = \boldsymbol{\rho}_{\boldsymbol{x}}(n-1) + \boldsymbol{x}(n-1)x(n), \tag{5.12}$$

similarly,

$$\boldsymbol{R}_{\boldsymbol{xx}}(n) = \boldsymbol{R}_{\boldsymbol{xx}}(n-1) + \boldsymbol{x}(n-1)\boldsymbol{x}^T(n-1) \tag{5.13}$$

5.3.4 The Spectral Estimation

The power spectral density of the input signal is obtained by using the estimated parameter-vector $\hat{a}_i(n)$ as (2.11)

$$\boldsymbol{P_x}(\omega, n) = \hat{\sigma}_v^2 \Bigg/ \left| 1 - \sum_{i=1}^{p} \hat{a}_i(n) e^{-j\omega(i-1)} \right|^2,$$

5.3.5 Estimation of State and Observation Noise Variances

The PDF with unknown observation noise variance is given by (5.4). An MLE of the variance is obtained by maximizing the PDF with respect to σ_v^2 as

$$\partial \ln p\left(\boldsymbol{x}(n) | \boldsymbol{a}(n)\right) \big/ \partial \sigma_v^2 = 0. \tag{5.14}$$

The estimated noise variance is thus obtained as

$$\hat{\sigma}_v^2 = \frac{1}{n-p+1} \sum_{i=p}^{n-1} \left[x(i) - \hat{\boldsymbol{a}}^T(n)\boldsymbol{x}(i-1)\right]^2,$$

The recursive counterpart of $\hat{\sigma}_v^2$ is given by

$$\hat{\sigma}_v^2(n) = \frac{(n-p)\hat{\sigma}_v^2(n-1) + \left[x(n) - \hat{\boldsymbol{a}}^T(n)\boldsymbol{x}(n-1)\right]^2}{n-p+1}.$$

Similarly, σ_u^2 is obtained by solving $\partial \ln p\left(\boldsymbol{a}(n)\right)/\partial\sigma_u^2 = 0$. $p\left(\boldsymbol{a}(n)\right)$ is obtained from (5.6). The MLE is given as

$$\hat{\sigma}_u^2(n) = \frac{1}{p} \left\| \hat{\boldsymbol{a}}(n) - \hat{\boldsymbol{a}}(n-1) \right\|_2^2.$$

5.3.6 Implementation of the Spectral Estimator

The implementation of the sequential spectral estimator is summarized in Algorithm 5.

Algorithm 5 Sequential spectral estimation

```
Input: $\hat{\boldsymbol{a}}(n-1)$, $x(n)$, $\boldsymbol{R_{xx}}(n-1)$, $\boldsymbol{\rho_x}(n-1)$, $\hat{\sigma}_u^2(n-1)$, $\hat{\sigma}_v^2(n-1)$.
Output: $\hat{\boldsymbol{a}}(n)$, $P(\omega)$.
for all $n$ such that $n > p$ do
    $\boldsymbol{R_{xx}}(n) = \boldsymbol{R_{xx}}(n-1) + \boldsymbol{x}(n-1)\boldsymbol{x}^T(n-1)$
    $\boldsymbol{\rho_x}(n) = \boldsymbol{\rho_x}(n-1) + \boldsymbol{x}(n-1)x(n)$
    $\hat{\sigma}_v^2(n) = \frac{1}{n-p+1}\left[\hat{\sigma}_v^2(n) + \left\{x(n) - \hat{\boldsymbol{a}}^T(n)\boldsymbol{x}(n-1)\right\}^2\right]$
    $\hat{\sigma}_u^2(n) = \frac{1}{p}\left\|\hat{\boldsymbol{a}}(n) - \hat{\boldsymbol{a}}(n-1)\right\|_2^2$
    $\kappa(n) = \sigma_v^2(n)/\sigma_u^2(n)$
    $\hat{\boldsymbol{a}}(n) = \left[\boldsymbol{R_{xx}}(n) + \kappa\boldsymbol{I}\right]^{-1}\left[\boldsymbol{\rho_x}(n) + \kappa\boldsymbol{a}(n-1)\right]$
    $\boldsymbol{x}(n) = \left[x(n), \boldsymbol{x}^T(n-1)\right]^T$
end for
$P(\omega, n) = \hat{\sigma}_v^2(n) \Big/ \left|\sum_{i=0}^{p} \hat{a}_i[n] e^{-j\omega}\right|^2$,
```

5.4 Evaluation of the Proposed Spectral Estimator

We evaluate the peak-MSE of the spectrum and how it is affected by the input SNR as shown in Fig. 5.1. For this simulation, 100 trials are performed for each SNR. The noise is generated from a Gaussian distribution with zero mean and appropriate variance for each trial. The true frequency of the signal was kept constant at 50.11 Hz, and amplitude was fixed at 1 unit. The performance of all the spectral estimators follows each other quite closely. If observed minutely, the proposed estimator performs marginally better when the SNR is high. However, its performance is comparable to the AR-spectrum. The Cramer-Rao lower bound

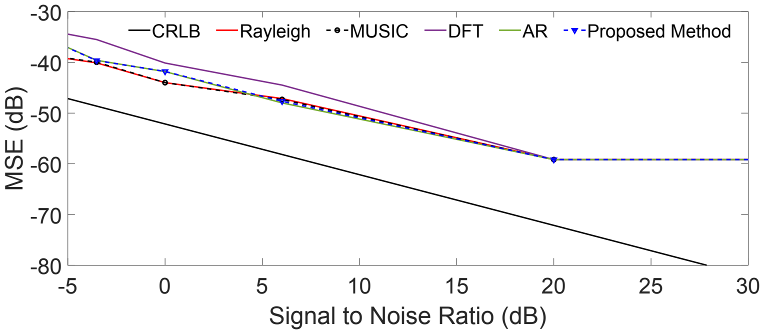

Figure 5.1: Mean squared error variation with the SNR. $N = 1000$

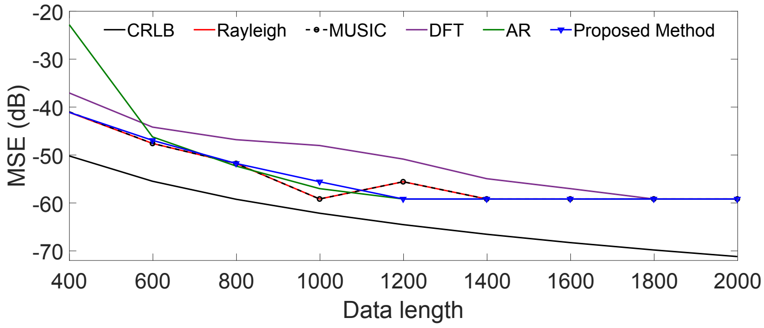

Figure 5.2: Mean squared error variation with data length. SNR = 6.98 dB.

(CRLB) for single-frequency estimation (derivation in Appendix C) is given as

$$\mathrm{var}(f) \geq \frac{3\sigma_v^2 F_s^2}{\pi^2 A_1^2 N(N-1)(2N-1)} \tag{5.15}$$

The MSE with different values of N is plotted in Fig. 5.2. For this simulation, a single component with a frequency of 51.11 Hz was taken. The SNR was fixed at 6.98 dB. It is observed that the MSE decreases with increasing data length for all the estimators. The MSE of all the estimators asymptotically converges to a constant value, after which N does not affect the MSE. It is also observed that the asymptotic value is achieved fastest by both the AR-spectrum and the proposed method. However, the proposed method performs better than the AR-spectrum when N is low.

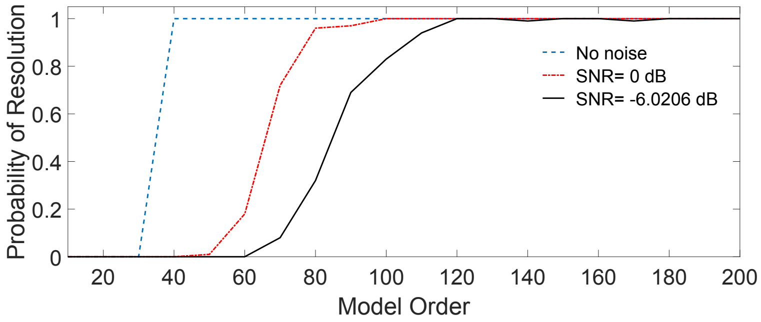

Figure 5.3: Variation of the probability of resolution of two sinusoidal components with different model-order.

For model-based methods, the resolution of the spectral estimation method depends on the model order p. The resolving power of the proposed spectral is evaluated using the probability of resolution. A signal with two components with a 1-Hz difference and unity amplitude is used to assess the probability of resolution. Three test conditions with different SNR levels are taken into account. For each value of p, 100 trials are conducted to find whether the components are resolved. Two components are resolved if (5.16) is satisfied.

$$\gamma(f_1, f_2) \triangleq h(f_\mu) - \frac{1}{2}\{h(f_1) + h(f_2)\} < 0 \tag{5.16}$$

where f_μ is the mean of f_1 and f_2, and $h(f_i)$ is the magnitude of the f_i^{th} component obtained from the spectrum. The probability of resolution for various model order is shown in Fig. 5.3.

5.5 Fault Detection using Bayesian MAP Spectrum

The implementation of the fault detection system, as illustrated in Fig. 5.4, is described as follows:

1. The current signal $x(n)$ is acquired at 400 samples/s with appropriate anti-

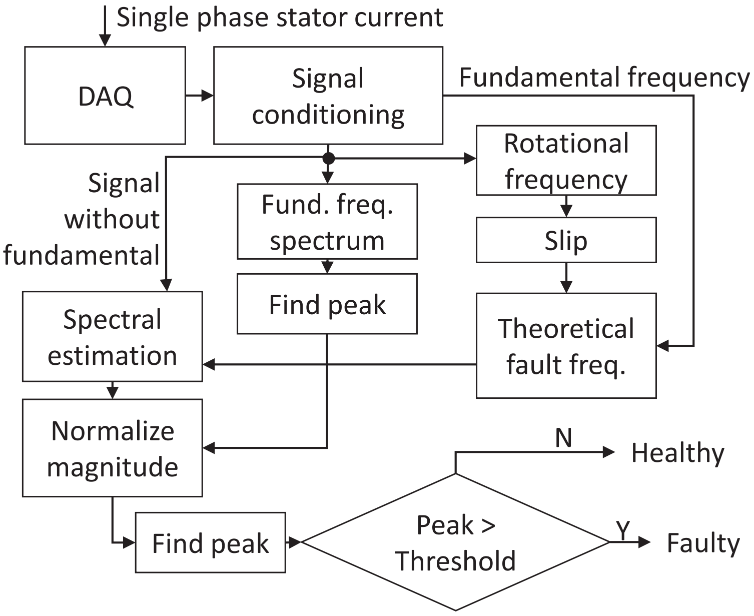

Figure 5.4: Implementation of the fault detection algorithm

alias filtering.

2. The signal conditioner estimates the fundamental frequency and removes the dominant components of $x(n)$. The conditioned signal $\hat{x}_0(n)$ is then stored in a buffer of length 2000. This amounts to five seconds of acquisition time.

3. The spectral estimator searches between $0.5f_0$ and $0.6f_0$ to find the mixed eccentricity peak component f_r.

4. The motor nameplate data, bearing specification, and f_r are then used to find the theoretical fault components.

5. A small band is searched around the theoretical frequencies by the spectral estimator, and the peak (ω) is detected.

6. The threshold (γ), buffered $\hat{x}_0(n)$, and ω are then sent for hypothesis testing, and the presence of fault is decided by the test statistic $T_0(x)$ and $T_1(x)$.

5.6 Results and Discussion: Fault Detection

5.6.1 Detection of Outer-raceway Fault

Figure 5.5 showed the stator current spectrum for a motor with an outer raceway fault when the motor was operated under low-load and high-load conditions. The fault-specific components can be easily distinguished when compared to a healthy motor spectrum.

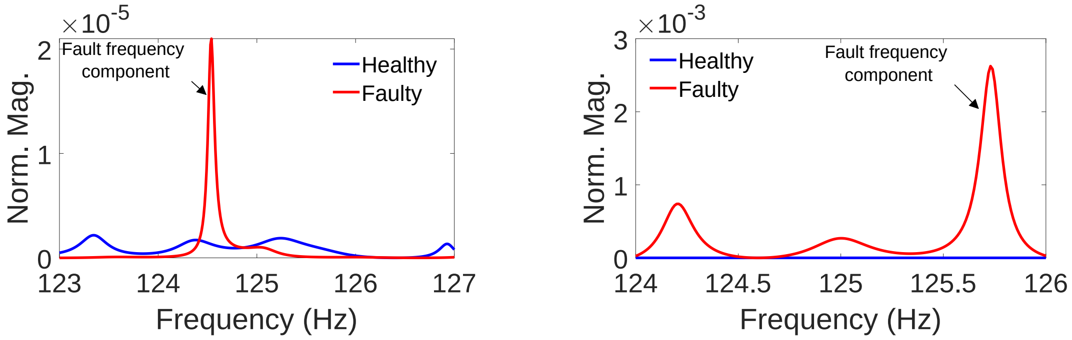

(a) Very low load, 0.2% slip.

(b) 67%load, 1.93% slip

Figure 5.5: Outer-race fault spectrum extracted from the stator current.

5.6.2 Detection of Inner-raceway Fault

In fig. 5.6, we have compared the spectrum of bearing with damaged inner raceway with a motor with healthy bearing. Two load cases are demonstrated in the figure. It is observed from the figure that the proposed method has successfully identified the faulty case for both the loads.

5.6.3 Detection of Rolling Element Fault

Conditioned stator current spectrum for the rolling element fault is shown in Fig. 5.7 for low-load and high-load, respectively. The fault component magnitude

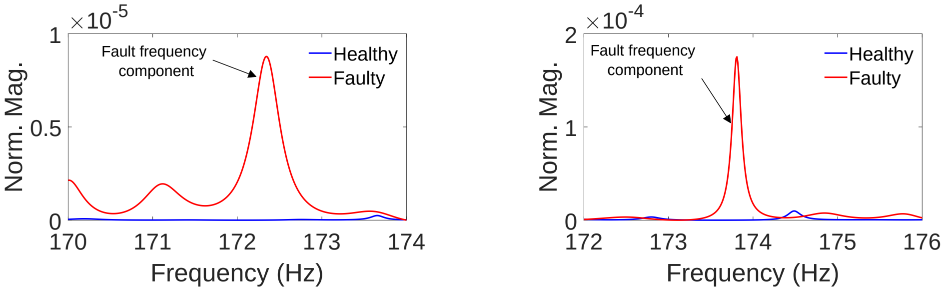

(a) Very low load, 0.2% slip.

(b) 67%load, 1.93% slip

Figure 5.6: Inner-race fault spectrum extracted from the current signal.

increases with increased loads and also gains prominence compared to the healthy spectrum.

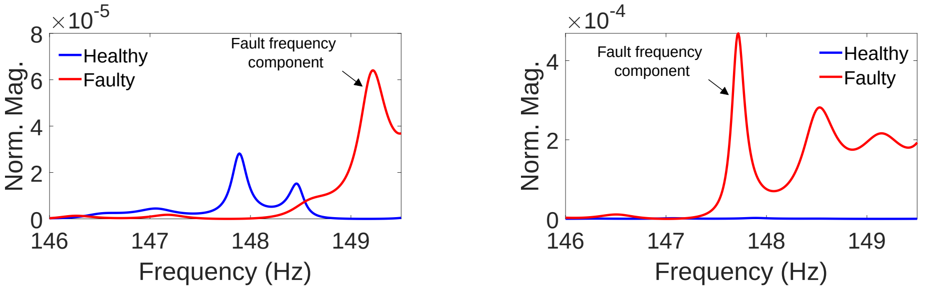

(a) Very low load, 0.2% slip.

(b) 67%load, 1.93% slip

Figure 5.7: Rolling element fault spectrum extracted from the current signal.

5.6.4 Detection of Cage Fault

The cage of the bearing was inadvertently damaged while machining the rolling element. Specific fault component was observed in the stator current spectrum, as shown in Fig. 5.8 for two load cases. The magnitude of the fault component decreases with increased loading. However, the fault component is distinguishable in both cases.

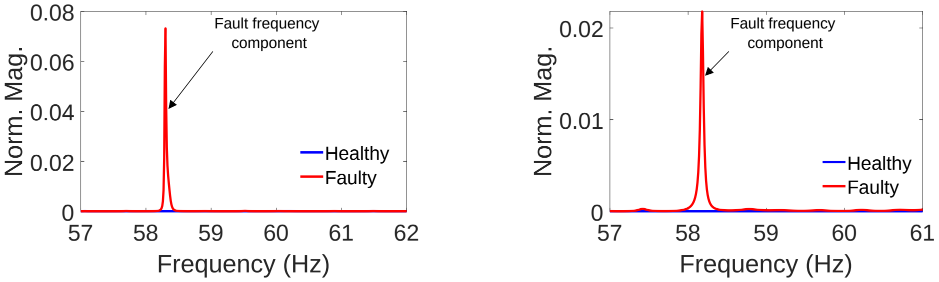

(a) Very low load, 0.2% slip.

(b) 67%load, 1.93% slip

Figure 5.8: Cage fault spectrum extracted from the current signal.

5.6.5 Detection of Single Broken Rotor Bar Fault

Figure 5.9 shows the spectrum of the stator current of the spectrum with a single broken rotor bar. Two conditions with low-load and high-load of 67% are shown in Fig. 5.9(a) and 5.9(b). The fault magnitude has increased with increased load, and the peak fault component magnitudes are higher than the healthy cases and are easily distinguishable.

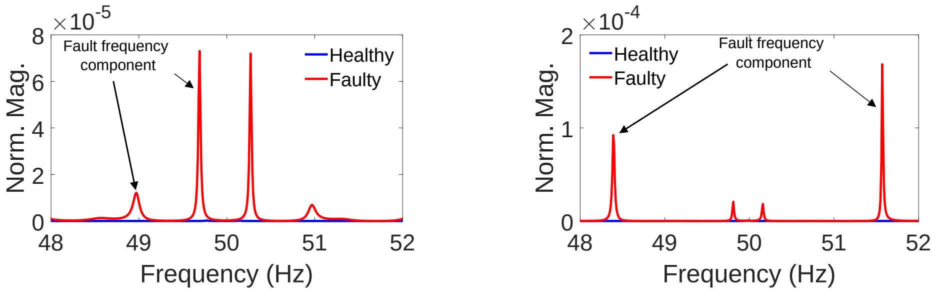

(a) Very low load, 0.2% slip.

(b) 67%load, 1.93% slip

Figure 5.9: Broken rotor bar fault spectrum extracted from the current signal.

5.7 Conclusions

The majority of the Bayesian spectral estimators assume a prior distribution of the frequency. However, we can improve the performance of the model-based spectral estimator by using a prior distribution on the parameters. This chapter has taken up the recent developments of TVAR-parameter estimates conditioned by the prior distribution for spectrum estimation. The assumed random walk model has also provided a way to estimate the spectrum sequentially. The resolution of parametric spectral estimators depends on the model order rather than on the data length. However, using a high-order model can result in spurious peaks in the spectrum. With the proposed spectral estimator, we have observed that these peaks are subdued, and accurate estimation of the frequency occurs with an increase in the number of observations. Thus, higher-order can improve the resolution, and longer data length can improve estimation accuracy. We have shown the effect of data length and SNR on the estimation error and compared the performance with four established methods. We have also evaluated the probability of resolution for different SNR levels and demonstrated the effect of model-order on the resolution. The spectral estimator needs further studies into its bias and variance to reduce the estimation error.

CHAPTER 6

Embedded System Development for Online Fault Detection

The fourth industrial revolution was ushered in with the capability of different components in the industry to connect themselves to a network. Connectivity enables remote monitoring and data storage of safety-critical equipment. In this chapter we will present two schemes for online implementations of the fault detector. The first scheme use the Rayleigh-quotient spectrum for detecting fault components. SIMULINK Real-Time (SLRT) was used for implementing the fault detection algorithm using an Intel embedded hardware. A single-phase stator current was recorded using NI-PCI 6024 E analog interface.

The second implementation uses the sequential Bayes spectrum of conditioned stator current for fault diagnosis. This framework is useful for monitoring multiple motors with IoT-enabled modules that can record and process stator current and transmit the decision to a central server for storing. We use local processing units to reduce large scale data transmission. Two ESP modules are configured as master-slave units to function as the data handler and fault detector, respectively. A sampling rate of 400 Hz is suitable for acquiring the data without aliasing for both the implementations, considering lower execution time.

Outline: The chapter is structured as follows: Section 6.1 describes the SLRT-based implementation of RQS estimator for fault detection. Section 6.2 presents the IoT-based fault detector that uses the Bayes MAP spectrum. This section includes the data communication protocols and fault detection framework for a multiple motor scenario. Section 6.3 summarizes and concludes the chapter.

6.1 SIMULINK Real-Time Implementation for a Standalone Fault Detection System

The complete fault detection algorithm has been realized on Intel-based embedded hardware for online and RT execution. The hardware consists of an ASUS Z87 mainboard with Intel Core i7 (3.4 GHz) processor, 8 GB DDR3 RAM, and NI PCI 6024E analog interface to acquire analog input signal from the motor. The embedded system is shown in Fig. 6.1a. The analog interface has a 12-bit resolution and supports up to 200 kHz sampling. DOS-based RT kernel known as SLRT developed by Mathworks is used as the operating system. A similar implementation for the detection of arc faults with SLRT can be found in [161]. SLRT is a host-target based system, where the fault detection program is developed on the host machine with SIMULINK and MATLAB. The host compiles the code and sends the executable to the target computer for RT execution. The NI PCI 6024E of the target acquires a single-phase stator current with 400 samples/s for 20 seconds. The received signal is conditioned using EKF, and a data matrix ($\mathbf{X}$) is created. The data matrix is used for spectral estimation and eventual fault evaluation. A screen-shot of the online system console is shown in Fig. 6.1b.

Table 6.1: Hardware specification of the SLRT system

Module	Name	Description
Current Sensor	Fluke i1010s (Hall effect)	AC input: 100 mA - 1000 A RMS, Frequency: 5 Hz - 100 kHz, Output: 1 mv/A, 10 mv/A, 100 mv/A.
Mainboard	Asus (Z87)	Processor: 3.4 GHz Intel Core i7, RAM: 8GB DDR3 (1600 MHz), PCI slots: 3xPCI, 2xPCIe(x16), Ethernet: 1xGigabit LAN Controller.
Analog Input Interface	NI PCI 6024E	Channels: 16 Single ended, 8 differential ended, Sampling frequency: 200 kHz (max), Resolution: 12 bit.

6.1.1 Implementation of the Rayleigh-Quotient Spectral Estimator

The Rayleigh-quotient spectral estimator can be formulated using simple matrix operations for implementation. This formulation is suitable for finding the spectral magnitudes in a single or multiple smaller frequency bands. The formulation involves a matrix multiplication followed by extraction of diagonal elements as given below

$$\hat{\boldsymbol{h}} = \tfrac{1}{L}\Big[\boldsymbol{W}^H \hat{\boldsymbol{R}}_x \boldsymbol{W}\Big]_{i,i} \quad i = 1, 2, \dots, m. \tag{6.1}$$

The diagonal vector of the matrix $(\boldsymbol{W}^H \hat{\boldsymbol{R}}_x \boldsymbol{W})$, contains the spectrum where the search is made. $\boldsymbol{W} = \begin{bmatrix} \boldsymbol{w}_1 & \boldsymbol{w}_2 & \dots & \boldsymbol{w}_m \end{bmatrix}^H$ is known as the search manifold matrix, and $\boldsymbol{w}_i$ is defined as

$$\boldsymbol{w}_i = \begin{bmatrix} 1 & e^{j\omega_i} & \dots & e^{j\omega_i(L-1)} \end{bmatrix}^H, \quad i = 1, 2, \dots, m,$$

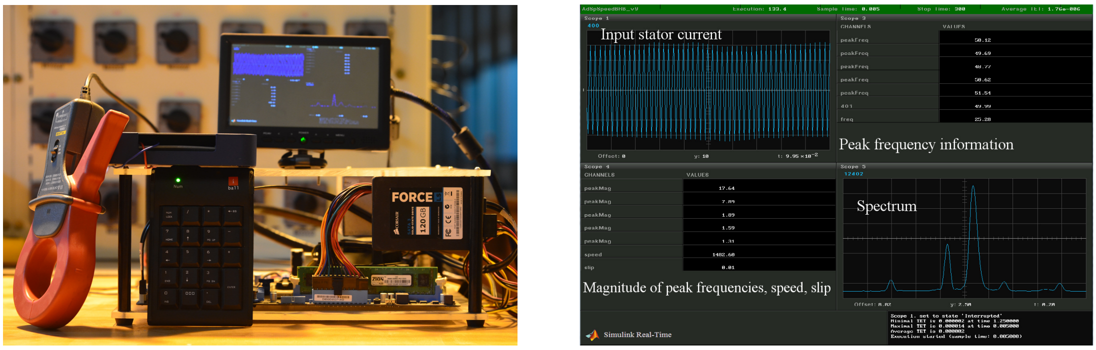

CHANNELS	VALUES
peakFreq	50.12
peakFreq	49.69
peakFreq	48.77
peakFreq	50.62
peakFreq	51.54
401	49.99
freq	25.28

CHANNELS	VALUES
peakMag	17.64
peakMag	7.89
peakMag	1.89
peakMag	1.59
peakMag	1.31
speed	1482.60
slip	0.01

```
Scope 1. set to state 'Interrupted'
Minimal TET is 0.000002 at time 1.250000
Maximal TET is 0.000014 at time 0.005000
Average TET is 0.000002
Execution started (sample time: 0.005000)
```

(a) Photograph of the developed fault detection system

(b) Online fault detector console

Figure 6.1: The online fault detection system and a screen-shot taken during a test run.

where $\omega_i \in [\omega_l, \omega_u]$ represents the normalized frequency band of m atoms where the search is done, and L is the size of the autocorrelation matrix $\hat{\boldsymbol{R}}_x$.

6.1.2 Implementation of the Online Fault Detector

The SIMULINK model for the online implementation of the fault detector is developed in accordance with the system described in Fig. 3.7. The working of the full system is given in Fig. 6.2

The fault detection is accomplished in two phases. The first stage is used for initialization and the second for execution. In the first phase, the motor parameters and variable dimensions are defined. The fixed dimensions of the variables avoids dynamic memory allocation. The initialization takes place in non-RT. The initialized parameters are required for slip estimation, supply frequency estimation, sampling time, spectral estimation, and time-steps. The execution phase estimates the amplitude of the fault specific frequency components. The stator current signal is acquired with the analog input card of NI PCI 6024E. The current data is used for slip and supply frequency estimation. The supply frequency estimator also conditions the input signal. The time of execution and the data

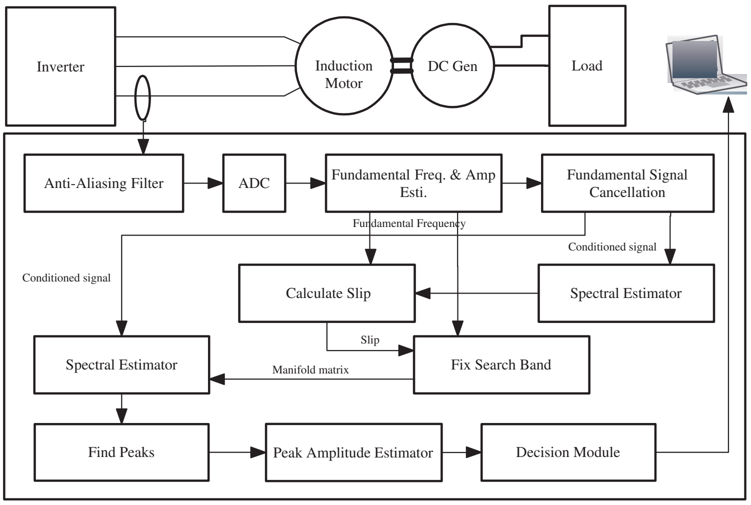

Figure 6.2: Fault detection scheme for SLRT implementation

acquisition sample time is same till spectral estimation, and the execution is performed in RT. Buffers are used for storing frames of conditioned data. The spectral estimator executes with a slower execution time and operates over the frame. The SIMULINK implementation of the fault detector is shown in Fig. 6.3. The data processing steps are enumerated as

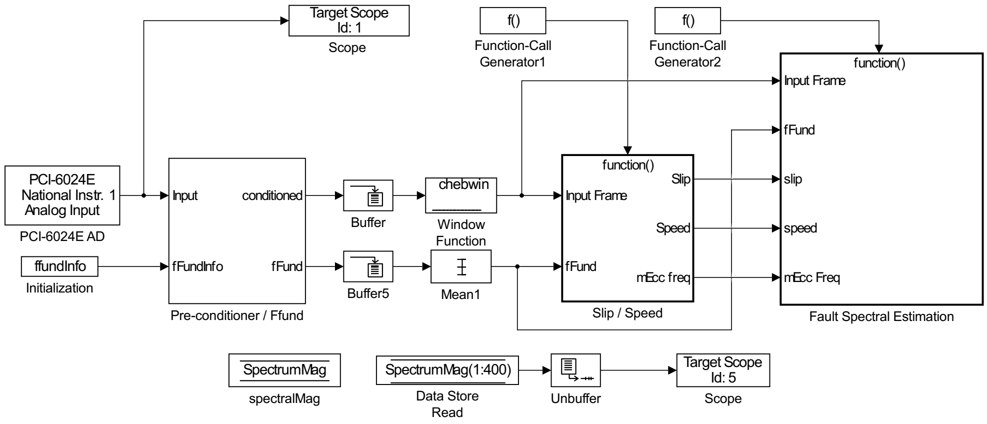

Figure 6.3: Implementation of the fault detector in SIMULINK for SLRT.

i. The stator current is acquired with 400 samples/s. For detecting only BRB, a sampling rate of 200 samples/s is adequate.

ii. The acquired data is used for supply frequency estimation and signal conditioning.

iii. A block estimates the slip according to (3.19).

iv. Different buffers store the conditioned data, slip, and fundamental frequency. The data frames are then sent for further processing.

v. For a particular frame of stator current, the mean values of fundamental frequency, and the slip are used for fixing the search band for spectral estimation.

vi. Autocorrelation matrix is constructed from the data frame.

vii. Multiple search bands corresponding to each fault are defined using supply frequency and slip values.

viii. Spectral estimation is conducted for each frame.

ix. Normalized magnitude of the spectral peaks are determined and used for decision.

6.2 Internet of Things Implementation for Multiple Motor Monitoring

There are two significant realms involved in Internet of things (IoT)-based remote monitoring. The first method relies on local resources for the acquisition and communication of data [162]. The central-server handles the processing. However, to reduce the intensive data-rate and error-prone nature of the former process, in-situ processing of the raw data and sending the diagnostic parameters to a central-server form the second paradigm [163]. This section showcases an IoT-based framework for detecting faults of squirrel cage induction motors. In this approach, each motor is provided with a detector unit that can acquire motor signals and process them to detect faults. We have considered a single broken rotor bar and defects in different parts of the bearing like inner-race, outer-race, rolling-element, and cage. The detector is provisioned to store fault information into a central server, accessed by a registered user.

6.2.1 The IoT Architecture

The architecture of the IoT system consists of three major parts, (i) The central server, (ii) Client: User, and (iii) Client: Detector, as shown in Fig. 6.4. The central server acts as a bridge between the user and detector. The user can request the server and observe the status of a motor using the HTTP protocol. Each motor is connected to a detector unit, which processes motor parameters and sends fault status to the server. The server is run on Python 3 and can handle GET and POST requests from the user and the detector.

The detector consists of two ESP modules that operate in a master-slave configuration. The master unit uses an ESP-8266 module to communicate with the central server and controls the slave unit using serial communication. The slave uses an ESP-32 Wrover, having two cores. The core 0 of the slave unit generates a clock pulse for driving IC MAX280- a fifth-order, low-pass Butterworth filter. Core 1 is used for data acquisition and fault detection. The detector is implemented using embedded C++ in the Arduino IDE. The description of the different hardware components are provided in Table 6.2.

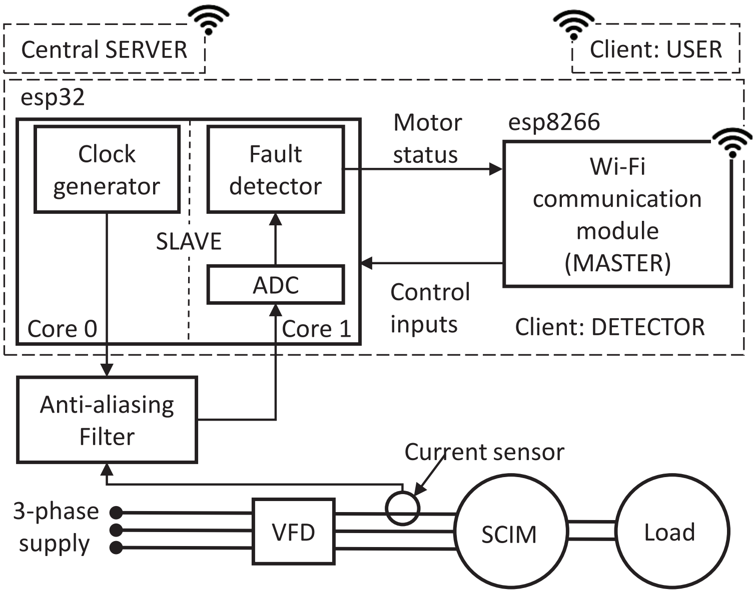

Figure 6.4: Schematic block diagram of the IoT-based implementation

6.2.2 Data Communication and Fault Detection

i. The user sends an HTTP GET request to register the motor using the serial number and then an HTTP PUSH request to send a user-info file in the server in JavaScript object notation (JSON) format for the first time only. The user-info file contains the nameplate motor and bearings specifications in the following form:

$$“user - info” : \{“P_1” : “ < val > ”, “P_2” : “ < val > ”, \ldots, \}$$

where P_i are the input parameters having unique names and their corresponding values.

ii. The detector sends an HTTP GET request to the server with basic authentication and motor serial number as a user-agent header to receive the user-info file only once. If the file is not found, i.e., the user has not registered the motor, the detector gets the GET response 404.

Table 6.2: Hardware specification of the IoT system

Module	Name	Description
Current sensor	SCT013-000 (Current transformer type)	AC input: 0-100 A, output: 0-50 mA,
Anti-aliasing filter	IC MAX280	5th-order, zero-error, Butterworth, switched-capacitor low-pass filter, cutoff frequency: 20 kHz (max)
Master unit	ESP32-WROVER-B	Flash: 4 MB, PSRAM: 4 MB, clock: 160 MHz, operating voltage: 2.7 - 3.6 v, SRAM: 520 KB, ADC resolution: 12 bit
Slave unit	ESP8266	RAM: 512 KB, clock: 80 MHz, configured baud rate: 115200, Wi-Fi: IEEE 802.11 b/g/n

iii. The master unit sends the received user-info file to the slave unit for its storage in the flash memory. Every master unit is hard-coded with an identifier same as the serial number of the motor. The identifier serves as the unique identity of the detector to communicate with the server. The master unit uses network time protocol over the UDP socket to get time and date-stamps and triggers the slave through serial communication for fault detection. The user fixes the time interval of the trigger.

iv. The slave unit stores the received user-info as a JSON file using the serial peripheral interface flash file system (SPIFFS).

v. After passing the current signal through the anti-aliasing filter, it is digitized and stored using the 12-bit analog to digital converter of the slave module. The sampling rate of 2 kHz has been used. However, the signal is down-sampled to 400 Hz for the present application for better spectral resolution.

The built-in pseudo-RAM of the slave unit provides extra memory for storing the current time samples.

vi. The stored samples are processed by the slave, and the output is serially sent to the master unit in the following format:

$$\{\text{“}Freq\text{”} : \{\text{“}f_1\text{”} : \text{“} < val > \text{”}, \text{“}f_2\text{”} : \text{“} < val > \text{”}, \ldots\}$$

$$\{\text{“}Amp\text{”} : \{\text{‘}a_1\text{”} : \text{“} < val > \text{”}, \text{“}a_2\text{”} : \text{“} < val > \text{”}, \ldots\}$$

where f_i and a_i are the names of specific frequencies and amplitudes along with their values val.

vii. The master sends a POST request with the motor serial number in the user-agent header and data-time stamp with the basic authentication header. A file containing the frequency and amplitude information are sent to the server for its appropriate storage as

$$< motor\_identifier > / < data >< time > .JSON.$$

6.3 Conclusions

This chapter presents two schemes for the online fault detection. The SLRT based hardware platform was developed for analyzing a single motor. Single-phase stator current is acquired for fault detection. For the SLRT-based implementation, the Rayleigh-quotient spectrum is used for fault detection. However, for sequential and RT applications, the Bayesian spectral estimation is used in the IoT-based system. The IoT-based system is suitable for detecting faults of multiple motors and can be used for future studies with historical fault analysis.

CHAPTER 7

Conclusions and Future Research Directions

This thesis tackles the problem of detection and estimation of low-amplitude frequency components buried under noise and masked by the presence of high-magnitude components. The associated phase information has been used to remove multiple dominant components, which has further improved the detection of the minor components. We have used the framework for detecting incipient faults in squirrel cage induction motors.

In Chapter 2, we have investigated the IF estimation of multiple components simultaneously. We have proposed an analytic form of a linearized observation model and used a constrained Kalman filter for the sequential analysis. Analytic closed-form matrices have substituted the dynamic linearization of the observation for general model-order and higher accuracy. The estimator is suitable for estimating closely-spaced frequency components or components having sharp changes in the frequency. The recovery time in case of the abrupt transition is better than other state-of-the-art methods. We have also observed that the technique outperforms other methods while estimating the frequency with a higher chirp-rate. The performance of the proposed method under high-SNR is proficient. However, its performance in low-SNR condition needs improvement. Three real-world examples to demonstrate the applicability and superiority of the proposed method under unknown SNR levels. The technique has the advantage of using a model in addition to the data for better performance.

In Chapter 3, the theory of the Rayleigh quotient was utilized for designing the proposed spectral estimator. We observed the performance of the spectral estimator for estimating frequency components to be better than DFT and is similar to that of MUSIC. Additionally, it can find the amplitude of the fault components and is also faster, unlike MUSIC. This chapter uses an EKF-based signal conditioner for eliminating the fundamental supply frequency of a single-phase stator current input. The conditioning had enhanced the signatures of a partially broken bar fault under light load conditions. However, the detection of multiple defects requires removing multiple dominant components. Significantly, the harmonics of the rotational frequency are quite overwhelming when compared to the low-amplitude fault components.

Hence, the mode-extraction property of the IF estimator of Chapter 2 was used for the targeted removal of multiple dominant components in chapter 4. The Rayleigh-spectrum was also extended for detecting different incipient faults of the SCIM using a single vibration sensor. This chapter has also proposed a minimum distance-based detector for incorporating incipient and inherent fault condition information into the decision process for reducing false alarms under noisy conditions. The proposed method is advantageous over recently proposed data-driven and DL-based methods due to its high-accuracy and non-requirement of faulty-motor data for the training. The technique only requires a few instances of healthy-motor data for fixing the threshold.

Chapter 5 proposes a Bayesian MAP-based method for spectral estimation using a first-order generalized Gauss-Markov random walk as the prior distribution of the states. The Gauss-Markov process solves a regularized least-squares problem and aids in the sequential estimation of the spectrum. We presented two embedded system implementation for fault detection in Chapter 6. The first example uses a SIMULINK-based framework for implementing the RQS estimator for detecting the faults. The second example uses the Bayes MAP estimator for a portable and IoT-based implementation. The first method is useful for a single motor. Whereas, the IoT-based method is suitable for a multi-motor scenario.

7.1 Future Scope of Reserch

The thesis leaves ample scope of extension for different applcations where frequency estimation can be useful. Few research avenues are discussed below:

i. *High-resolution spectral imaging:* Scanning macro X-ray fluorescence (MA-XRF) imaging is used for deconvolving hidden images of old art-works by tracing element spectroscopy. An X-ray beam is used to scan the whole image, and spectral information from each pixel are used to decipher the presence of different elements. There are two associated problems that can be an extension of this thesis. Particularly the use of spectral estimation to for high resolution traces and use of signal conditioning to remove the effect of spectral leakage. Especially, while estimating the presence of minor elements.

ii. *Load characterization and deconvolving its effect from fault features:* The experimental setup was mainly used for detecting faults under constant loading. However, in real life, the motors have to operate under load-torque oscillations. The provision of using a simplified motor model to estimate and remove the load-torque oscillation can make the proposed alogorithms robust in an industrial setting.

iii. *Use of spatial motor data and Graph-based detection of faults:* In a industry, multiple motors are used for executing a task in co-operation. For example, there are four to six traction motors that drive a locomotive engine. Similarly, in an steel rolling inustry, multiple motors are used for processing the steel. In such a scenario, a graph-signal processing architecture can be used to study the effect of differential load and fault in one motor on the overall operation of the plant.

iv. *Deep learning and its generalizability:* The recent use of deep learning has influenced the field of fault detction immensely. However, there are few problems that arise due to the absence of multiple datasets and training scenarios covering the whole spectrum of motor operation. More emphasis should be laid on how the developed models can be used for motors having no fault-data using exsting trained models.

Appendices

APPENDIX A

Experimental Setup Specification

A.1 SCIM specification

Three-phase, four-pole squirrel cage induction motor (ABB), delta connection with 28 rotor bars. Rated characteristics: power = 22 kW, voltage = 415 V, current = 40.5 A , speed = 1460 rpm, frequency = 50 Hz.

A.2 Laboratory bearing specification

Model: SKF 6310-2ZR with $N_b = 8$ units, $b_d = 19.05$ mm, $d_\rho = 82$ mm, $\beta = 0$.

A.3 CWRU bearing specification

Model: SKF 6205-2RS with $N_b = 9$ units, $b_d = 7.94$ mm, $d_\rho = 39.0398$ mm, $\beta = 0$.

A.4 Offline system specification

HP Z420 workstation with 2.80 GHz Intel Xeon CPU E5-1603 processor, 16 GB RAM, 64-bit Windows 10 operating system, and MATLAB R2019b is used.

A.5 Data acquisition specification

Make: Yokogawa DL 850E, ADC Resolution: 16 Bit, Sampling rate: 20 kHz (max: 100 MHz), Channel: 16 (Type: current, voltage, vibration, acoustic), Connectivity/ Data Storage: Ethernet connected to desktop for data transmission storage, Anti-aliasing filter: Low pass analog filter 4 kHz cut-off frequency.

APPENDIX **B**

Derivation of $\boldsymbol{H}[n]$

Expanding (2.10), we have

$$\begin{aligned} h\left(\boldsymbol{\theta}[n]\right) = &(e^{j\omega_1[n]} + \cdots + e^{j\omega_p[n]})x[n-1] - \\ &(e^{j\omega_1[n]}e^{j\omega_2[n]} + \cdots + e^{j\omega_{p-1}[n]}e^{j\omega_p[n]})x[n-2] + \\ &\cdots (-1)^{p+1}\left(e^{j\omega_1[n]}\cdots e^{j\omega_p[n]}\right)x[n-p]. \end{aligned}$$

Now, $\boldsymbol{H}[n]$ is given by

$$\boldsymbol{H}[n] = \frac{\partial h(\boldsymbol{\theta}[n])}{\partial(\boldsymbol{\theta}[n])} = \left[\begin{array}{ccc} \frac{\partial h(\boldsymbol{\theta}[n])}{\partial \omega_1[n]} & \cdots & \frac{\partial h(\boldsymbol{\theta}[n])}{\partial \omega_p[n]} \end{array}\right]$$

Therefore, the k^{th} element of $\boldsymbol{H}[n]$ can be obtained as

$$\begin{aligned} \frac{\partial h(\boldsymbol{\theta}[n])}{\partial \omega_k[n]} = &je^{j\omega_k[n]}x[n-1] - j(e^{j\omega_1[n]}e^{j\omega_k[n]} + \cdots + e^{j\omega_p[n]}e^{j\omega_k[n]})x[n-2] + \\ &\cdots j(-1)^{p+1}\left(e^{j\omega_1[n]}\cdots e^{j\omega_p[n]}\right)x[n-p] \end{aligned}$$

$$= je^{j\omega_k[n]}\left[\begin{array}{cccc} 1 & -\sum_{i=1,i\neq k}^{p} e^{j\omega_i[n]} & \cdots & (-1)^{p+1}\prod_{i=1,i\neq k}^{p} e^{j\omega_i[n]} \end{array}\right]\boldsymbol{x}[n-1]$$

Hence,

$$\boldsymbol{H}^T[n] =$$

$$j\begin{bmatrix} e^{j\omega_1[n]} & \cdots & 0 \\ \vdots & \ddots & \vdots \\ 0 & \cdots & e^{j\omega_p[n]} \end{bmatrix}\begin{bmatrix} 1 & -\sum\limits_{i=2}^{p} e^{j\omega_i[n]} & \cdots & (-1)^{p+1}\prod\limits_{i=2}^{p} e^{j\omega_i[n]} \\ \vdots & \vdots & \ddots & \vdots \\ 1 & -\sum\limits_{i=1}^{p-1} e^{j\omega_i[n]} & \cdots & (-1)^{p+1}\prod\limits_{i=1}^{p-1} e^{j\omega_i[n]} \end{bmatrix}\boldsymbol{x}[n-1]$$

alternatively, $\boldsymbol{H}^T[\boldsymbol{n}] = \boldsymbol{\phi W x}[\boldsymbol{n}-\mathbf{1}]$**.**

APPENDIX **C**

Derivation of Cramer Rao Bound

The real signal model is given by

$$x[n] = A\cos\left(\frac{2\pi f}{F_s}n + \phi\right) + w[n] \tag{C.1}$$

where A, f, ϕ are the amplitude, frequency and phase of a single sinusoid respectively. F_s is the sampling frequency and $w[n]$ is the white additive gaussian noise. The probability density function of $x_0, x_1, \ldots, x_{N-1}$ represented by $\mathbf{x}$ and parameterized by f is given by

$$P_{\mathbf{x}}(\mathbf{x}; f) = \frac{1}{\left(2\pi\sigma^2\right)^{N/2}} \exp\left\{-\frac{1}{2\sigma^2}\sum_{n=0}^{N-1}\left[x(n) - A\cos\left(\frac{2\pi f}{F_s}n + \phi\right)\right]^2\right\} \tag{C.2}$$

Taking natural logarithm on both side gives

$$\ln p_{\mathbf{x}}(\mathbf{x}; f) = -\frac{N}{2}\ln\left(2\pi\sigma^2\right) - \frac{1}{2\sigma^2}\sum_{n=0}^{N-1}\left[x(n) - A\cos\left(\frac{2\pi f}{F_s}n + \phi\right)\right]^2 \tag{C.3}$$

The first derivative w.r.t to f is given by

$$\frac{\partial \ln p_{\mathbf{x}}(\mathbf{x};f)}{\partial f} = -\frac{2\pi A}{\sigma^2 F_s}\sum_{n=0}^{N-1} n\left[x(n) - A\cos\left(\frac{2\pi f}{F_s}n+\phi\right)\right]\sin\left(\frac{2\pi f}{F_s}n+\phi\right) \tag{C.4}$$

$$= -\frac{2\pi A}{\sigma^2 F_s}\sum_{n=0}^{N-1} n\left[x(n)\sin\left(\frac{2\pi f}{F_s}n+\phi\right) - \frac{A}{2}\sin\left(\frac{4\pi f}{F_s}n+2\phi\right)\right] \tag{C.5}$$

The second derivative w.r.t to f is given by

$$\frac{\partial^2 \ln p_{\mathbf{x}}(\mathbf{x};f)}{\partial f^2} = -\frac{2\pi A}{\sigma^2 F_s}\sum_{n=0}^{N-1} n\left[\frac{2\pi}{F_s}nx(n)cos\left(\frac{2\pi f}{F_s}n+\phi\right) - \frac{2\pi A}{F_s}n\cos\left(\frac{4\pi f}{F_s}n+2\phi\right)\right] \tag{C.6}$$

Putting the value of $x[n]$ from (C.1) in the above equation, we get

$$\frac{\partial^2 \ln p_{\mathbf{x}}(\mathbf{x};f)}{\partial f^2} = -\frac{2\pi A}{\sigma^2 F_s}\sum_{n=0}^{N-1} n\left[\frac{2\pi}{F_s}n\left\{A\cos^2\left(\frac{2\pi f}{F_s}n+\phi\right) + w[n]cos\left(\frac{2\pi f}{F_s}n+\phi\right)\right\} - \frac{2\pi A}{F_s}n\cos\left(\frac{4\pi f}{F_s}n+2\phi\right)\right] \tag{C.7}$$

Taking negative expectation on both sides we get

$$-\mathcal{E}\frac{\partial^2 \ln p_{\mathbf{x}}(\mathbf{x};f)}{\partial f^2} = \frac{2\pi A}{\sigma^2 F_s}\mathcal{E}\sum_{n=0}^{N-1} n\left[\frac{2\pi}{F_s}nA\cos^2\left(\frac{2\pi f}{F_s}n+\phi\right)\right] \tag{C.8}$$

It is to be noted that

$$\sum_{n=0}^{N-1} n\mathcal{E}\left[w[n]cos\left(\frac{2\pi f}{F_s}n+\phi\right)\right] \approx 0$$

as $w[n]$ and ϕ are independent,

$$\sum_{n=0}^{N-1} n^2 \mathcal{E}\left[\cos\left(\frac{4\pi f}{F_s}n + 2\phi\right)\right] \approx 0$$

and

$$\sum_{n=0}^{N-1} n^2 \mathcal{E}\left[\cos^2\left(\frac{2\pi f}{F_s}n + \phi\right)\right] = \sum_{n=0}^{N-1} \frac{n^2}{2}$$

Therefore from (C.8) we have

$$-\mathcal{E}\frac{\partial^2 \ln P_{\boldsymbol{x}}(\boldsymbol{x}; f)}{\partial f^2} = \frac{4\pi^2 A^2}{\sigma^2 F_s^2} \sum_{n=0}^{N-1} n^2 \mathcal{E}\left[\cos^2\left(\frac{2\pi f}{F_s}n + \phi\right)\right]$$

$$= \frac{4\pi^2 A^2}{\sigma^2 F_s^2} \sum_{n=0}^{N-1} \frac{n^2}{2} = \frac{2\pi^2 A^2}{\sigma^2 F_s^2} \sum_{n=0}^{N-1} n^2 = \frac{2\pi^2 A^2}{\sigma^2 F_s^2} \frac{N(N-1)(2N-1)}{6} \tag{C.9}$$

The CRB is found by

$$\operatorname{var}(f) \geq \frac{1}{-E\left\{\frac{\partial^2 \ln P_{\boldsymbol{x}}(\boldsymbol{x};f)}{\partial f^2}\right\}}$$

Hence using the above identity in (C.9) gives

$$\operatorname{var}(f) \geq \frac{3\sigma^2 F_s^2}{\pi^2 A^2 N(N-1)(2N-1)} \tag{C.10}$$

Bibliography

[1] "Scopus Document Search." [Online]. Available: https://www.scopus.com/search/form.uri?display=basic

[2] Y. I. Abramovich, N. K. Spencer, and M. D. E. Turley, "Time-varying Autoregressive TVAR Adaptive Order and Spectrum Estimation," *Conf. Signals, Syst. Comput.*, no. 7, pp. 89–93, 2005.

[3] S. Kay, "A new nonstationarity detector," *IEEE Transa. Signal Process.*, vol. 56, no. 4, pp. 1440–1451, 2008.

[4] D. Rudoy, T. F. Quatieri, and P. J. Wolfe, "Time-Varying Autoregressions in Speech: Detection Theory and Applications," *IEEE Trans. Audio, Speech, Lang. Process.*, vol. 19, no. 4, pp. 977–989, 2009.

[5] Y. Chu and C. M. Mak, "A New Parametric Adaptive Nonstationarity Detector and Application," *IEEE Trans. Signal Process.*, vol. 65, no. 19, pp. 5203–5214, 2017.

[6] T. Chau, D. Chau, M. Casas, G. Berall, and D. J. Kenny, "Investigating the stationarity of paediatric aspiration signals," *IEEE Trans. Neural Syst. Rehabil. Eng.*, vol. 13, no. 1, pp. 99–105, 2005.

[7] S. M. Kay, *Modern spectral estimation.* Pearson Education India, 1988.

[8] R. Schmidt, "Multiple emitter location and signal parameter estimation," *IEEE Trans. Antennas Propag.*, vol. 34, no. 3, pp. 276–280, 1986.

[9] R. Roy and T. Kailath, "ESPRIT-estimation of signal parameters via rotational invariance techniques," *IEEE Trans. Audio, Speech, Lang. Process.*, vol. 37, no. 7, pp. 984–995, 1989.

[10] F. Hlawatsch and F. Auger, *Time-frequency analysis.* John Wiley & Sons, 2013.

[11] S. Kortlang, G. Grimm, V. Hohmann, B. Kollmeier, and S. D. Ewert, "Auditory model-based dynamic compression controlled by subband instantaneous frequency and speech presence probability estimates," *IEEE/ACM Trans. Audio, Speech, Lang. Process.*, vol. 24, no. 10, pp. 1759–1772, 2016.

[12] C. I. Chen, G. W. Chang, R. C. Hong, and H. M. Li, “Extended real model of Kalman filter for time-varying harmonics estimation,” *IEEE Trans. Power Del.*, vol. 25, no. 1, pp. 17–26, 2010.

[13] M. Lozano, J. A. Fiz, and R. Jané, “Automatic differentiation of normal and continuous adventitious respiratory sounds using ensemble empirical mode decomposition and instantaneous frequency,” *IEEE J. Biomed. Heal. Inform.*, vol. 20, no. 2, pp. 486–497, 2016.

[14] S. Wang, X. Chen, I. W. Selesnick, Y. Guo, C. Tong, and X. Zhang, “Matching synchrosqueezing transform: A useful tool for characterizing signals with fast varying instantaneous frequency and application to machine fault diagnosis,” *Mech. Syst. Signal Process.*, vol. 100, pp. 242–288, 2018.

[15] “Case Western Reserve University Bearing Data Center.” [Online]. Available: http://csegroups.case.edu/bearingdatacenter/home

[16] A. K. Samanta, A. Naha, A. Routray, and A. K. Deb, “Fast and accurate spectral estimation for online detection of partial broken bar in induction motors,” *Mech. Syst. Signal Process.*, vol. 98, pp. 63–77, 2018.

[17] S. V. Tenneti and P. P. Vaidyanathan, “iMUSIC: A Family of MUSIC-Like Algorithms for Integer Period Estimation,” *IEEE Trans. Signal Process.*, vol. 67, no. 2, pp. 367–382, 2019.

[18] K. V. Rangarao and S. Venkatanarasimhan, “Gold-MUSIC: A Variation on MUSIC to Accurately Determine Peaks of the Spectrum,” *IEEE Trans. Antennas Propag.*, vol. 61, no. 4, pp. 2263–2268, 2013.

[19] M. Trinh-Hoang, M. Viberg, and M. Pesavento, “Partial Relaxation Approach: An Eigenvalue-Based DOA Estimator Framework,” *IEEE Trans. Signal Process.*, vol. 66, no. 23, pp. 6190–6203, 2018.

[20] M. W. Morency, S. A. Vorobyov, and G. Leus, “Joint Detection and Localization of an Unknown Number of Sources Using the Algebraic Structure of the Noise Subspace,” *IEEE Trans. Signal Process.*, vol. 66, no. 17, pp. 4685–4700, 2018.

[21] T. L. Hansen, B. H. Fleury, and B. D. Rao, “Superfast Line Spectral Estimation,” *IEEE Trans. Signal Process.*, vol. 66, no. 10, pp. 2511–2526, 2018.

[22] G. Kitagawa and W. Gersch, “A Smoothness Priors Long AR Model Method for Spectral Estimation,” *IEEE Trans. Autom. Control*, vol. 30, no. 1, pp. 57–65, 1985.

[23] P. M. Djuric and H.-T. Li, “Bayesian spectrum estimation of harmonic signals,” *IEEE Signal Process. Lett.*, vol. 2, no. 11, pp. 213–215, 1995.

[24] H. Fu and P. Y. Kam, “MAP/ML Estimation of the Frequency and Phase of a Single Sinusoid in Noise,” *IEEE Trans. Signal Process.*, vol. 55, no. 3, pp. 834–845, 2007.

[25] L. Zhao, L. Wang, G. Bi, L. Zhang, and H. Zhang, "Robust Frequency-hopping Spectrum Estimation based on Sparse Bayesian Method," *IEEE Wirel. Commun. Lett.*, vol. 14, no. 2, pp. 781–793, 2015.

[26] M.-A. Badiu, T. L. Hansen, and B. H. Fleury, "Variational Bayesian Inference of Line Spectra," *IEEE Trans. Signal Process.*, vol. 65, no. 9, pp. 2247–2261, 2017.

[27] P. Das and B. Babadi, "Dynamic Bayesian Multitaper Spectral Analysis," *IEEE Trans. Signal Process.*, vol. 66, no. 6, pp. 1394–1409, 2018.

[28] F. Auger, P. Flandrin, Y.-T. Lin, S. McLaughlin, S. Meignen, T. Oberlin, and H.-T. Wu, "Time-frequency reassignment and synchrosqueezing: An overview," *IEEE Signal Process. Mag.*, vol. 30, no. 6, pp. 32–41, 2013.

[29] V. Popović-Bugarin and S. Djukanović, "Efficient instantaneous frequency estimation in high noise based on the Wigner distribution," *Signal Process.*, vol. 157, pp. 25–29, 2019.

[30] R. Tao, Y.-L. Li, and Y. Wang, "Short-time fractional Fourier transform and its applications," *IEEE Trans. Signal Process.*, vol. 58, no. 5, pp. 2568–2580, 2010.

[31] N. A. Khan and B. Boashash, "Instantaneous frequency estimation of multicomponent nonstationary signals using multiview time-frequency distributions based on the adaptive fractional spectrogram," *IEEE Signal Process. Lett.*, vol. 20, no. 2, pp. 157–160, 2013.

[32] F. Auger and P. Flandrin, "Improving the readability of time-frequency and time-scale representations by the reassignment method," *IEEE Trans. Signal Process.*, vol. 43, no. 5, pp. 1068–1089, 1995.

[33] G. Thakur, E. Brevdo, N. S. Fučkar, and H.-T. Wu, "The synchrosqueezing algorithm for time-varying spectral analysis: Robustness properties and new paleoclimate applications," *Signal Process.*, vol. 93, no. 5, pp. 1079–1094, 2013.

[34] I. Daubechies, J. Lu, and H.-T. Wu, "Synchrosqueezed wavelet transforms: An empirical mode decomposition-like tool," *Appl. Comput. Harmon. Anal.*, vol. 30, no. 2, pp. 243–261, 2011.

[35] T. Oberlin, S. Meignen, and V. Perrier, "Second-Order Synchrosqueezing Transform or Invertible Reassignment? Towards Ideal Time-Frequency Representations." *IEEE Trans. Signal Process.*, vol. 63, no. 5, pp. 1335–1344, 2015.

[36] D. H. Pham and S. Meignen, "High-Order Synchrosqueezing Transform for Multicomponent Signals Analysis-With an Application to Gravitational-Wave Signal." *IEEE Trans. Signal Process.*, vol. 65, no. 12, pp. 3168–3178, 2017.

[37] S. Wang, X. Chen, G. Cai, B. Chen, X. Li, and Z. He, "Matching demodulation transform and synchrosqueezing in time-frequency analysis," *IEEE Trans. Signal Process.*, vol. 62, no. 1, pp. 69–84, 2014.

[38] Y. Yang, X. Dong, Z. Peng, W. Zhang, and G. Meng, “Component extraction for non-stationary multi-component signal using parameterized de-chirping and band-pass filter,” *IEEE Signal Process. Lett.*, vol. 22, no. 9, pp. 1373–1377, 2015.

[39] T. L. Jensen, J. K. Nielsen, J. R. Jensen, M. G. Christensen, and S. H. Jensen, “A Fast Algorithm for Maximum-Likelihood Estimation of Harmonic Chirp Parameters,” *IEEE Trans. Signal Process.*, vol. 65, no. 19, pp. 5137–5152, 2017.

[40] I. Djurović, “A WD-RANSAC instantaneous frequency estimator,” *IEEE Signal Process. Lett.*, vol. 23, no. 5, pp. 757–761, 2016.

[41] ——, “QML-RANSAC Instantaneous Frequency Estimator for Overlapping Multicomponent Signals in the Time-Frequency Plane,” *IEEE Signal Process. Lett.*, vol. 25, no. 3, pp. 447–451, 2018.

[42] M. Aboy, O. W. Márquez, J. Mcnames, and R. Hornero, “Adaptive Modeling and Spectral Estimation of Nonstationary Biomedical Signals Based on Kalman Filtering,” *IEEE Trans. Biomed. Eng.*, vol. 52, no. 8, pp. 1485–1489, 2005.

[43] M. E. Khan and D. N. Dutt, “An expectation-maximization algorithm based Kalman smoother approach for event-related desynchronization (ERD) estimation from EEG,” *IEEE Trans. Biomed. Eng.*, vol. 54, no. 7, pp. 1191–1198, 2007.

[44] A. Routray, A. K. Pradhan, and K. P. Rao, “A novel Kalman filter for frequency estimation of distorted signals in power systems,” *IEEE Trans. Instrum. Meas.*, vol. 51, no. 3, pp. 469–479, jun 2002.

[45] C. K. Ahn, P. Shi, Y. Shmaliy, and F. Liu, “Bayesian state estimation for Markovian jump systems: employing recursive steps and pseudocodes,” *IEEE Syst. Man, Cybern. Mag.*, vol. 5, no. 2, pp. 27–36, 2019.

[46] Z. Shi, Y. Li, and Z. Wang, “Switched multi-model estimation using probabilistic neural network decision for maneuvering target tracking,” *Int. J. Innov. Comput. Inf. Control*, vol. 14, no. 4, pp. 1481–1493, 2018.

[47] P. Tichavský and P. Handel, “Two Algorithms for Adaptive Retrieval of Slowly Time-Varying Multiple Cisoids in Noise,” *IEEE Trans. Signal Process.*, vol. 43, no. 5, pp. 1116–1127, 1995.

[48] M. Niedźwiecki and P. Kaczmarek, “Generalized Adaptive Notch Filter with a Self-optimization Capability,” *IEEE Trans. Signal Process.*, vol. 54, no. 11, pp. 4185–4193, 2006.

[49] M. Niedźwiecki and M. Meller, “New Algorithms for Adaptive Notch Smoothing,” *IEEE Trans. Signal Process.*, vol. 59, no. 5, pp. 2024–2037, 2011.

[50] G. Fedele and A. Ferrise, “A Frequency-locked-loop Filter for Biased Multi-sinusoidal Estimation,” *IEEE Trans. Signal Process.*, vol. 62, no. 5, pp. 1125–1134, 2014.

[51] M. Vetterli, J. Kovačević, and V. K. Goyal, *Foundations of signal processing.* Cambridge University Press, 2014.

[52] M. Riera-Guasp, J. A. Antonino-Daviu, and G.-A. Capolino, "Advances in Electrical Machine, Power Electronic, and Drive Condition Monitoring and Fault Detection: State of the Art," *IEEE Trans. Ind. Electron.*, vol. 62, no. 3, pp. 1746–1759, 2015.

[53] S. Nandi, H. A. Toliyat, and X. Li, "Condition Monitoring and Fault Diagnosis of Electrical Motors — A Review," *IEEE Trans. Energy Convers.*, vol. 20, no. 4, pp. 719–729, dec 2005.

[54] A. K. Samanta, "Designing real-time diagnostics for squirrel cage induction motors," Ph.D. dissertation, Indian Institute of Technology, 2016.

[55] M. Drif and A. J. M. Cardoso, "Stator fault diagnostics in squirrel cage three-phase induction motor drives using the instantaneous active and reactive power signature analyses," *IEEE Trans. Ind. Informat.*, vol. 10, no. 2, pp. 1348–1360, 2014.

[56] M. Wolkiewicz, G. Tarchała, T. Orłowska-Kowalska, and C. T. Kowalski, "Online stator interturn short circuits monitoring in the DFOC induction-motor drive," *IEEE Trans. Ind. Electron.*, vol. 63, no. 4, pp. 2517–2528, 2016.

[57] H. Henao, C. Bruzzese, E. Strangas, R. Pusca, J. Estima, M. Riera-guasp, and S. H. Kia, "Trends in Fault Diagnosis for Electrical Machines: A Review of Diagnostic Techniques," *IEEE Ind. Electron. Mag*, vol. 8, no. June, pp. 31–42, 2014.

[58] S. H. Kia, H. Henao, and G.-A. Capolino, "Zoom-MUSIC frequency estimation method for three-phase induction machine fault detection," in *Ind. Electron. Soc. 2005. IECON 2005. 31st Annu. Conf. IEEE.* IEEE, 2005, pp. 6—-pp.

[59] G. Didier, E. Ternisien, O. Caspary, and H. Razik, "Fault detection of broken rotor bars in induction motor using a global fault index," *IEEE Trans. Ind. Appl.*, vol. 42, no. 1, pp. 79–88, 2006.

[60] K. N. Gyftakis, D. V. Spyropoulos, J. C. Kappatou, and E. D. Mitronikas, "A Novel Approach for Broken Bar Fault Diagnosis in Induction Motors Through Torque Monitoring," *IEEE Trans. Energy Convers.*, vol. 28, no. 2, pp. 267–277, jun 2013.

[61] J. E. Garcia-Bracamonte, J. M. Ramirez-Cortes, J. de Jesus Rangel-Magdaleno, P. Gomez-Gil, H. Peregrina-Barreto, and V. Alarcon-Aquino, "An Approach on MCSA-based Fault Detection using Independent Component Analysis and Neural Networks," *IEEE Trans. Instrum. Meas.*, vol. 68, no. 5, pp. 1353–1361, 2019.

[62] S. E. Pandarakone, Y. Mizuno, and H. Nakamura, "Evaluating the Progression and Orientation of Scratches on Outer-raceway Bearing using a Pattern Recognition Method," *IEEE Trans. Ind. Electron.*, vol. 66, no. 2, pp. 1307–1314, 2018.

[63] W. Zhou, B. Lu, T. G. Habetler, and R. G. Harley, “Incipient Bearing Fault Detection via Motor Stator Current Noise Cancellation using Wiener Filter,” *IEEE Trans. Ind. App.*, vol. 45, no. 4, pp. 1309–1317, 2009.

[64] A. Soualhi, G. Clerc, and H. Razik, “Detection and Diagnosis of Faults in Induction Motor Using an Improved Ant Clustering Technique,” *IEEE Trans. Ind. Electron.*, vol. 60, no. 9, pp. 4053–4062, 2013.

[65] B. Corne, B. Vervisch, C. Debruyne, J. Knockaert, and J. Desmet, “Comparing MCSA with Vibration Analysis in Order to Detect Bearing Faults—A Case Study,” in *2015 IEEE Int. Electr. Mach. Drives Conf.* IEEE, 2015, pp. 1366–1372.

[66] S. Shao, S. McAleer, R. Yan, and P. Baldi, “Highly Accurate Machine Fault Diagnosis using Deep Transfer Learning,” *IEEE Trans. Ind. Electron.*, vol. 15, no. 4, pp. 2446–2455, 2018.

[67] Y. Xie, P. Chen, F. Li, and H. Liu, “Electromagnetic Forces Signature and Vibration Characteristic for Diagnosis Broken Bars in Squirrel Cage Induction Motors,” *Mech. Syst. Signal Process.*, vol. 123, pp. 554–572, 2019.

[68] J. L. Contreras-Hernandez, D. L. Almanza-Ojeda, S. Ledesma-Orozco, A. Garcia-Perez, R. J. Romero-Troncoso, and M. A. Ibarra-Manzano, “Quaternion Signal Analysis Algorithm for Induction Motor Fault Ddetection,” *IEEE Trans. Ind. Electron.*, vol. 66, no. 11, pp. 8843–8850, 2019.

[69] S. Pan, T. Han, A. C. C. Tan, and T. R. Lin, “Fault Diagnosis System of Induction Motors based on Multiscale Entropy and Support Vector Machine with Mutual Information Algorithm,” *Shock. Vib.*, vol. 2016, 2016.

[70] P. A. Delgado-Arredondo, A. Garcia-Perez, D. Morinigo-Sotelo, R. A. Osornio-Rios, J. G. Avina-Cervantes, H. Rostro-Gonzalez, and R. d. J. Romero-Troncoso, “Comparative Study of Time-frequency Decomposition Techniques for Fault Detection in Induction Motors using Vibration Analysis during Startup Transient,” *Shock. Vib.*, vol. 2015, 2015.

[71] A. Naha, K. R. Thammayyabbabu, A. K. Samanta, A. Routray, and A. K. Deb, “Mobile Aapplication to Detect Induction Motor Faults,” *IEEE Embed. Syst. Lett.*, vol. 9, no. 4, pp. 117–120, 2017.

[72] Y. Park, C. Yang, J. Kim, H. Kim, S. B. Lee, K. N. Gyftakis, P. A. Panagiotou, S. H. Kia, and G.-A. Capolino, “Stray Flux Monitoring for Reliable Detection of Rotor Faults under the Influence of Rotor Axial Air Ducts,” *IEEE Trans. Ind. Electron.*, vol. 66, no. 10, pp. 7561–7570, 2018.

[73] Y. Soleimani, S. M. A. Cruz, and F. Haghjoo, “Broken Rotor Bar Detection in Induction Motors Based on Air-Gap Rotational Magnetic Field Measurement,” *IEEE Trans. Instrum. Meas.*, vol. 68, no. 8, pp. 2916–2925, 2018.

[74] G. N. Surya, Z. J. Khan, M. S. Ballal, and H. M. Suryawanshi, "A Simplified Frequency-domain Detection of Stator Turn Fault in Squirrel-cage Induction Motors using an Observer Coil Technique," *IEEE Trans. Ind. Electron.*, vol. 64, no. 2, pp. 1495–1506, 2016.

[75] M. Nemec, K. Drobnic, D. Nedeljkovic, F. Rastko, and Ambrožic Vanja, "Detection of Broken Bars in Induction Motor Through the Analysis of Supply Voltage Modulation," *IEEE Trans. Ind. Electron.*, vol. 57, no. 8, pp. 2879–2888, 2010.

[76] M. A. Cruz, "An Active – Reactive Power Method for the Diagnosis of Rotor Faults in Three-Phase Induction Motors Operating Under Time-Varying Load Conditions," *IEEE Trans. Energy Convers.*, vol. 27, no. 1, pp. 71–84, 2012.

[77] M. Drif and A. J. M. Cardoso, "Discriminating the Simultaneous Occurrence of Three-Phase Induction Motor Rotor Faults and Mechanical Load Oscillations by the Instantaneous Active and Reactive Power Media Signature Analyses," *IEEE Trans. Ind. Electron.*, vol. 59, no. 3, pp. 1630–1639, mar 2012.

[78] A. Glowacz, "Fault Diagnosis of Single-phase Induction Motor based on Acoustic Signals," *Mech. Syst. Signal Process.*, vol. 117, pp. 65–80, 2019.

[79] S. Hemamalini, "Rational-Dilation Wavelet Transform Based Torque Estimation from Acoustic Signals for Fault Diagnosis in a Three-Phase Induction Motor," *IEEE Trans. Ind. Informat.*, vol. 15, no. 6, pp. 3492–3501, 2018.

[80] X. Ying, "Performance Evaluation and Thermal Fields Analysis of Induction Motor with Broken Rotor Bars Located at Different Relative Positions," *IEEE Trans. Magn.*, vol. 46, no. 5, pp. 1243–1250, 2010.

[81] R. A. Osornio-Rios, J. A. Antonino-Daviu, and R. de Jesus Romero-Troncoso, "Recent Industrial Applications of Infrared Thermography: A Review," *IEEE Trans. Ind. Informat.*, vol. 15, no. 2, pp. 615–625, 2018.

[82] A. Mohammed, J. I. Melecio, and S. Djurović, "Stator Winding Fault Thermal Signature Monitoring and Analysis by in situ FBG sensors," *IEEE Trans. Ind. Electron.*, vol. 66, no. 10, pp. 8082–8092, 2018.

[83] M. F. Cabanas, F. Pedrayes, M. G. Melero, C. H. R. García, J. M. Cano, G. A. Orcajo, and J. G. Norniella, "Unambiguous Detection of Broken Bars in Asynchronous Motors by Means of a Flux Measurement-Based Procedure," *IEEE Trans. Instrum. Meas.*, vol. 60, no. 3, pp. 891–899, 2011.

[84] C. Bruzzese, "Analysis and application of particular current signatures (symptoms) for cage monitoring in nonsinusoidally fed motors with high rejection to drive load, inertia, and frequency variations," *IEEE Trans. Ind. Electron.*, vol. 55, no. 12, pp. 4137–4155, 2008.

[85] J. Kim, S. Shin, S. B. Lee, K. N. Gyftakis, M. Drif, and A. J. M. Cardoso, “Power Spectrum-Based Detection of Induction Motor Rotor Faults for Immunity to False Alarms,” *IEEE Trans. Energy Convers.*, pp. 1–10, 2015.

[86] C. Yang, T.-j. Kang, S. B. Lee, J.-y. Yoo, A. Bellini, L. Zarri, and F. Filippetti, “Screening of False Induction Motor Fault Alarms Produced by Axial Air Ducts based on the Space Harmonic - Induced Current Components,” *IEEE Trans. Ind. Electron.*, vol. 62, no. 3, pp. 1803–1813, 2014.

[87] M. Hamadache, D. Lee, and K. C. Veluvolu, “Rotor Speed-Based Bearing Fault Diagnosis (RSB-BFD) under Variable Speed and Constant Load,” *IEEE Trans. Ind. Electron.*, vol. 62, no. 10, pp. 6486–6495, 2015.

[88] M. Garcia, P. A. Panagiotou, J. A. Antonino-Daviu, and K. N. Gyftakis, “Efficiency Assessment of Induction Motors Operating under Different Faulty Conditions,” *IEEE Trans. Ind. Electron.*, vol. 66, no. 10, pp. 8072–8081, 2018.

[89] A. Khezzar, M. Y. Kaikaa, M. E. K. Oumaamar, M. Boucherma, and H. Razik, “On the Use of Slot Harmonics as a Potential Indicator of Rotor Bar Breakage in the Induction Machine,” *IEEE Trans. Ind. Electron.*, vol. 56, no. 11, pp. 4592–4605, nov 2009.

[90] T.-j. Kang, J. Kim, S. B. Lee, and C. Yung, “Experimental Evaluation of Low-Voltage Offline Testing for Induction Motor Rotor Fault Diagnostics,” *IEEE Trans. Ind. Appl.*, vol. 51, no. 2, pp. 1375–1384, 2015.

[91] A. Stief, J. R. Ottewill, J. Baranowski, and M. Orkisz, “A PCA and Two-Stage Bayesian Sensor Fusion Approach for Diagnosing Electrical and Mechanical Faults in Induction Motors,” *IEEE Trans. Ind. Electron.*, vol. 66, no. 12, pp. 9510–9520, 2019.

[92] M.-K. Liu, M.-Q. Tran, and P.-Y. Weng, “Fusion of Vibration and Current Signatures for the Fault Diagnosis of Induction Machines,” *Shock. Vib.*, vol. 2019, 2019.

[93] A. K. Samanta, A. Routray, S. R. Khare, and A. Naha, “Direct Estimation of Multiple Time-Varying Frequencies of Non-Stationary Signals,” *Signal Process.*, vol. 169, p. 107384, 2020.

[94] M. M. Rahman and M. N. Uddin, “Online Unbalanced Rotor Fault Detection of an IM Drive based on Both Time and Frequency Domain Analyses,” *IEEE Trans. Ind. Appl.*, vol. 53, no. 4, pp. 4087–4096, 2017.

[95] A. Naha, A. Samanta, A. Routray, and A. Deb, “A Method for Detecting Half-broken Rotor Bar in Lightly Loaded Induction Motors using Current,” *IEEE Trans. Instrum. Meas.*, vol. 65, no. 7, 2016.

[96] A. Garcia-perez, R. D. J. Romero-troncoso, E. Cabal-yepez, and R. A. Osornio-rios, “The Application of High-Resolution Spectral Analysis for Identifying Multiple Combined Faults in Induction Motors,” *IEEE Trans. Ind. Electron.*, vol. 58, no. 5, pp. 2002–2010, may 2011.

[97] Y.-H. Kim, Y.-W. Youn, D.-H. Hwang, J.-H. Sun, and D.-S. Kang, "High-Resolution Parameter Estimation Method to Identify Broken Rotor Bar Faults in Induction Motors," *IEEE Trans. Ind. Electron.*, vol. 60, no. 9, pp. 4103–4117, sep 2013.

[98] B. Xu, L. Sun, L. Xu, and G. Xu, "An ESPRIT-SAA-Based Detection Method for Broken Rotor Bar Fault in Induction Motors," *IEEE Trans. Energy Convers.*, vol. 27, no. 3, pp. 654–660, 2012.

[99] V. Choqueuse and M. Benbouzid, "Induction Machine Faults Detection using Stator Current Parametric Spectral Estimation," *Mech. Syst. Signal Process.*, vol. 52, pp. 447–464, 2015.

[100] G. Bouleux, "Oblique projection pre-processing and TLS application for diagnosing rotor bar defects by improving power spectrum estimation," *Mech. Syst. Signal Process.*, vol. 41, no. 1-2, pp. 301–312, 2013.

[101] K. Teotrakool, M. J. Devaney, and L. Eren, "Adjustable-speed Drive Bearing-fault Detection via Wavelet Packet Decomposition," *IEEE Trans. Instrum. Meas.*, vol. 58, no. 8, pp. 2747–2754, 2009.

[102] J. Seshadrinath, B. Singh, and B. K. Panigrahi, "Investigation of Vibration Signatures for Multiple Fault Diagnosis in Variable Frequency Drives Using Complex Wavelets," *IEEE Trans. Power Electron.*, vol. 29, no. 2, pp. 936–945, feb 2014.

[103] W. He, Y. Zi, B. Chen, F. Wu, and Z. He, "Automatic Fault Feature Extraction of Mechanical Anomaly on Induction Motor Bearing using Ensemble Super-wavelet Transform," *Mech. Syst. Signal Process.*, vol. 54, pp. 457–480, 2015.

[104] J. J. Saucedo-Dorantes, M. Delgado-Prieto, R. A. Osornio-Rios, and R. de Jesus Romero-Troncoso, "Multifault Diagnosis Method Applied to an Electric Machine based on High-dimensional Feature Reduction," *IEEE Trans. Ind. Appl.*, vol. 53, no. 3, pp. 3086–3097, 2016.

[105] P. A. Delgado-arredondo, D. Morinigo-sotelo, R. A. Osornio-rios, J. G. Avina-cervantes, H. Rostro-gonzalez, and R. D. J. Romero-troncoso, "Methodology for fault detection in induction motors via sound and vibration signals," *Mech. Syst. Signal Process.*, vol. 83, pp. 568–589, 2017.

[106] X. Yan and M. Jia, "Application of CSA-VMD and optimal scale morphological slice bispectrum in enhancing outer race fault detection of rolling element bearings," *Mech. Syst. Signal Process.*, vol. 122, pp. 56–86, 2019.

[107] X. Tu, Y. Hu, F. Li, S. Abbas, Z. Liu, and W. Bao, "Demodulated High-Order Synchrosqueezing Transform With Application to Machine Fault Diagnosis," *IEEE Trans. Ind. Electron.*, vol. 66, no. 4, pp. 3071–3081, 2019.

[108] C. Morales-Perez, J. Rangel-Magdaleno, H. Peregrina-Barreto, J. P. Amezquita-Sanchez, and M. Valtierra-Rodriguez, "Incipient Broken Rotor Bar Detection in Induction Motors using Vibration Signals and the Orthogonal Matching Pursuit Algorithm," *IEEE Trans. Instrum. Meas.*, vol. 67, no. 9, pp. 2058–2068, 2018.

[109] Z. Zhao, S. Wu, B. Qiao, S. Wang, and X. Chen, "Enhanced sparse period-group lasso for bearing fault diagnosis," *IEEE Trans. Ind. Electron.*, vol. 66, no. 3, pp. 2143–2153, 2019.

[110] A. Naha, A. Samanta, A. Routray, and A. Deb, "Low Complexity Motor Current Signature Analysis Using Sub-Nyquist Strategy With Reduced Data Length," *IEEE Trans. Instrum. Meas.*, 2017.

[111] F. Dalvand, M. Kang, S. Dalvand, and M. Pecht, "Detection of Generalized-Roughness and Single-Point Bearing Faults Using Linear Prediction-Based Current Noise Cancellation," *IEEE Trans. Ind. Electron.*, vol. 65, no. 12, pp. 9728–9738, 2018.

[112] F. B. Abid, S. Zgarni, and A. Braham, "Distinct bearing faults detection in induction motor by a hybrid optimized SWPT and aiNet-DAG SVM," *IEEE Trans. Energy Convers*, vol. 33, no. 4, pp. 1692–1699, 2018.

[113] J. Wu, C. Wu, S. Cao, S. W. Or, C. Deng, and X. Shao, "Degradation data-driven time-to-failure prognostics approach for rolling element bearings in electrical machines," *IEEE Trans. Ind. Electron.*, vol. 66, no. 1, pp. 529–539, 2019.

[114] S. Schmidt and P. S. Heyns, "An open set recognition methodology utilising discrepancy analysis for gear diagnostics under varying operating conditions," *Mech. Syst. Signal Process.*, vol. 119, pp. 1–22, 2019.

[115] M. Y. Kaikaa and M. Hadjami, "Effects of the Simultaneous Presence of Static Eccentricity and Broken Rotor Bars on the Stator Current of Induction Machine," *IEEE Trans. Ind. Electron.*, vol. 61, no. 5, pp. 2452–2463, 2014.

[116] P. Shi, Z. Chen, Y. Vagapov, and Z. Zouaoui, "A new diagnosis of broken rotor bar fault extent in three phase squirrel cage induction motor," *Mech. Syst. Signal Process.*, vol. 42, no. 1-2, pp. 388–403, 2014.

[117] A. Bellini, F. Filippetti, G. Franceschini, C. Tassoni, and G. B. Kliman, "Quantitative Evaluation of Induction Motor Broken Bars by Means of Electrical Signature Analysis," *IEEE Trans. Ind. Appl.*, vol. 37, no. 5, pp. 1248–1255, oct 2001.

[118] B. Xu, L. Sun, and H. Ren, "A New Criterion for the Quantification of Broken Rotor Bars in Induction Motors," *IEEE Trans. Energy Convers.*, vol. 25, no. 1, pp. 100–106, mar 2010.

[119] Y. Trachi, E. Elbouchikhi, V. Choqueuse, and M. E. H. Benbouzid, "Induction Machines Fault Detection Based on Subspace Spectral Estimation," *IEEE Trans. Ind. Electron.*, vol. 63, no. 9, pp. 5641–5651, sep 2016.

[120] B. Halder and T. Kailath, “Efficient Estimation of Closely Spaced Sinusoidal Frequencies Using Subspace-Based Methods,” *IEEE Signal Process. Lett.*, vol. 4, no. 2, pp. 49–51, 1997.

[121] P. Stoica, H. Li, and J. Li, “Amplitude Estimation of Sinusoidal Signals : Survey , New Results , and an Application,” *IEEE Trans. Signal Process.*, vol. 48, no. 2, pp. 338–352, 2000.

[122] C. Concari, G. Franceschini, and C. Tassoni, “Differential diagnosis based on multivariable monitoring to assess induction machine rotor conditions,” *IEEE Trans. Ind. Electron.*, vol. 55, no. 12, pp. 4156–4166, 2008.

[123] R. Romero-Troncoso, D. Morinigo-Sotelo, O. Duque-Perez, P. Gardel-Sotomayor, R. Osornio-Rios, and A. Garcia-Perez, “Early broken rotor bar detection techniques in vsd-fed induction motors at steady-state,” in *2013 9th IEEE International Symposium on Diagnostics for Electric Machines, Power Electronics and Drives (SDEMPED).* IEEE, 2013, pp. 105–113.

[124] B. Ayhan, H. J. Trussell, M.-y. Chow, and M.-H. Song, “On the Use of a Lower Sampling Rate for Broken Rotor Bar Detection With DTFT and AR-Based Spectrum Methods,” *IEEE Trans. Ind. Electron.*, vol. 55, no. 3, pp. 1421–1434, 2008.

[125] R. Puche-Panadero, M. Pineda-Sanchez, M. Riera-Guasp, J. Roger-Folch, E. Hurtado-Perez, and J. Perez-Cruz, “Improved Resolution of the MCSA Method Via Hilbert Transform , Enabling the Diagnosis of Rotor Asymmetries at Very Low Slip,” *IEEE Trans. Energy Convers.*, vol. 24, no. 1, pp. 52–59, 2009.

[126] B. Xu, L. Sun, L. Xu, and G. Xu, “Improvement of the Hilbert Method via ESPRIT for Detecting Rotor Fault in Induction Motors at Low Slip,” *IEEE Trans. Energy Convers.*, vol. 28, no. 1, pp. 225–233, 2013.

[127] M. Pineda-sanchez, J. Perez-cruz, J. Pons-llinares, V. Climente-alarcon, and J. A. Antonino-daviu, “Application of the Teager – Kaiser Energy Operator to the Fault Diagnosis of Induction Motors,” *IEEE Trans. Energy Convers.*, vol. 28, no. 4, pp. 1036–1044, 2013.

[128] C. G. Dias and I. E. Chabu, “Spectral Analysis Using a Hall Effect Sensor for Diagnosing Broken Bars in Large Induction Motors,” *IEEE Trans. Instrum. Meas.*, vol. 63, no. 12, pp. 2890–2902, 2014.

[129] A. Sapena-Baño, M. Pineda-Sanchez, R. Puche-Panadero, J. Martinez-Roman, and Ž. Kanović, “Low-Cost Diagnosis of Rotor Asymmetries in Induction Machines Working at a Very Low Slip Using the Reduced Envelope of the Stator Current,” *IEEE Trans. Energy Convers.*, vol. 30, no. 4, pp. 1409–1419, dec 2015.

[130] V. Climente-Alarcon, J. A. Antonino-Daviu, E. G. Strangas, and M. Riera-Guasp, “Rotor-bar breakage mechanism and prognosis in an induction motor,” *IEEE Trans. Ind. Electron.*, vol. 62, no. 3, pp. 1814–1825, 2015.

---

[131] E. Elbouchikhi, V. Choqueuse, F. Auger, and M. E. H. Benbouzid, "Motor Current Signal Analysis based on a Matched Subspace Detector," *IEEE Trans. Instrum. Meas.*, vol. 66, no. 12, pp. 3260–3270, 2017.

[132] T. Han, C. Liu, L. Wu, S. Sarkar, and D. Jiang, "An adaptive spatiotemporal feature learning approach for fault diagnosis in complex systems," *Mech. Syst. Signal Process.*, vol. 117, pp. 170–187, 2019.

[133] R. Zhao, R. Yan, Z. Chen, K. Mao, P. Wang, and R. X. Gao, "Deep learning and its applications to machine health monitoring," *Mech. Syst. Signal Process.*, vol. 115, pp. 213–237, 2019.

[134] Y. Lei, B. Yang, X. Jiang, F. Jia, N. Li, and A. K. Nandi, "Applications of Machine Learning to Machine Fault Diagnosis: A review and Roadmap," *Mech. Syst. Signal Process.*, vol. 138, p. 106587, 2020.

[135] R. Razavi-Far, M. Farajzadeh-Zanjani, and M. Saif, "An Integrated Class-imbalanced Learning Scheme for Diagnosing Bearing Defects in Induction Motors," *IEEE Trans. Ind. Informat.*, vol. 13, no. 6, pp. 2758–2769, 2017.

[136] Y. Trachi, E. Elbouchikhi, V. Choqueuse, M. E. H. Benbouzid, and T. Wang, "A Novel Induction Machine Fault Detector based on Hypothesis Testing," *IEEE Trans. Ind. App.*, vol. 53, no. 3, pp. 3039–3048, 2016.

[137] S. M. Kay, *Fundamentals of Statistical Signal Processing: Detection Theory.* Prentice-Hall (Upper Saddle River, NJ [ua]), 1998.

[138] A. T. Johansson and P. R. White, "Instantaneous Frequency Estimation at Low Signal-to-noise Ratios using Time-varying Notch Filters," *Signal Process.*, vol. 88, no. 5, pp. 1271–1288, 2008.

[139] T. Hsiao, "Identification of time-varying autoregressive systems using maximum a posteriori estimation," *IEEE Trans. Signal Process.*, vol. 56, no. 8, pp. 3497–3509, 2008.

[140] D. Simon, "Kalman Filtering with State Constraints: a Survey of Linear and Nonlinear Algorithms," *IET Control Theory Appl.*, vol. 4, no. 8, pp. 1303–1318, 2010.

[141] N. Gupta and R. Hauser, "Kalman Filtering with Equality and Inequality State Constraints," *arXiv Prepr. arXiv0709.2791*, 2007.

[142] A. Naha and A. K. Deb, "Particle swarm optimisation with Kalman correction," *Electron. Lett.*, vol. 49, no. 7, pp. 465–467, 2013.

[143] R. Baraniuk, "Bat Echolocation Chirp," *DSP Group, Rice Univ. Houston, TX*, 2009.

[144] L. Zuo, M. Li, Z. Liu, and L. Ma, "A High-Resolution Time-Frequency Rate Representation and the Cross-Term Suppression." *IEEE Trans. Signal Process.*, vol. 64, no. 10, pp. 2463–2474, 2016.

[145] B. P. Abbott, R. Abbott, T. D. Abbott, M. R. Abernathy, F. Acernese, K. Ackley, C. Adams, T. Adams, P. Addesso, R. X. Adhikari, and Others, "Observation of gravitational waves from a binary black hole merger," *Phys. Rev. Lett.*, vol. 116, no. 6, p. 61102, 2016.

[146] Y. Pan, A. Buonanno, M. Boyle, L. T. Buchman, L. E. Kidder, H. P. Pfeiffer, and M. A. Scheel, "Inspiral-merger-ringdown multipolar waveforms of nonspinning black-hole binaries using the effective-one-body formalism," *Phys. Rev. D*, vol. 84, no. 12, p. 124052, 2011.

[147] V. Y. Pan, "Solving a polynomial equation: some history and recent progress," *SIAM Rev.*, vol. 39, no. 2, pp. 187–220, 1997.

[148] B. N. Datta, *Numerical linear algebra and applications.* Siam, 2010.

[149] M. H. Hayes, *Statistical Digital Signal Process. and Modeling.* John Wiley & Sons, 2010.

[150] A. Naha, A. K. Samanta, A. Routray, and A. K. Deb, "Determining Autocorrelation Matrix Size and Sampling Frequency for MUSIC Algorithm," *IEEE Signal Process. Lett.*, vol. 22, no. 8, pp. 1016–1020, aug 2015.

[151] Q. Zhang, "Probability of resolution of the MUSIC algorithm," *IEEE Trans. Signal Process.*, vol. 43, no. 4, pp. 978–987, apr 1995.

[152] M. S. Zaky, M. M. Khater, S. S. Shokralla, and H. Yasin, "Wide-Speed-Range Estimation With Online Parameter Identification Schemes of Sensorless Induction Motor Drives," *IEEE Trans. Ind. Electron.*, vol. 56, no. 5, pp. 1699–1707, may 2009.

[153] S. Nandi, S. Ahmed, and H. A. Toliyat, "Detection of Rotor Slot and Other Eccentricity Related Harmonics in a Three Phase Induction Motor with Different Rotor Cages," *Energy*, vol. 16, no. 3, pp. 253–260, 2001.

[154] Y. Li, X. Wang, S. Si, and S. Huang, "Entropy based Fault Classification using the Case Western Reserve University Data: A Benchmark Study," *IEEE Trans. Rel*, 2020.

[155] J. Zhang, S. Yi, G. U. O. Liang, G. A. O. Hongli, H. Xin, and S. Hongliang, "A New Bearing Fault Diagnosis Method based on Modified Convolutional Neural Networks," *Chinese J. Aeronaut.*, vol. 33, no. 2, pp. 439–447, 2020.

[156] D. Zhao, F. Liu, and H. Meng, "Bearing Fault Diagnosis based on the Switchable Normalization SSGAN with 1-D Representation of Vibration Signals as Input," *Sensors*, vol. 19, no. 9, p. 2000, 2019.

[157] D.-T. Hoang and H.-J. Kang, "Rolling Element Bearing Fault Diagnosis using Convolutional Neural Network and Vibration Image," *Cogn. Syst. Res.*, vol. 53, pp. 42–50, 2019.

[158] Y. Yuan, G. Ma, C. Cheng, B. Zhou, H. Zhao, H.-T. Zhang, and H. Ding, "Artificial Intelligent Diagnosis and Monitoring in Manufacturing," *arXiv Prepr. arXiv1901.02057*, 2018.

[159] C. Lu, Z.-Y. Wang, W.-L. Qin, and J. Ma, "Fault Diagnosis of Rotary Machinery Components using a Stacked Denoising Autoencoder-based Health State Identification," *Signal Process.*, vol. 130, pp. 377–388, 2017.

[160] X. Wang, Y. Li, T. Rui, H. Zhu, and J. Fei, "Bearing Fault Diagnosis Method based on Hilbert Envelope Spectrum and Deep Belief Network," *J. Vibroengineering*, vol. 17, no. 3, pp. 1295–1308, 2015.

[161] A. Mukherjee, A. Routray, and A. Samanta, "Method for On-line Detection of Arcing in Low Voltage Distribution Systems," *IEEE Trans. Power Del.*, vol. PP, no. 99, p. 1, 2015.

[162] D. Ganga and V. Ramachandran, "IoT-Based Vibration Analytics of Electrical Machines," *IEEE Internet Things J.*, vol. 5, no. 6, pp. 4538–4549, 2018.

[163] A. Belahcen, K. N. Gyftakis, J. Martinez, V. Climente-Alarcon, and T. Vaimann, "Condition monitoring of electrical machines and its relation to industrial internet," in *2015 IEEE Work. Electr. Mach. Des. Control Diagnosis.* IEEE, 2015, pp. 233–241.

Dissemination out of the Thesis

Patent Filed

1. A. Routray, A. Naha, **A. K. Samanta**, Amey Pawar, & Chandrasekhar Sakpal, “A system for assessment of multiple faults in induction motors”, WO2019167086A1, 2019.

Journals

1. **A. K. Samanta**, A. Routray, S.R. Khare, & A. Naha, “Minimum Distance-based Detection of IncipientInduction Motor Faults using Rayleigh Quotient Spectrum of Conditioned Vibration Signal [Accepted]”, *IEEE Transactions on Instrumentation and Measurement.*
2. **A. K. Samanta**, A. Routray, S.R. Khare, & A. Naha, “Direct Estimation of Multiple Time-varying Frequencies of Non-stationary Signals”, *Signal Processing*, vol.169, 2020.
3. **A. K. Samanta**, A. Naha, A. Routray, & A. K. Deb “Fast and accurate spectral estimation for online detection of partial broken bar in induction motors”, *Elsevier Mechanical Systems and Signal Processing*, vol. 98, pp. 63-77, 2018.

Author Biography

Anik Kumar Samanta is a doctoral candidate from Advanced Technology Development Centre at the Indian Institute of Technology Kharagpur. After completing his thesis, he joined the data science and machine learning group at Eaton/Danfoss R&D. Previously, he has received his M.S. degree from the same institute in 2016, and his B. Tech. degree from Dr. B. C. Roy Engineering College, Durgapur, India, in 2011. His research interests include high-resolution spectral estimation, signal-based fault diagnosis of induction motors, detection theory, detection and estimation of parameters under non-stationary conditions, and embedded signal processing. **Homepage**: https://eceanik.github.io/